AD-767 319

ANALYSIS OF HEAD IMPACT

Stephen L. Gordon

Naval Air Development Center

Prepared for:

Naval Air Systems Command

1 April 1973

NAVAL AIR
DEVELOPMENT
CENTER

Warminster, Pennsylvania

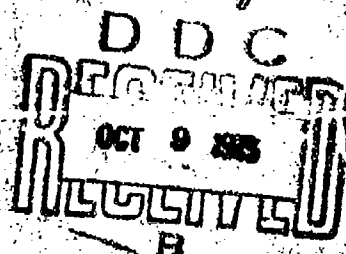REPORT NO. NADC-73065-40 1 APRIL 1973

ANALYSIS OF HEAD IMPACT

INTERIM REPORT

AIRTASK A310310C/001A/3R-04101001, W.U. 1

Approved for public release; distribution unlimited.

D D C
RECEIVED
OCT 9 1973
B

135

DOCUMENT CONTROL DATA - R & D

Security classification of title, body of abstract and indexing annotation must be entered when the overall report is classified

1. ORIGINATING ACTIVITY (Corporate author)	2a. REPORT SECURITY CLASSIFICATION
Crew Systems Department Naval Air Development Center Warminster, Pennsylvania 18974	**UNCLASSIFIED** 2b. GROUP

3. REPORT TITLE

Analysis of Head Impact

4. DESCRIPTIVE NOTES (Type of report and inclusive dates)
Interim Report

5. AUTHOR(S) (First name, middle initial, last name)

Stephen L. Gordon

6. REPORT DATE	7a. TOTAL NO. OF PAGES	7b. NO. OF REFS
1 April 1973	124	72

8a. CONTRACT OR GRANT NO	9a. ORIGINATOR'S REPORT NUMBER(S)
b. PROJECT NO AIRTASK A310310C/001A/3R-04101001	NADC-73065-40
c Work Unit - 01 d.	9b. OTHER REPORT NO(S) (Any other numbers that may be assigned this report)

10. DISTRIBUTION STATEMENT

Approved for Public Release; Distribution Unlimited.

11. SUPPLEMENTARY NOTES	12. SPONSORING MILITARY ACTIVITY
	Naval Air Systems Command Department of the Navy Washington, D.C. 20360

13. ABSTRACT

A finite difference form of the governing equations of motion for one and two-dimensional wave propagation is utilized to solve the problem of non-penetrating impact to the human head. The layered plate one-dimensional analysis provides a method of predicting the influence of several material property and size modifications in a geometrically simplified head impact model. The spherical model with a layered energy absorbing skull yields highly attenuated and smoothed tensile pressure peaks in the brain as compared to the results with a single layered elastic skull. An elastic brain model (that includes an assumed high dynamic shear modulus) suggests that the combined shear-normal stress levels would be more likely to cause failure than the shear free stress condition in a hydrodynamic brain model. The generality of the solution techniques would readily permit extension of the analyses to investigate the significance of future modelling considerations.

DD FORM **1473** (PAGE 1)

0102 014 6600

i

14 KEY WORDS	LINK A		LINK B		LINK C	
	ROLE	WT	ROLE	WT	ROLE	WT
HEAD INJURY						
PROTECTIVE HELMETS						
CRASH WORTHINESS						
SKULL						
BIOMECHANICS						

DEPARTMENT OF THE NAVY
NAVAL AIR DEVELOPMENT CENTER

REPORT NO. NADC-73065-40   1 APRIL 1973

ANALYSIS OF HEAD IMPACT

INTERIM REPORT

AIRTASK A310310C/001A/3R-04101001, W.U. 1

Reported by: _Stephen L. Gordon_
Stephen L. Gordon, Ph.D.
Applied Physiology Lab- CSD

Reviewed by: _E. Hendler_
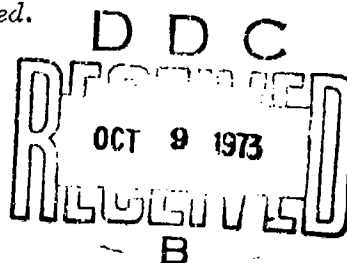E. Hendler, Ph.D., Head,
Applied Physiology Lab- CSD

H.J. von Beckh
H.J. von Beckh, M.D.
Med. Res. Dir. - CSD

Approved by: _L.H. Blackburn_
L.H. Blackburn, CAPT, MC, USN
Director, Crew Systems Department

DDC

RECEIVED

OCT 9 1973

B

This report is based on work completed in partial fulfillment of the requirements for the Ph.D. degree in Biomedical Engineering for Drexel University, Philadelphia, Pennsylvania. Portions of the experimental results are repeated (for clarity) from the Annual Progress Report "Development of Multi-Layer Models for the Head under Impact" (Contract #N62269-72-C-0171) November 8, 1972 by G.D. Moskowitz and J.L. Rose.

ii

SUMMARY

As a consequence of Man's travel at increasing speeds, the incidence and severity of head injuries has also increased. The development of adequate protection against such injury requires a thorough knowledge of the mechanics of trauma to an unprotected head.

A finite difference form of the governing equations of motion for one and two-dimensional wave propagation is utilized to solve the problem of non-penetrating impact to the human head. Two aspects of the analyses provide significant improvement over previous models: (1) multi-layered structuring which includes (2) more accurate material definitions for each layer. A series of dynamic photoelastic experiments add qualitative confidence in the solution techniques.

The layered plate one-dimensional analysis provides a method of predicting the influence of several material property and size modifications in a geometrically simplified head impact model. The spherical model with a layered energy absorbing skull yields highly attenuated and smoothed tensile pressure peaks in the brain as compared to the results with a single layered elastic skull. An elastic brain model (that includes an assumed high dynamic shear modulus) suggests that the combined shear-normal stress levels would be more likely to cause failure than the shear free stress condition in a hydrodynamic brain model. The generality of the solution techniques would readily permit extension of the analyses to investigate the significance of future modelling considerations.

TABLE OF CONTENTS

LIST OF TABLES

v

LIST OF ILLUSTRATIONS

LIST OF ILLUSTRATIONS (Continued)

LIST OF ILLUSTRATIONS (Continued)

I - INTRODUCTION

As a consequence of man's travel at increasing speeds, the incidence and severity of head injuries has also increased. Walker (1966) noted that in motor vehicle accidents approximately two-thirds of the cases involve head injury. In addition, between the ages of 1 and 44 years, head injury ranks as the prime killer in the United States (Walker (1966). The development of adequate protection against such injury requires a thorough knowledge of the mechanics of trauma to an unprotected head.

In this present work, theoretical one-and two-dimensional head models are developed which could lead to improved understanding of head injury mechanics. Two aspects of the analysis provide significant improvement over previous models: (1) multi-layered structuring which includes (2) more accurate material definitions for each layer. The realistic head impact model solution predicts the stress wave propagation which occurs when the head is struck by a low velocity impactor.

Physiological and Pathological Considerations

There are three classifications of types of blows to the head. Impulsive blows involve accelerations to the head when there is no direct contact with the impactor. This situation is typified by whiplash injuries. Objects which strike the head and pierce the brain matter produce penetrating blows. Bullet and high-velocity fragment wounds are examples of this type of injury. Finally, impactors which strike the head, but do not enter the brain, are classified as non-penetrating

blows. Unterharnscheidt and Sellier (1965) further subclassify non-penetrating blows as primary (cerebral cortex damage and subdural hematomas) and secondary (circulatory problems due to brain stem damage). The model discussed in this dissertation is for the case of a primary non-penetrating blow to the head where the skull does not fracture.

In the present research, initial wave propagation response analysis is the primary objective; however, other potential injury mechanisms are included to provide a complete description. Because of the relatively high compressive strength of brain tissue, overpressure is generally regarded as a secondary cause of injurious mechanical stress. Potentially dangerous forces resulting from underpressure, rotation, and cervical stretching will be discussed individually.

Benedict (1969) discussed three means by which underpressure can result in tissue damage: (1) outgassing of entrained gas; (2) vaporization of liquid (flash boiling); and (3) tissue failure in tension. Liu, Chan, and Nelson (1971) describe a failure criterion for capillary vessels as the cumulative time spent beyond a critical tensile pressure. Unterharnscheidt and Sellier (1966) showed that a fixed head (of experimental animals) allowed no separation between brain and skull, and therefore produced no cavitation injury. Goldsmith (1966) expressed an opposing view, claiming that cavitation is the result of rarefaction waves reflected from the skull boundary opposite from the site of the blow.

Rotational forces which result in the shearing of tissues can be caused by whiplash or non-penetrating blows. The original work in this area was presented by Holbourn (1943), who based much of his theory on

the fact that the bulk modulus of brain tissue is several orders of magnitude higher than the modulus of rigidity. This fact suggested that at low shear levels brain tissues could separate and produce injury. Ommaya, Hirsch, and Martinez (1966) subjected experimental animals to blows which could cause head rotation. In one case, a plaster collar restricted head rotation and permitted only translation, and in the second case, unrestricted head rotation was allowed. The results indicated that rotation was necessary to cause concussion at a given level of impact. One experimental study induced purely rotational forces on the head. This resulted not only in brain trauma, but also in spinal cord injury (Unterharnscheidt and Higgins (1969)).

Cervical stretch has been demonstrated to produce injury patterns similar to impact without any actual impacting blow (Friede (1961)) and vonGierke (1966). vonGierke (1966) used a nearly hardened soft plastic model of the cervical cord region to show the indentation caused by stretching over the odontoid process.

Injury produced by a change in volume within the brain case is mainly related to slower acting forms of insult, such as tumors or hematomas (e.g., Evans (1966) and Gurdjian and Webster (1958). Langfitt et al (1966) demonstrated that for monkeys, an intracranial volume change greater than 4 ml resulted in extremely high intercranial pressure. While this is not of direct consequence in impact studies, the cumulative volume change effects of repeated (vibration) blows might be important.

The neuropathological investigations of Lindenberg and Freytag (1957) show the typical wedge shaped contusion necroses found on the opposite from the impact location. These contre coup regions are widest at the

crest of a convolution with the point of the wedge extending toward or
into the white matter. Streak-like, multiple, and densely arranged con-
tusion hemorrhages are also described. Detailed light microscopic
analysis of nerve fiber (white-matter) damage is given by Stritch
(1956 and 1961). Evidence of torn or severed segments of white-matter
is shown with the presence of retraction balls of axoplasm at the cut
ends. A general discussion of the feasibility of using physiopatho-
logical discoveries to uncover the mechanical pathways of head injury
is presented by Ommaya (1969).

Injury Tolerance Criteria

Experimental *in-vivo* observation of neural tissue injury in humans
during head impact has not been (and probably never will be) accomplished.
Physical and theoretical modelling of head impact must be cautiously
correlated to the best available *in-vitro* and pathological human findings
and *in-vivo* animal experiments.

An important consideration in modelling head impact is the dynamic
nature of a non-penetrating blow. The duration of an impact blow has
physical as well as physiological significance in defining head injury
criteria. Kornhauser (1954) describes a cross-over point between short
and long blows at one-third to one-fourth of the natural period for
simple single degree of freedom systems. Holbourne (1943) and Rayne
and Masien (1969) state that long duration blows (compared to the
natural period of the system) result in head displacement being pro-
portional to the peak input acceleration, while for short duration
blows displacement is proportional to change in velocity .

The Wayne-State Impact Tolerance curve was developed with the

criteri_ _eventing a simple linear skull fracture that often
accompanies concussion. Based primarily on results determined by dropping
cadavers on their heads, the Wayne-State curves (e.g., Gurdjian, et al.
(1964) and Patrick (1966) have the general form of a rectangular hyper-
bola. The ordinate of this curve is acceleration and the abcissa is
duration of blow. Beyond a crossover duration of about 10m sec, the
injury tolerance can be defined as a constant level of peak acceleration.

Two additional injury criteria are based on the concepts of the
Wayne-State curve. The Severity Index is computed by integrating (with
respect to time) acceleration to the 2.5 power. The single resultant
value must be less than a given injury level constant (1000). A recent
Maximum Strain Criteria by McElhaney, Roberts, and Stalmaker (1971)
describes the largest strain permissible in a simple mass-spring-damper
model for head impact response. The Maximum Strain Criteria is also
based on the average strain required to cause skull fracture.

One rotational injury criterion is not based on preventing skull
fracture. Mahone, et al (1967) present rotational velocity vs. rotation-
al acceleration injury threshold curves for experimental impacts to
Rhesus monkeys. A scaling factor between various primates was developed
by Ommaya, Yarnell, Hirsch, and Harris (1967) such that an inverse 2/3
power relationship exists between brain masses and rotational accelera-
tions. The monkey to man brain mass similitude analysis can be used to
plot a rotational tolerance curve for man.

The Wayne State curves were developed by considering that simple
linear skull fracture frequently appears in concussed patients. This
phenomenological approach does not account for the mechanisms of the

primary concussion injury. Likewise, the Severity Index defines a
somewhat arbitrary injury cutoff value which is not determined from
potential brain tissue damage. Even the rotational injury criteria are
not related to specific shear levels within the cranial vault. All of
these criteria are useful in estimating a damage threshold; however,
they do not define the severity or nature of the brain injury mechanism.

The Maximum Strain Criteria provides a meaningful correlation be-
tween the existing protective indices and the actual strain levels in a
lumped parameter skull-brain model. The Cumulative Damage Index (liu,
et al (1971)) describes contre-coup injury as the time averaged stress
during which the negative pressure at a given brain region is above a
critical level. In a like manner, the present research effort is
directed towards defining physical phenomena which are the potential
source of brain damage during impact. Whenever possible, the brain
injury mechanism hypotheses are correlated to the exisiting, more
directly measurable, impact tolerance criteria.

Time Scale

The term non-penetrating head trauma suggests that at some time,
after the blow is delivered, an injurious mechanical force is applied
to the brain for a finite period of time. Two criteria are necessary
to define a time scale for identifying types of head injury mechanisms:
(1) time of injury occurence and (2) duration of damaging force. A
simplifying fact is that most short duration injury forces occur soon
after the impact, while most longer duration forces occur later.

The sound wave transit time in a brain is about 120 μ sec
(Unterharnscheidt and Sellier (1966)). During the wave propagation

which follows an impact blow many reflected and refracted waves periodically interact with each other. This indicates that local brain tissues are stressed with a period several times less than the characteristic period of 120 μ sec.

Only physical modelling experiments have shown the existence of potential injury forces at times less than 1 m sec (1000 μ sec) after impact. Janssen and Bowman (1970) show wave propagation in a photoelastic brain model. Because the high shear stress levels enter and exit a given location from frame to frame (250μ sec intervals), the damaging force duration must be less than 250 μ sec. Gross (1958) analyzed high-speed photographs (4000 frames per second) of a rubber mallet striking a water filled glass flask to display cavitation bubbles 500 μ sec after impact. Sellier and Unterharnscheidt (1965) implanted pressure transducers in cadaver heads and recorded a peak negative contre-coup pressure at 500 μ sec after delivery of an impact blow.

Many of the later occurring peak forces were observed by delivering a blow to the head of an animal subject whose head was free to rotate. Data from such experiments was gathered fror. probes located external to the skull. Friede (1961) struck the occipital region of a cat's skull with a pendulum and recorded maximal frontal bone velocity at 4 m sec. Ommaya, Hirsh, and Martinez (1966) impacted monkeys and photographically determined the peak rotational acceleration to occur at 4 msec and to have a duration of 2.5 msec. In experiments with human volunteers wearing helmets, Lombard (1949) showed peak acceleration from a frontal blow to last approximately 2 m sec.

Even longer durations and later arrival times for injury forces ar-
found in the indirect whiplash type of injury. Horizontal sled experi-
ments with humans (e.g. Ewing, Thomas, Patrick, Beeler, Smith (1970) and
Stapp (1957) resulted in approximately 10 m sec duration peak head ac-
celerations. Head motion started 75 m sec after the onset of sled ac-
celeration.

The present detailed wave propagation analysis is not extended for
a long time after the impact blow is delivered. Longer solutions to the
complex formulations of multi-layered head impact might require an in-
creased degree of approximation. Emphasis is placed on predicting tissue
damage phenomena occurring earlier than 500 µsec and lasting less than
25 µsec.

II - MODELLING CONSIDERATIONS

Previous Theoretical Models

Before beginning a thorough discussion of the present theoretical modelling, a brief review of previous skull-brain impact analyses is presented. The mathematical approach of most investigators has been to consider geometrically and materially simplified models which represent the overall closed head (no-fracture) impact situation. This approach has led to the prediction of potential sites of contre-coup, intermediate coup, and coup.

The first theoretical model (Anzelius (1943)) consisted of a rigid, fluid-filled spherical shell which reduced the problem to the solution of the wave equation in spherical coordinates. Goldsmith (1966) suggested that the model be modified to include an elastic shell.

The mathematical contribution of Rand and DiMaggio (1967) in the field of acoustics led to a solution for the vibratory response of a fluid-filled, elastic membrane sphere. Engin (1969) added bending to the formulation and described the head as a thin, elastic, isotropic, and homogeneous sphere filled with an inviscid, compressible fluid. The solution technique consisted of a Laplace transformation method with a radially directed impulsive loading function.

Several modifications of the Engin model have been made within the same general configuration. Benedict (1969) considered the Engin approach too cumbersome for any generalized forcing function, except the dirac-delta. He has obtained a finite difference solution for a time and spatially varying input function. Recently, Liu, et al (1971) expanded the input to the Engin model to include a spatially dependent,

finite time pulse. An approximate thick shell model with transverse

shear and rotatory inertia was solved by Advani and Lee (1970). A

suggested improvement (Engin and Liu (1970) and Roberts, Hodgson, and

Thomas (1966) is the addition of a weakly plugged foramen magnum.

One-dimensional models are inherently much simpler to analyze

and much less expensive in computer time costs. The small number of

parameters required to define the problem also make discussion of one-

dimensional models much easier.

Hayashi (1969) describes a rigid but massless container (skull)

filled with an elastic fluid (brain). The vessel is attached to a

linear spring which represents the resultant effects of skull and

hair elasticity. The slowly converging infinite series solutions are

meaningless in computing numerical results. Liu (1970), in reviewing

and critiquing the Hayashi model, provides an exact, closed form

solution for this one-dimensional model. He also suggests including a

damper in parallel with the spring. The lumped parameter head model by

McElhaney, et al (1970) provides linear brain displacement results for

various input configurations. The simplicity of this four element

model (two masses, one spring, and one damper) allows solutions to be

extended to several hundred milli seconds.

Anatomical and Theoretical Structuring

Anatomical observation suggests that the head consists of many

layers of different materials. A magnified view of a head cross-

section would show ten or more separate layers. A somewhat simplified

head cross-sectional sketch is shown in Figure 1. Many layers are

included within each of the four regions indicated. The rationale for choosing the particular layers that are included in the theoretical analysis is discussed in the following paragraphs.
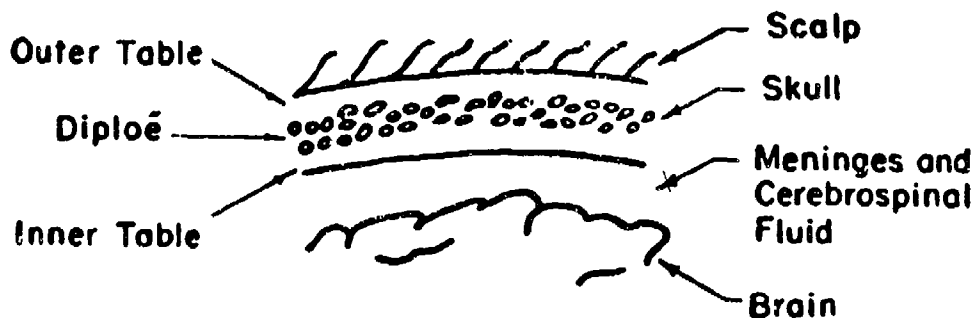
Figure 1. Diagram of cross-section of a portion of the head.

Galford and McElhaney (1970) claim the scalp acts as a cushion in the transmission of forces to the brain. Because the soft visco-elastic scalp is only partially restrained, it is free to be pushed aside and be readily displaced by a rapidly moving impactor. The scalp primarily provides protection against lower velocity, glancing blows. While the scalp might slightly reduce the energy delivered to the skull, the scalp is considered to be of secondary importance compared to the skull. Therefore, the scalp is not included in the initial modelling.

The strong, bony skull provides the most important brain protection layer. The skull structure consists of three layers the outer table, the diploe, and the inner table. The outer and inner tables are constructed of dense, compact bone. The diploe region is a weaker, porous

structure that contains many fluid-filled interconnected cavities. Inclusion of three skull layers, each with their own properties, is a meaningful improvement over previous single-layered skull head impact models.

The meningeal region (dura mater is the most significant sub-. structure) is a physically tough and leathery layer which might affect the wave reflections inside the skull. Also the dura provides penetration protection to the brain against the bony interior skull ridges. Ommaya (1968) demonstrated that piercing of dura occurred at 50% of the force level required to penetrate human skin. To date, there have been no experimental evaluations of the structural proper- ties necessary to define the behavior of the meningeal region. Therefore, it is impossible to establish an approximate description of this portion of the head. Additionally, the potentially complex constitutive relationships that might govern the structural nature of the meninges would add substantial difficulties to the mathematical formulation. Presently no meningeal layer is included; however, the need for further evaluation of this region is clearly recognized.

Head impact in the absence of cerebrospinal fluid (CSF) was shown by Ommaya (1968) to result in concussion with very low energy blows. Because CSF is rather inviscid, it can not act as a viscous shock ab- sorber. The protective role of CSF seems to be filling the portions of the cranial vault not filled with brain tissue so that the entire internal cavity remains without void space. Engin and Liu (1970) discuss the similar densities of brain and CSF (1.150 gm/cm^3 to 1.007 gm/cm^3). In addition, the bulk modulus of brain and CSF are

both approximately that of water ($2.07 \times 10^{10} \frac{dynes}{cm^2}$). Mathematically, CSF and brain can be considered to be a single continuous structural substance. Physically, however, if the theoretical analysis predicts dangerous mechanical forces at the extreme outer brain radius, then the CSF and not the brain will be damaged.

The theoretical model consists of the three bony skull layers and the brain region. A physical impactor (not an arbitrary input function) is included to yield a more realistic impact analysis. Solutions to both one and two-dimensional formulations are presented.

One-dimensional analyses are typically simpler and less expensive than two-dimensional analyses. The one-dimensional head impact model does not include the important closed container geometrical effects of a spherical model. However, the wave propagation influences of a layered structure with various material properties can be mathematically determined. In general, the one-dimensional computer analysis provides an economical method of investigating several parameter variations within the basic layered head impact formulation. In addition, the flat plate model can be compared to continuum and lumped parameter one-dimensional analyses.

One-dimensional particle motion requires eliminating edge effects by having layers that are wide in comparison to the thickness. The multi-layered flyer-plate class of formulations satisfies the general problem description. Figure 2 shows the one-dimensional impactor, skull layers, and brain region. All layer thicknesses for the head are approximately equal to the anatomic values. Because exact one-dimensional geometrical thicknesses are not of critical significance,

a larger skull to brain thickness ratio was used to provide a shorter problem and more economical computer cost. The assumed sizes for impactor, total skull, and brain layers are 5.0, 1.5, and 10.0 cm, respectively.

The cranial vault (brain containing skull structure) appears to be ellipsoidal in shape. Most coronal cross-sections are basically circular, while the sagittal and transverse cross-sections have the appearance of an ellipse. It is assumed that a spherical model will provide a geometrically simplified, but meaningful approximation of the head shape. The two-dimensional layered head impact model is shown in Figure 3. The impactor is assumed to be moving in an axial direction along the symmetry axis. Also the head and impactor lie on the same axis of symmetry. All layer thicknesses and, therefore, radii are approximately equal to the average anatomic values. The frontal and occipital skull regions are used to determine skull thickness values, because these are the most frequent sites of impact injury and because blows to the thinner temporal regions might produce fracture more readily. The radial thicknesses of the impactor, total skull, and brain are 5.0, 1.1 and 14.0 cm, respectively.

Material Property Definitions

A microscopic view of bone reveals long thin collagen fibers embedded in a hard crystalline matrix of hydroxyapatite. This description suggests that bone materials behave as a transversely isotropic specimen. Also a realistic analysis of brain tissue would indicate that it is an anisotropic and inhomogeneous material. Ideally, one would like to include anisotropy and inhomogeneity in a

BRAIN

OUTER TABLE
DIPLOE
INNER TABLE

LINE OF SYMMETRY

IMPACTOR

Figure 3. Cross-section of two-dimensional
multi-layered skull-brain model.

IMPACTOR

OUTER TABLE
DIPLOE
INNER TABLE

BRAIN

INNER TABLE
DIPLOE
OUTER TABLE

Figure 2. Cross-section of
one-dimensional multi-layered
skull-brain model.

head model; however, the likelihood of obtaining a solvable formula-
tion of such a model is small. Therefore, the present model assumes
all materials behave isotropically and homogeneously.

Isotropic materials have three constants in the constitutive
(stress-strain) equations. Only two material constants are inde-
pendent (Chou and Pagano (1969)). The formulations presented for
one- and two-dimensional analysis require knowledge of the bulk
sound speed (directly related to bulk modulus), Poisson's ratio,
and density.

The mechanical properties assigned to each of the skull layers
and the brain are based, in general, on the best available experi-
mental head materials evaluation. In 1968, Ommaya surveyed publica-
tions on the mechanical properties of the nervous system. He reported
that only three papers on brain tissue properties had been presented.
Also, very scant findings were given for the other constituents of
the nervous system. Under recent contracts supported by the National
Institute of Neurological Diseases and Stroke, the West Virginia Uni-
versity Biomechanics Laboratory, and the Michigan University Highway
Safety Research Institute have investigated many aspects of the material
behavior for scalp, skull, dura, and brain tissue. The following dis-
cussion is a brief summary of the pertinent results of these and other
material property studies.

The inner and outer tables are of similar construction and are
assigned the same property values. Melvin, Fuller, and Barodawala
(1970) indicate, in a density curve for the entire skull, that the
table density is 1.94 gm/cm^3. While not specifically evaluated for

the compact tables, the Poisson's ratio is approximated as 0.3.
The West Virginia University investigators measured a sound wave
velocity in compact bone of 3000 meters/sec. An elastic modulus
of 2.07×10^{11} dynes/cm^2 at a strain rate of 100 cm/cm/sec was
obtained by Wood (1971). It is interesting to correlate the
material parameters of sound speed (C_o), bulk modulus (K), density
(ρ), Poisson's ratio (ν), and elastic modulus (E). The computer
impact wave propagation analysis utilizes the input values C_o =
3000 meters/sec, ρ = 1.94 gm/cm^3, and ν = 0.3. The following equa-
tions are valid for isotropic materials:

$$K \approx \rho C_o^2 \tag{1}$$

$$\text{and } E = 3K(1-2\nu). \tag{2}$$

Substituting the input values into equations (1) and (2) the elastic
modulus is computed as 2.10×10^{11} dynes/cm^2, which is nearly equal
to the experimentally determined value.

Slight strain rate dependence has been demonstrated for hard
femur bone (McElhaney and Byars (1965). In testing the human skull,
the workers at West Virginia University Biomechanics Laboratory suggest
a certain degree of rate sensitivity in the fresher samples. Wood
(1971) demonstrates linear regression curves to show strain rate de-
pendence of the elastic modulus, breaking stress, and breaking strain
for compact cranial bone. The elastic modulus increases by only 55%
as the strain rate increases by 4 orders of magnitude (.01 to 100).
Therefore, the equivalent of the highest value for elastic modulus
is used as a constant, and the material properties for bone are not
considered to be strain rate dependent.

Random variations in diploë thickness do not have a functional
relationship (West Virginia University Biomechanics Laboratory (1970)).
The large standard deviation computed by McElhaney, Fogle, Melvin,
Haynes, Roberts, and Alem (1970) suggests that the use of mean thick-
ness and mean material property values for the diploë might lead to
large variations between impact sites and between different individuals.
The best approximation for average properties was utilized in this
analysis.

Melvin et al. (1970) present graphic relations of compression
modulus versus diploë density. Using average density values, the
elastic compressive modulus is 1.38×10^{10} dynes/cm^2. The Poisson's
ratio is reported as high as 0.28 (for biopsy specimens by West
Virginia University Biomechanics Laboratory (1970) and as low as 0.19
(by McElhaney et al. (1970). An average value of .25 is assumed for
the present model. Density values for diploë have been variously re-
ported from 1.25 to 2.03 gm/cm^3. The lower value (Melvin et al. (1970))
will again be used to maintain consistency.

Diploë sound speed measurements have resulted in paradoxical con-
clusions. An initial study by West Virginia University Biomechanics
Laboratory (1970) and Martin and McElhaney (1971) shows the diploë
wave speed to be faster than that in the tables. The volumetric
porosity of the tables is about .38 (large number of tiny holes) com-
pared to a value of .56 for the diploë (smaller number of large holes).
The West Virginia University Biomechanics Laboratory researchers re-
peated their material evaluation and developed a porosity dependent

sound speed equation. The latter experiments showed the more physical-
ly predictable result of a lower sound speed in the diploë region.
Using the statistical parameters suggested in the West Virginia model,
the sound speed is computed as 2750 meters/sec.

The compressive failure strength for the initial crushing of the
diploë is shown by Melvin et al (1970) to be only 4.137×10^8 dynes/cm^2.
This relatively low value suggests that the diploe might crush or ex-
hibit plastic deformation during impact. Also the crushing diploë
struts, which form the porou. structure, can only deform until the
cavities disappear and the diploe becomes a solid region. McElhaney
et al (1970) suggest a 3 percent total strain over the entire skull
cross-section as a final crush-up strain. If the 3 percent level is
modified to express the fact that only the diploë region is crushing,
then the final strain is approximately 10 percent. Therefore, a crush-
up stress level is given by 1.38×10^9 dynes/cm^2.

There is some question as to the effect of strain-rate on the stress-
strain relationships for the diploe. Melvin et al (1970) indicate very
little scatter of the various rate-dependent data points in compressive
tests on diploe. However, anatomical observations indicate that the
fluid-filled diploe cavities might result in strain-rate dependence
in the *in-vivo* skull. Because rate-dependent effects are probably not
as important as the crushing effects, a simpler rate-independent diploe
model is used for the initial analysis.

Several mechanical aspects of brain tissue have been evaluated.
These areas of investigation include parametric stress-strain relation-
ships, bulk modulus and sound speed measurements, and shear modulus

testing. An equation relating stress to strain and strain-rate was
determined from compressive tests performed by Estes and McElhaney
(1970). Galford and McElhaney (1970) tested brain specimens for
creep compliance and stress relaxation. The four lumped parameters
of a Maxwell-Kelvin model are found which best fit the creep compli-
ance results. Driving point impedance characteristics of the head
were used by Stalnaker, Fogle, and McElhaney (1970) to define the
parameters for a mass, spring, damper head model.

The viscous damper coefficients described in the above investiga-
tions are not appropriate for wave propagation analysis require in-
stantaneous vs. equilibrium modulii as determined from the Hugoniot
curves. A strain-rate dependent brain constitutive equation is in-
corporated in the one-dimensional model, but the necessary modulii
are only roughly approximated in the absence of experimental data.

West Virginia University Biomechanics Laboratory (1970) reported
an average human brain density of 1.05 gm/cm^3 and a bulk modulus of
2.10×10^{10} dynes/cm^2. Rhesus monkey brain sound velocity was 1550
meter/sec and varied only slightly when measured across different
head diameters. Using the above for K and ρ in equation (1), the
sound velocity in human brain is computed to be 1450 meter/sec.

A statement by West Virginia University Biomechanics Laboratory (1970)
(unsupported by tabular or graphic data) claims the dispersion in
brain tissue to be very small (5.5%) up to 300KHz. Therefore, the bulk
properties of sound and modulus are essentially invariant with increas-
ing frequency. The 1450 meter/sec sound speed for the two-dimensional
model approximates the value used in previous two-dimensional head

impact models. The bulk sound speed in the one-dimensional model was assumed to be equal to the high frequency shock wave value reported for water in the Dynamic Materials Property Library (Lawrence, et al (1968)). This dynamically determined higher speed (1893 meter/sec) was utilized before the non-dispersive brain statement was read. Because of the rather large expense in computer costs, the one-dimensional analysis was not rerun with the lower sound speed. While the one-dimensional computer results are not based on a completely accurate head model, the relative values are still meaningful and valid.

Fallenstein, Hulce, and Melvin (1969) vibrated at (10Hz) brain specimens between two parallel plates and determined the shear storage modulus to lie between $6-11 \times 10^3$ dynes/cm^2. A shear storage modulus increase from 8.28×10^3 to 1.38×10^6 dynes/cm^2 with frequency variation from 2 to 400 Hz was reported by Shuck, Haynes, and Fogle (1970). This result was obtained by combining the mathematical solution for torsional input to a circular cylinder and the experimental findings of torque supplied to a cylindrical brain sample. The graphic display of this data shows the shear modulus exponentially increasing with frequency (West Virginia University Biomechanics Laboratory (1970)). A linear extrapolation from 400 Hz to the characteristic frequency of 8300Hz yields a shear modulus of 5.50×10^7 dynes/cm^2. The use of an exponential relationship and a higher frequency of brain tissue loading imply that much higher values of brain shear modulus might exist during head impact.

The thread-like interwoven nerve cell and nerve fiber substructure which comprises the brain might attain a strong shear rigidity under

dynamic loading. The shear modulus of weakly cross-linked and dilute gel polymers increases by three to five orders of magnitude with increasing frequency (Ferry (1961)). It is interesting to note that most of the polymers reach a peak shear plateau of 1.0×10^{10} dynes/cm^2. If brain tissue performs in a similar manner, then its dynamic properties must be significantly modified from the low frequency properties. The elastic brain model utilized in the two-dimensional analysis has a shear modulus of 1.0×10^9 dynes/cm^2 which results in a Poisson's ratio of 0.475.

Janssen and Bowman (1970) used a very soft urethane (reported tear strength is zero) as a brain model for photoelastic modelling. The results showed stress waves propagating through the urethane before the rotational effects could have occurred. If the dynamic shear modulus was not higher than the low frequency value, then the urethane could not support shear and stress could not be photoelastically observed.

Shear failure of brain tissue from a rotational force is widely accepted as an injury mechanism in the millisecond time regime. As polymeric materials change from low to high shear modulus with increasing frequency, they also reach a glassy-transition state in which they are brittle. A new brain injury hypothesis is proposed here: during the initial impact response to a direct blow, brain tissue can be injured by a shear-normal fracture mechanism. This injury concept also serves to unify the influence of shear effects throughout the entire time scale.

Experimental Correlations

Several results of experimental head injury investigations have been discussed previously in the Time Scale and Injury Tolerance Criteria sections. Visual demonstrations provide improved understanding of damage mechanisms. A brief summary of optical observations of mechanical injury phenomena is presented in the following paragraphs.

Optical analysis can be accomplished by photoelastic and direct observation. Gross (1958) used high speed (4000 frame per second) photographs to show the existence of regions of cavitation in water-filled glass skulls. Pudenz and Sheldon (1946); Gosch, Gooding, and Schneider (1970); and Ommaya (1966) have considered acute experiments with animals which have had lucite and lexan calvaria implanted. After impact, the skull moves away from the site of the blow and the brain lags behind (Ommaya (1966)). The brain then swirls, while rotating about an axis passing through the head's center of gravity. The largest movements occur in the fronto-parietal region.

The photoelastic approach to experimental modelling of internal stresses during head injury began when Holbourn (1943) displayed pressure gradients in a gelatin-filled skull. Gurdjian and Lissner (1961) constructed a two-dimensional head model. When this model was impacted from any direction, shear stress concentrations appeared at the brain stem. Flynn (1966) used an outer ring of high modulus and inner disk of low modulus photo-elastic material to simulate the skull and brain, respectively. The recent work of Janssen and Bowman (1970) is the most thorough attempt at photo-elastic modelling. Realistic sagittal and coronal skull sections were used. The location

and magnitude of the delivered blow was shown to effect the resulting shear stress patterns in the brain. Also, the axis of head rotation was shifted while maintaining a similar striking force. Finally, the significance of dura attachments was demonstrated by including, and then eliminating, these attachments when molding the photoelastic model.

Photoelastic models of a skull cross-section were constructed by two research groups: Melvin et al (1970) and West Virginia University Biomechanics Laboratory (1970). These models used a solid photo-elastic material to represent the outer and inner tables and a region containing many holes to represent the diploe. In both studies, a static load was applied to the model. High stress concentrations were observed in the diploe region, indicating this area to be a site of potentially early failure.

The exploding wire dynamic photoelasticity laboratory at Drexel University provides the capability of observing wave propagation in birefringent models. An ultra high-speed (1μ sec between frame) framing camera photographs the event. Several aspects of theoretical modelling were studied experimentally to validate modelling assumptions and gain confidence in the general applicability of the two-dimensional analysis. Wave form and wave speed properties of flat plate table and diploe models were investigated. A concentric disk model of a layered skull and brain was impacted over a polar cap to simulate the theoretical two-dimensional model.

III - <u>THEORETICAL MODELLING</u>

The significant head layers and their properties for impact modelling have been defined in the previous sections. Theoretical one and two-dimensional models require the equations of motion for the given geometries be solved for the proper boundary and initial conditions. The geometric model shape is divided into a network of small grids. Finite difference analogs of the governing partial differential equations are solved in each of the grid zones. The result of satisfying all the equations in all the zones yields an approximate numerical solution for the head impact model.

Finite Difference Formulation and Solution

The one and two-dimensional solutions utilize Sandia Laboratory computer codes "WONDY IIIa" and "TOODY IV". The following mathematical descriptions of the formulation and computational procedures are based on reports by Lawrence (1970) and Benzley, Berthoff, and Clark (1969). Because the one-dimensional analysis is a degenerate form of the two-dimensional method, the details of the two-dimensional formulation are described. Whenever large deviations between the two models exist, then both methods will be explained.

"TOODY IV" is a Fortran computer code that solves the finite difference analogs to the Langrangian equations of motion in two dimensions. Limitation of the model to motion in two directions (essentially two independent spatial variables) does not preclude the presence of induced normal stress and strain in a third direction. The semi-circular, two-dimensional model shown in Figure 3 is representative of either a cylindrical or spherical cross-section. The sphere of revolution is

obtained by rotating the circular cross-section about its axis of symmetry. Both geometrical configurations are shown in Figure 4. A computer input parameter α determines the desired shape ($\beta=1$ implies a cylindrical geometry and $\beta=2$ implies a spherical shape).

Shell or plate theories are not incorporated into the formulation. The exact equations of motion are solved by satisfying the laws of conservation of linear momentum, mass, and energy. Also required are the constitutive and strain rate - velocity equations. Conservation of linear momentum in the x and z directions is expressed as

$$\rho \, a^x = \frac{\partial T^{xx}}{\partial x} + \frac{\partial T^{xz}}{\partial z} + (\beta-1) \frac{T^{xx} - T^{yy}}{x} \tag{3}$$

$$\rho \, a^z = \frac{\partial T^{xz}}{\partial x} + \frac{\partial T^{zz}}{\partial z} + (\beta-1) \frac{T^{xz}}{x} \tag{4}$$

where ρ is density

  a is acceleration in the given direction

  T^{xx} is normal stress in the x direction

  T^{yy} is normal stress in the y direction

  T^{zz} is normal stress in the z direction, and

  T^{xz} is shear stress in the x-z plane

The conservation of mass equation is given by

$$\rho dv = M \tag{5}$$

where M is mass in an element, and

  dv is instantaneous volume of an element

Energy conservation is described as

$$\rho \, \frac{\partial E}{\partial t} = P_s + P_d \tag{6}$$

where E is internal energy per unit mass

  P_s is rate of work done by pressure against a volume change, and
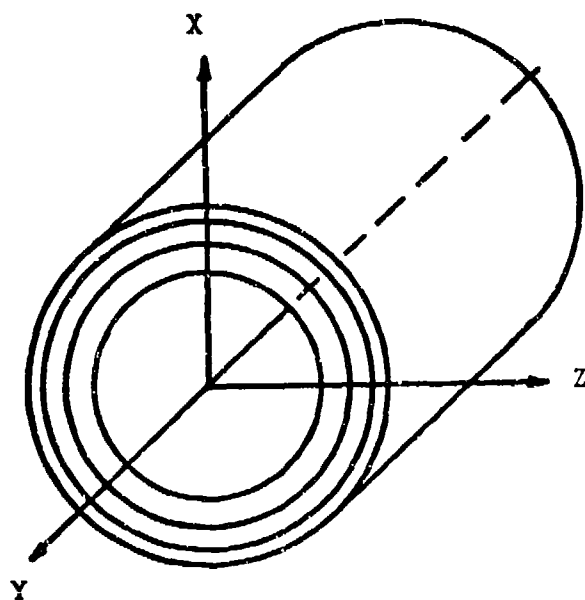
a. Cylindrical
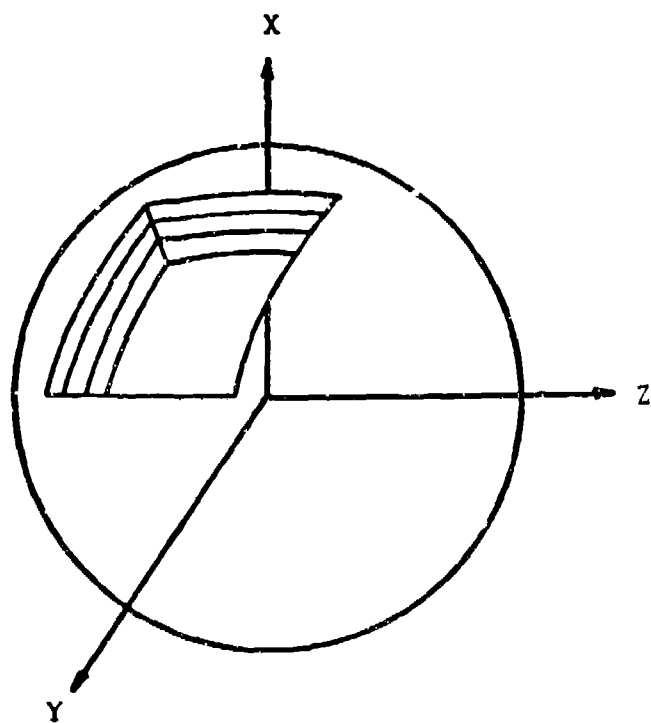
b. Spherical

Figure 4. Geometrical Configuration of Two-Dimensional Models

P_d is rate of work done by deviator stress against distortion

The strain-rate, velocity equations are expressed as

$$d^{xx} = \frac{\partial u^x}{\partial x} \tag{7}$$

$$d^{zx} = d^{xz} = \frac{1}{2} \left(\frac{\partial u^x}{\partial z} + \frac{\partial u^z}{\partial x} \right) \tag{8}$$

$$d^{zz} = \frac{\partial u^z}{\partial z} \tag{9}$$

$$d^{yy} = (\beta-1) \frac{u^x}{x} \tag{10}$$

where d^{xx}, d^{yy}, d^{zz} is normal strain rate in the given direction

d^{xz} is shear strain rate in the x-z plane, and

u^x, u^z is velocity in the given direction

Equations (3) - (10) must be satisfied for all layers of the models. An additional equation is required, but this constitutive equation is specified independently for each individual layer. All constitutive relationships are defined in the following section entitled "Constitutive Equations".

"TOODY IV" defines the approximate spatial derivative of an arbitrary variable function (ψ) of x and z as

$$\frac{\partial \psi}{\partial x}_{\text{Average}} = -\frac{1}{A} \oint_c \psi \, dz \tag{11}$$

$$\frac{\partial \psi}{\partial z}_{\text{Average}} = \frac{1}{A} \oint_c \psi \, dx \tag{12}$$

where c is integration path for line integral ($\oint$), and

A is area enclosed by path.

For example, using the coordinates in Figure 5, the value of a derivative

required for equation (3) or (4) (with c equal to A-B-C-D-A and area ABCDA equal to A) is given by

$$\frac{1}{\rho}\frac{\partial T^{xx}}{\partial x} = -\frac{1}{\rho A}\left[T_1^{xx}(Z_a-Z_d) + T_2^{xx}(Z_b-Z_a) + T_3^{xx}(Z_c-Z_b) + T_4^{xx}(Z_d-Z_c)\right] \quad (13)$$

where T_1^{xx} is the value of T^{xx} for quadrilateral 1, etc.
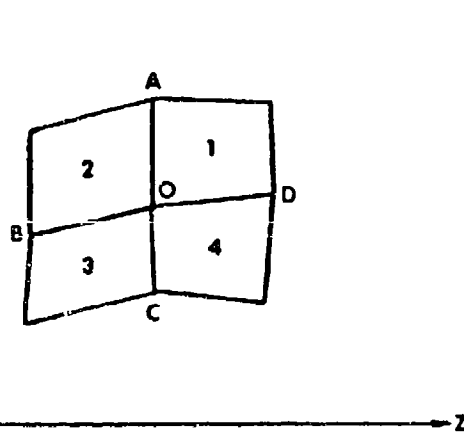
Figure 5. Grid zone description for finite difference algorithm.

The value of ρA is obtained by averaging the values of the neighboring regions to yield

$$\rho A = 2\left(\frac{1}{4}(\rho_1 A_1 + \rho_2 A_2 + \rho_3 A_3 + \rho_4 A_4)\right) \quad (14)$$

where ρ_1 and A_1 are the average density and area of quadrilateral 1, etc.. Other areas or variable values required are also determined by linear inter-polation and averaging techniques.

Time derivates are set in finite difference form by direct use of a simple, second order, centered difference analog as follows:

$$\left[\frac{\partial \psi}{\partial t}\right]^{n+1/2} = \frac{\psi^{n+1} - \psi^{n}}{t^{n+1} - t^{n}} \tag{15}$$

where the superscripts denote the value of ψ and time at the prescribed time increments $(n, n + \frac{1}{2}, n + 1)$.

"WONDY-IIIa" uses a centered difference analog for spatial as well as time derivatives. If the subscripts j, $j + \frac{1}{2}$, and $j + 1$ represent the end points and midpoint of the jth spatial zone, then

$$\left[\frac{\partial \psi}{\partial x}\right]_{j+1/2} = \frac{\psi_{j+1} - \psi_{j}}{x_{j+1} - x_{j}} \tag{16}$$

Linear interpolation expressions for time and spatial zones are also utilized in determining the final difference equations. The complete finite difference system of equations for "WONDY-IIIa" and "TOODY-IV" is presented in Appendix A.

All physical materials and boundary regions are defined by "TOODY-IV" as projections on a rectangular index space. The column (i) and row (j) identification of each zone is fixed for easy referencing. The same material particles are always contained in a given zone (a requirement of the Lagrangian system of equations). There is no limitation on the motion and distortion allowed for any zone. Variables in mesh 3 (see Figure 5) are stored with the same index as that applying to point 0. At a given time and location, the variables are all being solved for the value at point 0.

In addition to the equations of motion, the formulation must satisfy the proper boundary and initial conditions. The initial values for all variables

are determined by input card parameters. The boundary criteria are established by defining a one zone layer that has the desired boundary effects. Figure 6 shows the index space required to model the impactor, three layered skull, and brain. For example, along the symmetry axis a symmetry line is defined which in the "TOODY IV" code automatically creates the mathematical conditions for allowing motion parallel to the axis but no motion in the normal direction. Analogous techniques are utilized at the outer radius of the skull by including a free surface description. The slide line allows different nodal points to exist on both sides of the same physical line. Slippage along the slide line is not permitted in the brain region, but the impactor can slide along the skull surface. Also the boundary layers are defined as free surface and symmetry (a symmetrical axis line).

A physical shape is assigned to the material meshes by using a system of transformation relationships. The impactor, skull, and outer brain regions (labelled regions 1, 2, 3 and 4) are described by the following equations

$$R = r_0 - r_1 (i-i_0) \tag{17}$$

$$X_{j,i} = R\sin (w_0 - w_1 (j-j_0)) + X_0 \tag{18}$$

$$Z_{j,i} = R\cos (w_0 - w_1 (j-j_0)) + Z_0 \tag{19}$$

where r_c, r_1, w_1, x_0, z_0 are non-dimensional input constants that are specified for each layer. With a proper choice of input values, two adjacent regions with a different number of rows can be equal in length. Effectively the column (i) locations determine the radius and row (j) locations sweep out the angle. Because the impactor and head model are assumed to have a mutual axis of symmetry, only one hemisphere (a semi-circle in cross-section) is analyzed. The results in the opposite hemisphere are directly available as the symmetric image of the portion that is analyzed. Figure (7) shows the
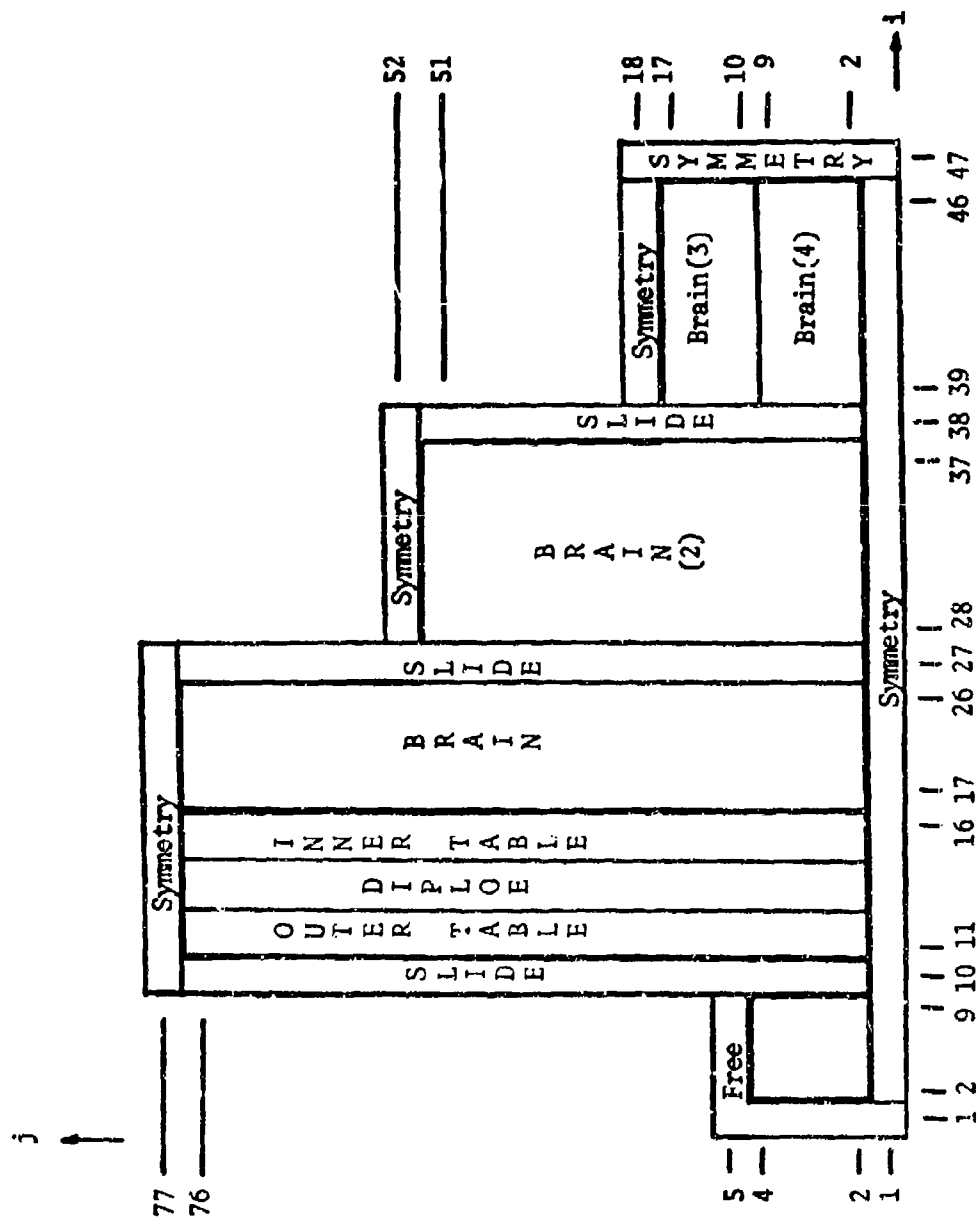
Figure 6. Index (i,j) Space for Multi-layered Spherical Model
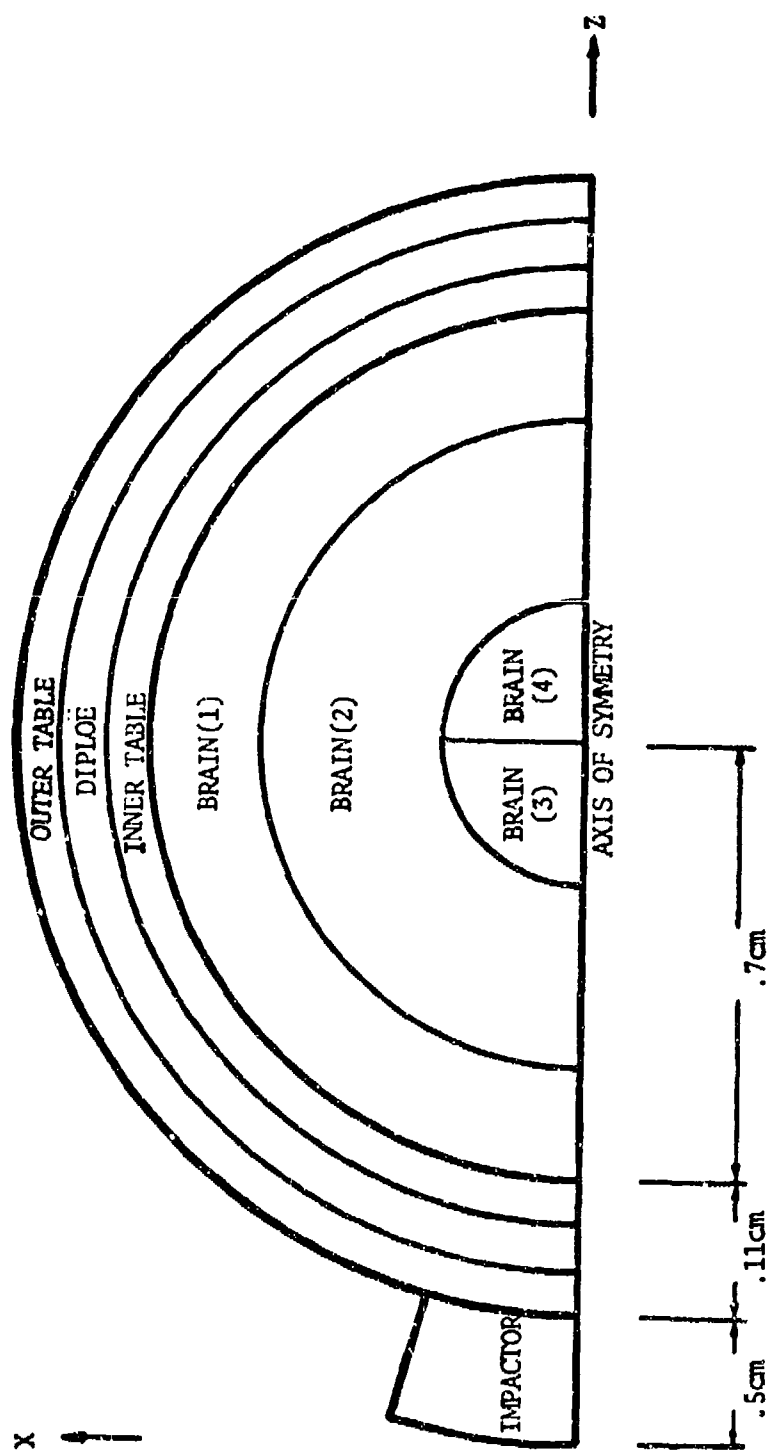
Figure 7. Physical (X,Z) Space for Multi-layered Spherical Model

cross-sectional view of the layered hemisphere model for head impact.

The central regions in Figure 7 cannot be obtained from equations (17)-(19). Figure 8 shows the transformation that exists between the index and physical space for the left side of the central region. While point 4 in the index space is surrounded by the normal rectangular zone, the same point 4 in the physical space is part of a triangular grid. The standard computations used for all zones would result in an undefined solution at that location, because the zero length of one side of the zone would result in division by zero. This computational anomaly was resolved by using a linear interpolation based on the neighboring nodes as the value for the motion of point 4.
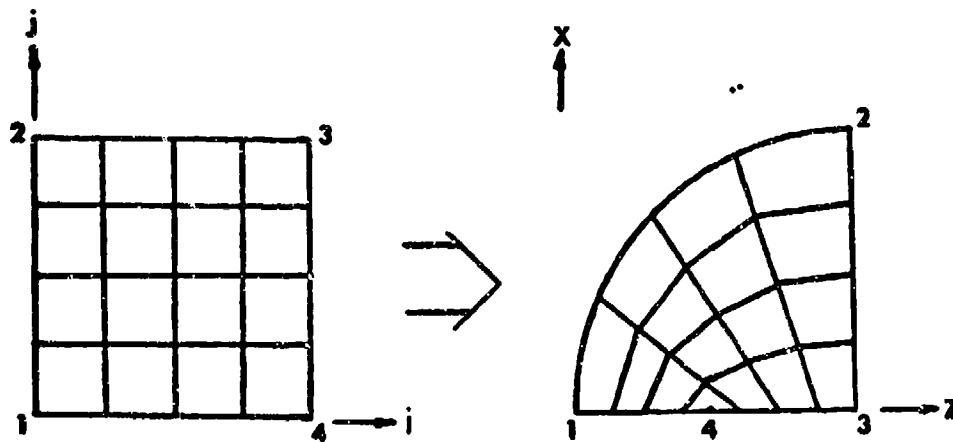
Figure 8. Transformation from Index to Physical Space for the Central Zones

With all zones defined, the computation proceeds as follows. At time=0, the initial values define all variables in all i, j zones. The time is then incremented by the appropriate initial time step (Δt). At t=Δt, the new values for all quantities are determined in the 1st column (i=1), 1st row in 1st column (j=1) zone. Then the row identifier is advanced until the entire 1st column has been solved at the new time. The 2nd column is then advanced to the new time, etc., until all meshes have been completed. The time is now incremented by a new time step, and the procedure continues until the problem is completed at a predetermined final time.

An important aspect of finite difference methods for studying wave propagation has not been discussed. Due to material non-linearities, compressive waves tend to steepen into shock discontinuities. A finite difference scheme requires that variable values change by small amounts within a given zone; therefore, the infinite shock slope would yield invalid computations. Extremely small mesh sizes could provide finite changes in the shock vicinity, but the cost of running even a short problem would be prohibitive. Artificial viscosity is introduced to insure that lower gradients exist and that the finite difference algorithm are valid. It should be noted that artificial viscosity only operates in the presence of compression waves, not rarefaction waves. Two forms of artificial pressure (q) are incorporated. A quadratic viscosity is given by

$$q = \rho \, b_1^2 \, \left(\frac{1}{\rho} \frac{\partial \rho}{\partial t} \right)^2 \tag{20}$$

where b_1 is an assumed constant length. The quadratic viscosity is extremely rate dependent and is effective near shock gradients. A linear viscosity which controls small spurious oscillations is given in the form

$$q = b_2 \, C \left(\frac{\partial \rho}{\partial t} \right) \tag{21}$$

where b_2 is assumed constant length, and

C is sound speed.

Deviator components of artificial stress are available but not used in the present model. The values computed from (20) and (21) are summed to yield a resultant total artificial pressure. In the linear momentum and energy equations (3), (4) and (6), the viscous stress values are added to the true stress to obtain the final system of equations.

The constants b_1 and b_2 are modified to form non-dimensional constants B_1 and B_2. The values of $B_1 = 1.2$ and $B_2 = .06$ were used as suggested by Benzley, et al (1969). A sample problem (using "WONDY-IIIa") with low values for the artificial viscosity constants was computed. The general result was that the stress and energy output was the same for normal and low constant values. At points near the compressive wave peaks, the stress and energy was less than 4% lower with the normal values of B_1 and B_2. Because the results were nearly equivalent, the normal values were used to protect the difference formulation from invalid computations near a potential shock wave.

Constitutive Equations

The material property survey (in the Material Property Definitions section) suggests that several combinations of stress strain relations might exist within the multi-layered head impact model. Because the stress levels in the skull region for this analysis are below the yield point for compact bone, the inner and outer tables are always represented as exhibiting a linear (elastic) stress-strain behavior. The collapsing diploë region is described by two models: (1) a material that has plastic yielding beyond a given elastic stress limit and (2) a crushable hydrodynamic foam. Most of the skull models utilize a water-like hydrodynamic brain representation.

However, two additional constitutive relations were considered (1) a strain rate dependent stress version and (2) an elastic model which includes shear stress.

Several relationships are required to determine the pressure and stress components for a particular material behavior. Lee (1969) suggests that in cases of high impactor velocity (with resulting pressures above 50 KBar) the equation of state must include an energy dependent thermodynamic term. "TOODY-IV" uses the Mie-Gruneisen equation to express pressure as a function of density and energy in the following form.

$$P - P_h = \Gamma(E - E_h)\rho \qquad (22)$$

where Γ is Gruneisen ratio

P_h is reference pressure along the Hugoniot, and

E_h is reference energy along the Hugoniot.

The relatively low impactor speed and the dearth of energy dependent high speed data on skull and brain tissue indicate that an energy independent (theory of elasticity) analysis is the only potentially successful approach. To show the accuracy of using energy independent constitutive equations, a sample problem was analyzed in one-dimension with an impactor striking a head which had a skull with aluminum properties. The energy dependent part of the equation of state is given by

$$p = \rho \Gamma E \qquad (23)$$

In the sample problem the experimentally determined aluminum constants were available from Lawrence, et al (1968). For aluminum the Gruneisen ratio is 2.1 (typical range for metals to water is 3.0 to 1.0). The results of this sample problem showed the energy dependent pressure term to be less than 1% of the pressure component from the energy independent elasticity calculations.

The energy independent form of the equation of state is given by

$$p = K_0 \eta \tag{24}$$

where K_0 is adiabatic bluk modulus at zero pressure

η is $1 - \rho_0/\rho$, and

ρ_0 is density at zero pressure.

Equation (24) is directly analogous to the theory of elasticity relationship (see Chou and Pagano (1969))

$$p = K_0 \epsilon \tag{25}$$

where ϵ is the volumetric strain.

The following deviator equations must be used to compute the stress components

$$T^{xx} = {}^d T^{xx} - p \tag{26}$$

$$T^{xz} = {}^d T^{xz} \tag{27}$$

$$T^{zz} = {}^d T^{zz} - p \tag{28}$$

$$T^{yy} = -3p - T^{xx} - T^{zz} \tag{29}$$

where the terms preceded by the superscript "d" are the deviator stress components. In equations (26) - (29) the artificial pressure terms are added to the right-hand-side in order to compute the stress components. If the material is hydrodynamic (zero deviator streee) then, for example, equation (26) yields that the normal stress (T^{xx}) is equal to the negative of the pressure. The water-like brain model is hydrodynamic in behavior.

For an elastic-plastic material the stress deviators are non-zero. The stress (or stress-rate) deviators are computed by applying Hooke's Law to the strain (or strain-rate) deviators. The strain-rate deviators $({}^d d^{xx}, {}^d d^{yy},$

d_d^{zz}, d_d^{xz}) are defined by

$$d_d^{xx} \equiv d^{xx} + \frac{1}{3}\frac{1}{\rho}\frac{\partial \rho}{\partial t} \tag{30}$$

$$d_d^{zz} \equiv d^{zz} + \frac{1}{3}\frac{1}{\rho}\frac{\partial \rho}{\partial t} \tag{31}$$

$$d_d^{yy} \equiv d^{yy} + \frac{1}{3}\frac{1}{\rho}\frac{\partial \rho}{\partial t} \tag{32}$$

$$d_d^{xz} \equiv d^{xz} \tag{33}$$

From plasticity theory the deviator strain-rate is divided into an elastic part ($d_{d_e}^{xx}$) and a plastic part ($d_{d_p}^{xx}$) given (for example) as

$$d_d^{xx} = d_{d_e}^{xx} + d_{d_p}^{xx} \tag{34}$$

Stress and stress-rate are related to the elastic scrain and strain-rate (respectively) via Hooke's Law. The deviator parts of the stress-rate are described as.

$$\frac{\partial d_T^{xx}}{\partial t} - 2w^{xz}d_T^{xz} = 2G d_{d_e}^{xx} \tag{35}$$

$$\frac{\partial d_T^{xz}}{\partial t} + w^{xz}(d_T^{xx} - d_T^{zz}) = 2G d_{d_e}^{xz} \tag{36}$$

$$\frac{\partial d_T^{zz}}{\partial t} + 2w^{xz}d_T^{xz} = 2G d_{d_e}^{zz} \tag{37}$$

where G is shear modulus, and

w^{xz} is rigid body rotation

The finite difference form of equations (35) - (37) can be solved explicitly for the stress deviators at time n+1.

If the material exhibits plastic behavior, then there is an upper limit to the deviator stresses which is determined by the yield condition. A typical

yield criterion is the well-known von Mises relationship (Mendelson (1968))

$$\frac{1}{6}[(T^{xx}-T^{yy})^2+(T^{yy}-T^{zz})^2+(T^{zz}-T^{xx})^2+6(T^{xy2}+T^{yz2}+T^{zx2})] \leq \frac{1}{3} y^2 \qquad (38)$$

where y is the flow stress in uniaxial stress. Transforming this relationship into deviator stress terms and substitution of equation (30) for T^{yy} yields

$$2\{(^d_T x^x)^2 + (^d_T x^z)^2 + (^d_T z^z)^2 + (^d_T x^x)(^d_T z^z)\} \leq \frac{2}{3} y^2 \qquad (39)$$

When plastic strain occurs, it is required to be normal to the yield surface. The yield stress (y) may vary due to strain hardening, strain-rate, or compression. However, in the present diploe modelling, y is assumed to be constant, and the material behavior is termed elastic-perfectly plastic.

The outer and inner tables develop deviator stresses but they do not exhibit plasticity. This perfectly elastic condition is accomplished by assuming an effectively infinite yield flow stress. One diploe and one brain model also utilize a perfectly elastic formulation. The former case produces a skull model that behaves as a single linear elastic shell which serves as a baseline for comparison with other diploe models studied here and previous investigations by others.

The collapsing diploe cavities can also be modelled as a crushable foam. The equation of state for hydrogynamic foams or distended solid materials is described by Herrmann (1968) and Lawrence (1970). A parameter, α, describing the degree of distention of the foam is defined as

$$\alpha = \frac{\rho_s}{\rho} \qquad (40)$$

where ρ_s is solid material density, and

ρ is distended material density.

The α parameter must vary to describe three separate material regions: (1) initial elastic distended region; (2) crushing distended region; and (3) final elastic solid region (after final crushing). At the boundaries between these regions certain continuity and smoothness conditions are imposed on the α parameter. During the crushing, the α parameter is assumed to vary quadratically with pressure. As in the case of the elastic-plastic constitutive equations, the pressure as well as the α parameter are chosen to be energy independent functions.

The rate dependent brain layer model is described by a visco plastic constitutive equation for one-dimensional wave propagation as described by Herrmann, Lawrence, and Mason (1970). The constitutive relation is

$$\frac{d\sigma}{dt} = \frac{d\sigma i}{dt} - 2Gg \tag{41}$$

where σ is total stress

σi is instantaneous stress, and

g is relaxation rate

Two of the terms in equation (41) are further defined by

$$\frac{d\sigma i}{dt} \equiv Fd \tag{42}$$

where F is local instantaneous modulus

d is volumetric strain rate,

and $\quad g = \dfrac{\sigma^i - \sigma^1 e}{G\, t_r}$

where σ^1 is total stress deviator

σ_c^1 is equilibrium stress deviator, and

t_r is relaxation time

All required moduli are computed within the program code from the input constants of density, bulk sound speed, and Poisson's ratio. If the relaxation rate is small, then there is not enough time for plastic stresses to develop. On the other hand, for large relaxation rates plasticity occurs so rapidly that there is not sufficient time for viscous over-stress to develop. In the absence of brain tissue experimental data, the relaxation time is approximated as one-tenth of the characteristic wave transit time in the brain. The one-tenth assumption is a physically meaningful value which will show the potential influence of viscous effects in the brain.

Stability and Accuracy

The "WONDY III-a" and "TOODY IV" computer codes provide error checks as well as a stability criterion. Herrmann, Holzhauser, and Thompson (1967) developed an approximate analytic method for determining a stable time step increment for equations of motion in uniaxial strain. Valid time increments are restricted by the following stability equations in "WONDY III-a"

$$\Delta t \leq \frac{\Delta x}{B_2 C + B_1^2 |\Delta u| + \sqrt{(B_2 C + B_1^2 |\Delta u|)^2 + C^2}} \quad \text{for } \Delta u < 0$$

$$\Delta t \leq \frac{\Delta x}{C} \quad \text{for } \Delta u \geq 0 \tag{43}$$

where B_1 and B_2 are artificial viscosity constants. A similar stability analysis has been extended to the two-dimensional "TOODY IV" code. Benzley, et al (1969) state that this criterion has yielded efficient and stable time steps for all problems heretofore solved.

Impactors cause large initial velocity gradients; therefore, a smaller Δt than required by equation (43) is used at the start of the calculation. As problem time progresses, the value of Δt is allowed to return to the increment computed by the stability equations.

Using velocity interferometer techniques, Lundergan and Drumheller (1971) achieved good correlation between experimental layered plate impact and analogous computations using WONDY III. Experimental verification of a TOODY III mathematical analysis is presented by Karnes and Bertholf (1971). Other experimental comparisons to these computer codes also indicate the general acceptability of the mathematical analyses.

The total internal and kinetic energy is computed for all meshes at the end of each cycle. A check is made to determine if total energy has been conserved while solving the equations of motion. An instability or accuracy error would result in an energy blow up or a stable but excessive error, respectively. "WONDY III-a" also checks momentum conservation by a similar procedure. Unfortunately the kinetic energy computation (only used in the error check) for the two-dimensional analysis is the least accurate approximation of the entire solution. For the complex geometry used, the "TOODY III" error check is a good measure of stability but not a good accuracy check. Computed errors of up to 12% were considered acceptable.

Another widely used method to verify that stability and accuracy have been achieved is to run the same finite difference analog with different grid zone sizes. If the two solutions are approximately equivalent (within a tolerable percentage difference), then the grid size is assumed to be acceptable. The head impact models were run with zone dimensions approximately one-third to one-half the original zone size. The output from the smaller zone sizes produced results which differed only slightly (less than 5%) from the larger

zone sizes. Therefore, the present choice of zone sizes provides a valid grid network for the finite difference formulation.

Non-Dimensionalization and Input Value Summary

"WONDY IIIa" and "TOODY IV" contain no internal dimensional constants; therefore, any self consistent set of units can be used. A properly non-dimensionalized system can be developed with respect to a characteristic velocity (u_r), density (ρ_r), and length (x_r). The resulting non-dimensional independent and dependent variables are given by

$$X^* = \frac{x}{x_r}$$

$$t^* = \frac{tu_r}{x_r}$$

$$\sigma^* = \frac{\sigma}{\rho_r u_r^2} \tag{44}$$

$$\rho^* = \frac{\rho}{\rho_r}$$

$$u^* = \frac{u}{u_r}$$

$$E^* = \frac{E}{u_r^2}$$

The present non-dimensional scheme is developed by considering the size and properties of the brain (in the one-dimensional analysis) as the characteristic values. These constants (based on the one-dimensional brain thickness, density and bulk sound speed) are given as $x_r = 10\,cm$, $\rho_r = 1.0\,gm/cm^3$, and $u_r = 1.893\times10^5\,cm/sec$.

The non-dimensional layer sizes are summarized in Table 1. Because of zone size considerations in the two-dimensional analysis, the single layered elastic skull has a dimensionless thickness of 0.10, while the total thickness for the layered models is 0.11. The impactor velocity is approximated by the free fall velocity of an object falling from a high shelf. This velocity is 9.465×10^2 cm/sec or 0.005 non-dimensional units. All other layer velocities are initially zero.

TABLE 1 - Non-Dimensional Head Model layer sizes

MODEL	IMPACTOR	TABLES	DIPLOE	BRAIN
ONE-DIMENSIONAL THICKNESS (cm)	0.5	0.05	.05	1.0
TWO-DIMENSIONAL THICKNESS (cm)	0.5	0.0363	0.0363	1.4

One previous spherical head impact analysis has considered a time and spatially dependent pressure input function. Benedict (1969) defines the time related portion of the pressure (p(t)) as

$$p(t) = 2500 \ (e^{-4.73 \ t^2/10^{-6}})(\sin(\pi/10^{-3}) \ t) \qquad (45)$$

The force applied to the head can be directly determined as the product of the pressure times the surface area of a 30° polar cap on the skull. The integral of this force-time curve (for an assumed one millisecond duration) is equal to the change of momentum of the impactor. Using the impactor velocity of 9.465×10^2 cm/sec, the equivalent mass required to produce the given force is

computed as 2520 gms. Assuming that an iron impactor (with dimensions de-
scribed before) is utilized in the mathematical two-dimensional model, the
impactor mass is calculated as 2290 gms. Therefore, the input energy is
approximately equivalent for the pressure function and impactor models.
While the force-time areas might be similar for the two input models, the
actual force duration and rise time is shorter for the impactor problem.
The one-millisecond duration pressure pulse is only attainable by consider-
ing the physical effects of a soft impactor (e.g. a padded dash). The im-
pactor model is a realistic descriptor for a blow delivered to the head model
presented in this work. Possible modifications to the impactor or head model
will be discussed in Chapter VI - Recommendations.

The present impactor model is more closely related to the dirac-delta
impulsive function utilized by Engin (1969), and Liu, et al (1971). The iron
impactor material properties are those given by Lawrence, et al (1968).

For convenient reference a summary of the important non-dimensional
material properties for the various head layers used in the two-dimensional
analysis are presented in Table 2. The elastic yield or initial crushing
value was decreased to one tenth of the experimental value. With the orig-
inal value, relatively small amounts of crushing occurred. A larger impact
energy would induce more crushing. Because the experimental value might
be lower in a dynamic test, it was more convenient to lower the initial
crushing value and use the same impact parameters. The overall effect is
to emphasize the energy absorbing protection provided by the skull. In
the one-dimensional model the crush-up strength was inadvertently set to a
value of 1.0 which gives a more gradual, less energy absorbing pressure-

distension curve than for the two-dimensional case. Also the flat plate
models utilize different brain properties which were described previously.

TABLE 2 - Summary of Non-Dimensional Material Properties for
Head Impact Analysis

NON-DIMENSIONAL MATERIAL PROPERTY	LAYER DESCRIPTION				
	tables and elastic diploe	elastic-plastic diploe	crushable diploe	hydro dynamic brain	elastic brain
density	1.94	1.25	1.25	1.05	1.05
bulk sound speed	1.60	1.467	1.467	.766	.766
Poisson's ratio	0.30	0.25	--	--	.475
elastic yield	∞	.00115	.00115	--	∞
crushup strength	--	--	0385	--	--

IV - RESULTS AND OBSERVATIONS

Theoretical Results

Computed results of the one and two-dimensional analyses of head impact are presented in condensed tabular and graphic form. The previously described non-dimensional units are used for all output variables. It should be noted that the results are based on the impact response with the assumed impactor size and velocity. Because of the high computer costs, no attempt has been made to determine if the general response characteristics of the skull-brain system are strongly dependent on the impactor parameters.

Several computer output dependent variables such as particle velocity, normal stress, shear stress, wave speed, and energy density at each spatial zone are available for each output time. These values can be plotted as variable versus position profiles at fixed times. Also a particular location can be used to obtain a variable versus time curve. The peak values and duration above a given cut-off level can be determined from these output displays.

When the one-dimensional analyses were performed, the computer software for automatic plotting was not available. Therefore, the one-dimensional output (dependent) variables were printed in both a complete and reduced form. The reduced output consisted of observing only seven locations within the brain region, but these new variable values were sampled every 0.1 non-dimensional time units. The complete output scheme printed the output variables for every spatial zone in the brain at every 2.0 units of time. With this latter output an accurate stress profile can be drawn from the complete spatial information. A sample stress profile in the brain is shown in Figure 9. This curve shows the positive tensile stress levels at every point
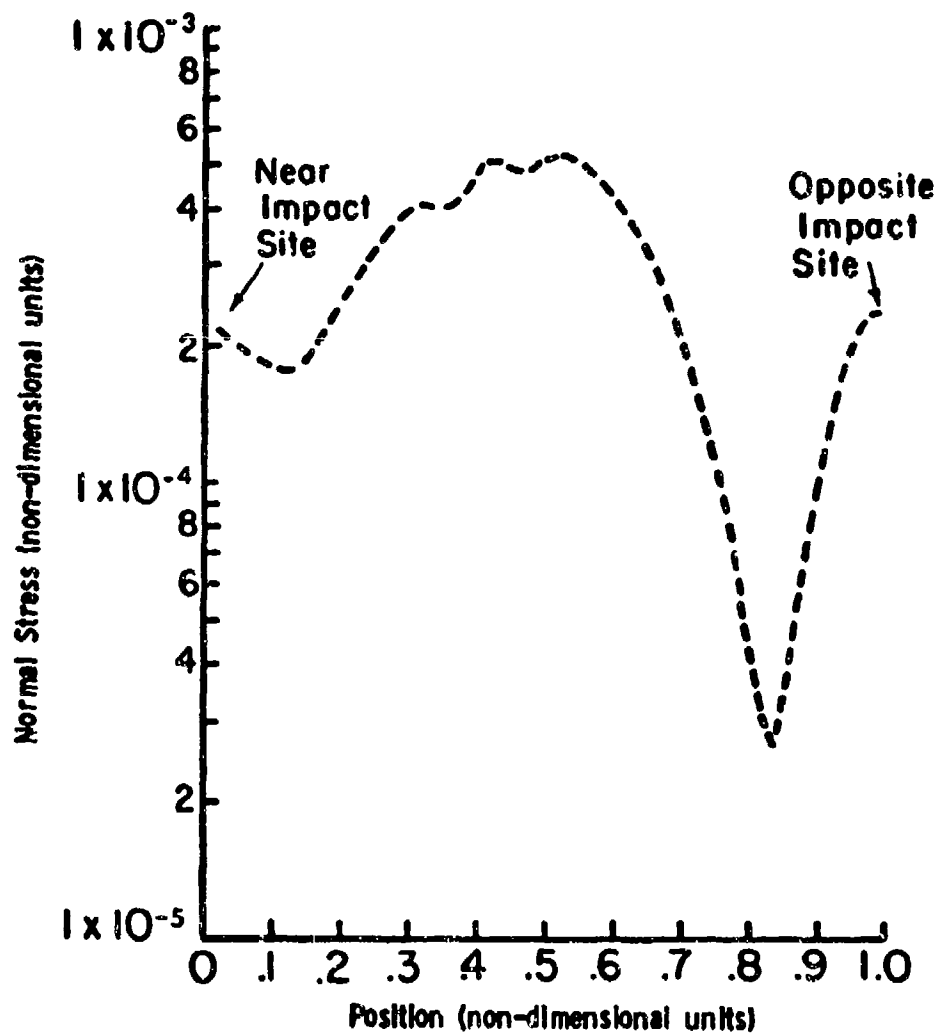
Figure 9. A stress profile in brain layer of
one- dimensional analysis for elastic-
plastic diploë model

in the brain layer at time equals 4.0 non-dimensional units. Tables of peak tensile stress values for each one-dimensional model are presented in Chapter V - Discussions.

A California Computer Plotting System was available when the two-dimensional analyses were performed. Detailed stress profiles and variables versus time curves are given in Chapter V - Discussions.

A single quantity which defines at each instant the overall brain response to an impact would provide a simple method of comparing the results of several models and serve as a link between continuum and lumped-parameter models. The internal energy in the entire brain region yields a measure of the stress-strain energy that has been transmitted to the brain. The total energy which equals internal energy plus kinetic energy was utilized for a portion of the one-dimensional analysis. Specific curves are presented in Chapter V - Discussions.

Experimental Observations

The analytic model provides the detailed mechanical results of a theoretical head impact, but there is a lack of experimental *in-vivo* evidence to correlate these mathematical computations to physiological events. The correlation of brain trauma to mechanics is not attempted in this present work; however, experimental models are developed which provide qualitative confidence in the analytic solution. Dynamic evaluation of two aspects of head impact phenomena have been considered: (1) wave propagation through a porous, three-layered skull, and (2) wave propagation in a simplified concentric ring model for head impact.

All experiments were performed at the Wave Propagation Research Center of Drexel University under the direct supervision of Dr. Joseph L. Rose.

The wave propagation experiments utilized the techniques of dynamic photo-elasticity. A brief summary of the test methods is discussed in the following paragraphs. A complete description of the test facilities can be found in papers by Rose and Chou (1970 and 1972). The photographic results are displayed in Chapter V - Discussions.

Pressure from an exploding wire can be used to impulsively load a thin plate photoelastic model of the layered skull, or of the entire head. The propagation of stress waves is photographed by a Beckman and Whitley Model 201 framing camera. The camera aperture was reduced in size to yield an exposure time of approximately .3μ sec. This short exposure minimized the blurring due to wave motion during the exposure period. The time duration between frames for the present testing is 1μ sec.

Light is made available from an E.G. and G. FX-1C-6 xenon flash tube. The xenon flash tube is mounted along the focal line of a cylindrical parabolic, chromium-plated reflector. Light from the flash tube and reflector then enters, in order, a polarizer, 1/4-wave plate, test specimen, 1/4-wave plate, analyzer, filter and camera.

The detailed model of the porous diploë layer of the skull is based on a photomicrograph by Melvin, et al (1970). Even the hard table regions have microscopic fluid-filled cavities. The effect of these tiny holes is modelled by several rows of small (.2 cm) drilled circular holes. Figure 10 shows a sketch of the two skull models (the second model was constructed with more diploë details to provide a lesser free path for wave propagation) and the reference material plates. The reference section provides measure-ments of undisturbed wave speeds for the solid and void filler. The disk and concentric ring head model is shown in Figure 11. Flynn (1966) constructed
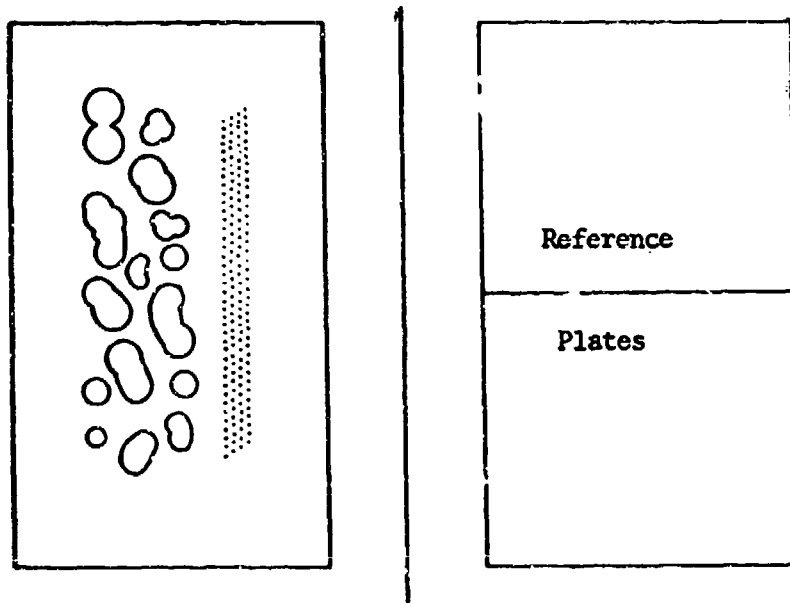
a. PL-2 Filler
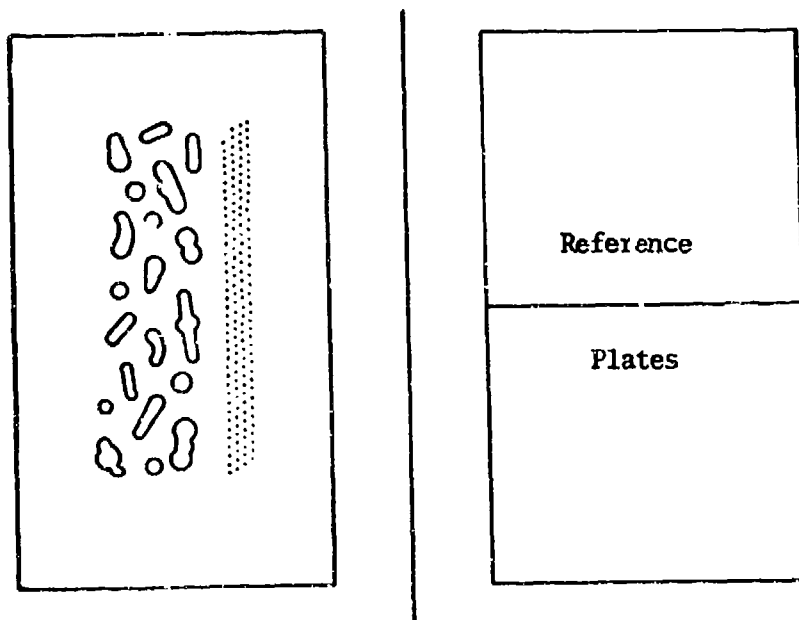
b. Solithane 113 Filler

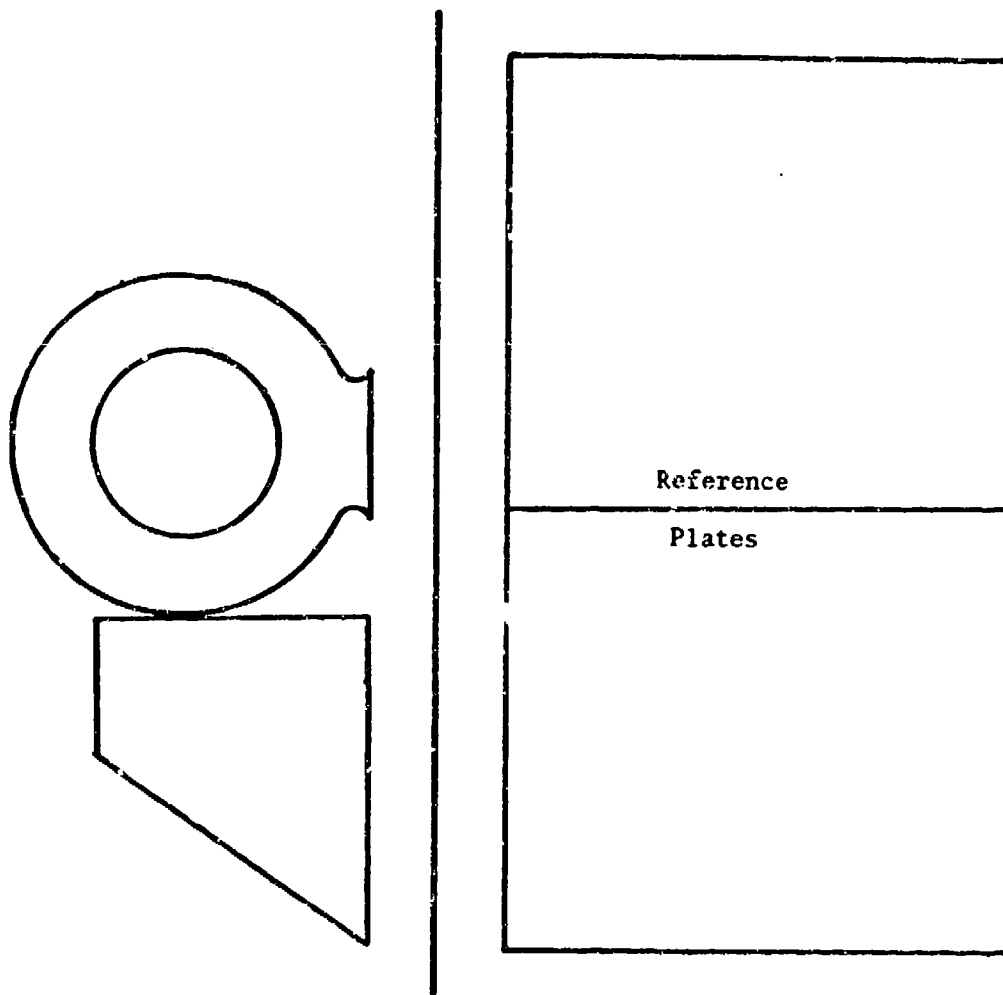Figure 10. Photoelastic Skull Model

Figure 11. Photoelastic Head Model

a similar model which broke after a few impacts. Therefore, the skull portion of the present head model was machined thicker than necessary for scaling to the anatomic size. Also a separate support bracket was supplied to prevent the specimen from sagging under its own weight.

The photoelastic model must have material properties which are similar to the corresponding regions of the head. In addition, the birefringent nature of the plastic specimens must produce readily observable stress-optical fringe patterns. Wave speed (plate velocity in these experiments) and acoustic impedance (wave speed x density) are the critical properties in wave propagation analyses. In the layered skull model the acoustic impedance at each solid-filler interface determines the proportions of reflected vs. refracted wave propagation. In the head model the relative wave speeds in the outer ring and central disk, also strongly influence the resultant wave motion. Several materials were utilized because of their material characteristics and their availability in the required solid sheet or castable form. Table 3 shows a comparison of the important wave propagation properties for the anatomic and plastic model materials.

The experimental values for the wave speeds in the photoelastic materials are determined by measuring the plate velocity for each material in the reference sheet. Because no two explosions are exactly the same, all wave speeds must be determined from the 12 photographs of a single test. By utilizing isotropic elastic constants, the bulk speed (C_0) may be computed. There is a discrepancy between the static property prediction of the bulk speed and the dynamic experimental values. The lack of knowledge

TABLE 3 - Material Properties of Head and Photoelastic Model Layers

Material	J	ρ gm/cm^3	K dynes/cm^2	Co meters/sec Computed	Co meters/sec Experimental	ρCo Computed	ρCo Experimental
[1]SKULL	.3	1.94	1.6×10^{11}	2871.	3000.	5450.	5820.
[1]BRAIN	--	1.05	2.1×10^{10}	1414.	1450.	1480.	1520.
[2]PSM-5	.36	1.23	3.75×10^{10}	1746.	1830.	2150.	2250.
[2]PL-2	.36	1.192	2.6×10^{9}	468.	1460.	557.	1740.
[3]SOLITHANE 113	.48	1.009	2.92×10^{8}	170.	374.	172.	377.

1 Skull and brain properties from current literature (See Chapter II-Modelling Considerations)

2 PSM-5 and PL-2 properties from Photoelastic, Inc. (Bulletin P-1120-1) and Jolly-Beam density measurements

3 Solithane 113 properties from Thiokol, Inc. (Bulletin UR-12) and Jolly Beam density measurements

4 Co computed based on $Co = \sqrt{K/\rho}$

5 Co experimental based on measured wave speeds in reference plates

of the wave speeds before testing makes the choice of materials very diffi-
cult. In the present testing, acoustic impedance mismatches were higher and
lower than those for the actual anatomic regions.

V - DISCUSSION

One-Dimensional Analysis

The flat plate one-dimensional modelling of the skull is not directly comparable with closed container spherical models. In addition to the unconnected skull regions, the plate impactor strikes the entire skull on one side of the model. The energy density for such an impact is not the same as the case of a small impactor hitting only a portion of the skull. This concept does provide a model of wave propagation emanating from one side of the head and travelling back and forth through the brain. The primary objective of the plate model is to economically (in terms of computer expenses) determine the effect of several parameter variations within the basic energy absorbing multi-layered skull-brain system. Therefore, the results will emphasize the differences in wave propagation response for several types of flat plate head models.

The nature of the mathematical coupling between the brain and inner tables was found to be very important. Previous mathematical models have considered a strong bond at the brain-inner table boundary, which caused the particles on both sides of the boundary to move together without separating. This non-separating connection permits the dissipative and dispersive effects of the diploe to remain influential during the entire period of analysis. A separable situation can be modelled by assuming that the mathematical coupling between these two layers can fail above a given tensile limit. To show this effect quantitatively, an arbitrary separation tensile stress of 1.0×10^{8} dynes/cm^{2} was assumed for both brain-inner table boundaries (near the site of the blow and on the opposite side). Separation occurred first at the opposite side from the blow (1.68 non-dimensional time units) and then near the site of the blow (2.34 units). The separation (gap) between

the brain and inner tables produces a high acoustic impedance mismatch at the brain boundary; therefore, the stress waves are totally reflected back into the brain and not transmitted to the table region.

Figure 12 shows the total energy (internal energy plus kinetic energy) in the brain as a function of time for the case when the inner table separated from the brain at a tensile stress of 1.0×10^8 dynes/cm^2. Displayed in Figure 13 is the total energy curve for the case when mathematical separation is not allowed (effectively an infinite tensile stress for separation). In both Figure 12 and Figure 13, the following material properties for the skull layers are indicated: elastic tables and elastic diplöe; elastic tables and elastic-plastic diplöe; and elastic tables and crushable hydrodynamic foam diplöe. The lower total energy levels (also lower internal energy levels), in the case of no separation, is due to the continued attachment the skull to the brain.

The complex C.S.F. and meningeal regions physically comprise what has been described as simply a boundary condition. Destruction of the vascular tissue in this region could cause serious intracranial bleeding. No experimental investigations have been performed have to determine the nature or level of such injury mechanisms. Because the one-dimensional plate model does not have the geometrical dispersion effects of a spherical model (small impactor striking a large head), the stress levels are necessarily higher than in a real head impact. Therefore, in the spherical models the tensile stress level at the brain-inner table boundary will be less than in the plate models. Until a more definitive separation stress can be ascertained, the firm bonding condition will be utilized in all model analyses. The potential importance of properly defining this boundary or correctly
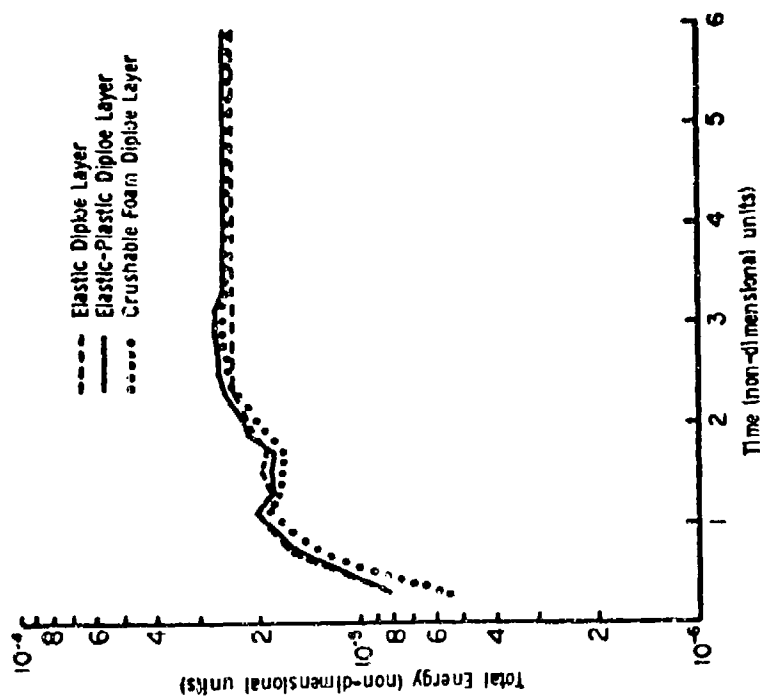
Figure 13. Total energy in brain layer of one-dimensional analysis with no skull-brain separation.

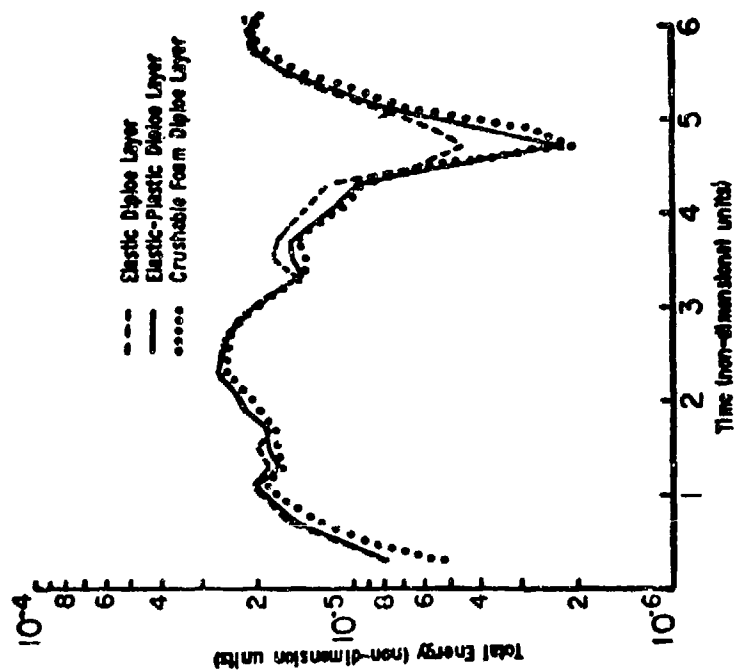

Figure 12. Total energy in brain layer of one-dimensional analysis with skull-brain separation.

incorporating these anatomic layers requires future experimental and analytic investigation.

The internal energy within the brain quantifies the stress-strain tissue deformation in the brain. In comparing the effects of various material descriptions for the layered models, the internal energy versus time curves will be displayed. The curves in Figures 14 to 18 are assumed to have no separation. Because it was desired to accurately plot data points over a large range of values, a semi-logarithmic display form was utilized. The non-dimensional units, as described previously, are used on all curves.

Figure 14 shows the internal energy curve for the average material properties as listed in Table I. The energy contained within the brain is in the following decreasing order: elastic diplöe, elastic-plastic diplöe, and crushable foam diplöe. The percentage difference between the elastic and elastic-plastic models varies from 2% to 50%, while there is a 10% to 65% difference between the elastic and crushable models. The crushable foam model would absorb more energy if the final crush-up pressure were not set higher than the actual value. The periodic peaking of the internal energy represents the movement of the main wave front as it carries a large portion of the energy from the brain compartment to the skull and back again.

The thickness of the diplöe in proportion to the table thickness differs between locations on the skull and between various individuals. A special situation with the diplöe thickness increased by 2-1/2 times the original value (0.125 non-dimensional units from 0.05 units) was analytically examined to determine the effects of a large change in the diplöe thickness parameter. Figure (15) shows the results for the elastic-plastic and crushable foam enlarged diplöe models. The elastic diplöe model results are included for
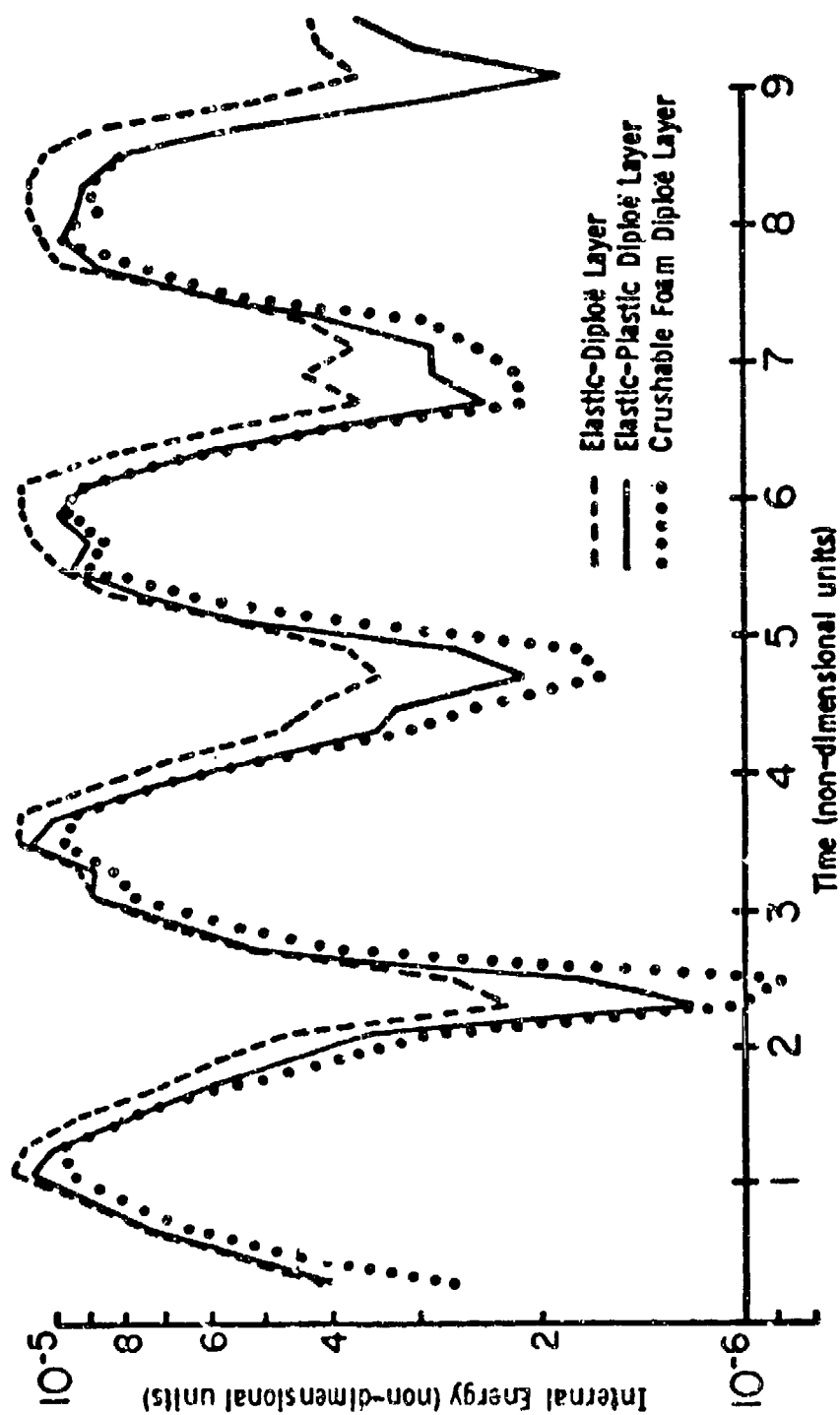
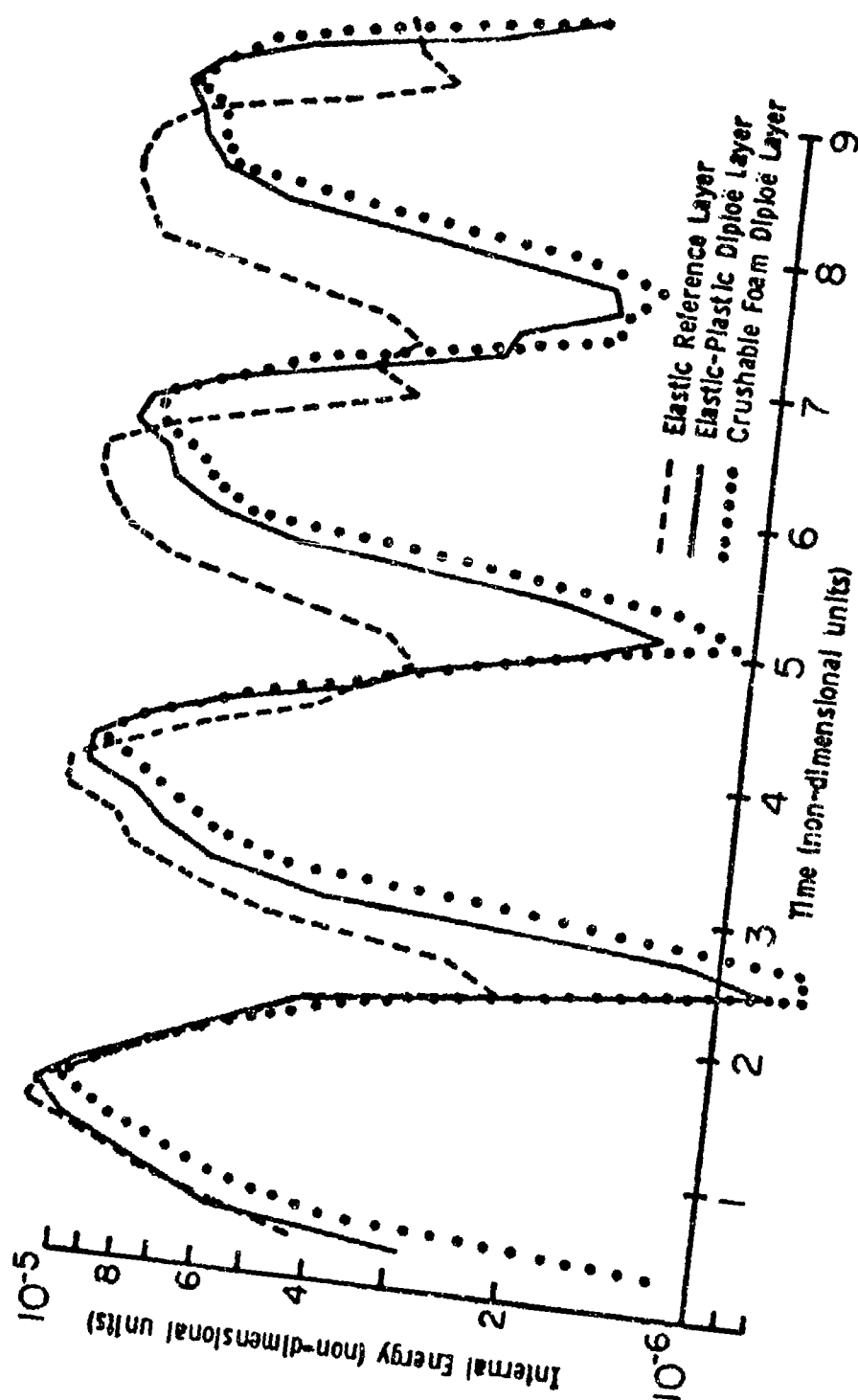Figure 14. Internal energy in brain layer of one-dimensional analysis with average property values.

Figure 15. Internal energy in brain layer of one-dimensional analysis with enlarged diploë layer.

reference to the original problem values. The percentage difference between the elastic and elastic-plastic models is now as high as 65%, while the percentage difference between the elastic and crushable foam models is as high as 70%. The basic implication from this increased dissipative layer thickness is that (as one would expect) an enlarged energy absorbing layer gives better protection to the interior layers.

The difference between the bulk sound speed in the tables and diplöe is very slight (1.6 to 1.467) in the basic formulation. The acoustic impedance (density multiplied by sound speed) of a material layer is important in wave propagation analysis. If there is a larger acoustic impedance mismatch between two layers, then a greater portion of the wave energy is reflected at the boundary instead of transmitted. In order to investigate a variation of this impedance difference, the analytic computer code was programmed for a sound speed ratio of 1.6 to 1.0. Figure (16) displays the internal energy results for an elastic-plastic diplöe with a large acoustic impedance mismatch. Again, as expected, the energy transmitted to the brain is somewhat reduced. The parameter study is not detailed enough at this point to make a definitive judgment as to whether the diplöe thickness parameter or diplöe bulk sound speed parameter is more effective in reducing the energy transmitted to the brain. Figure (17) displays the results of both enlarging and decreasing the wave speed in the diplöe region. With both modifications included, there is now a percentage difference as large as 72% between the elastic and elastic-plastic diplöe models. Due to the slower wave speed and larger distance to traverse, there is now an appreciable phase difference between the two curves. The dashed line indicates that peak energies are decreasing with time. A straight line on this semi-logarithmic scale suggests that a logarithmic energy decay occurs.
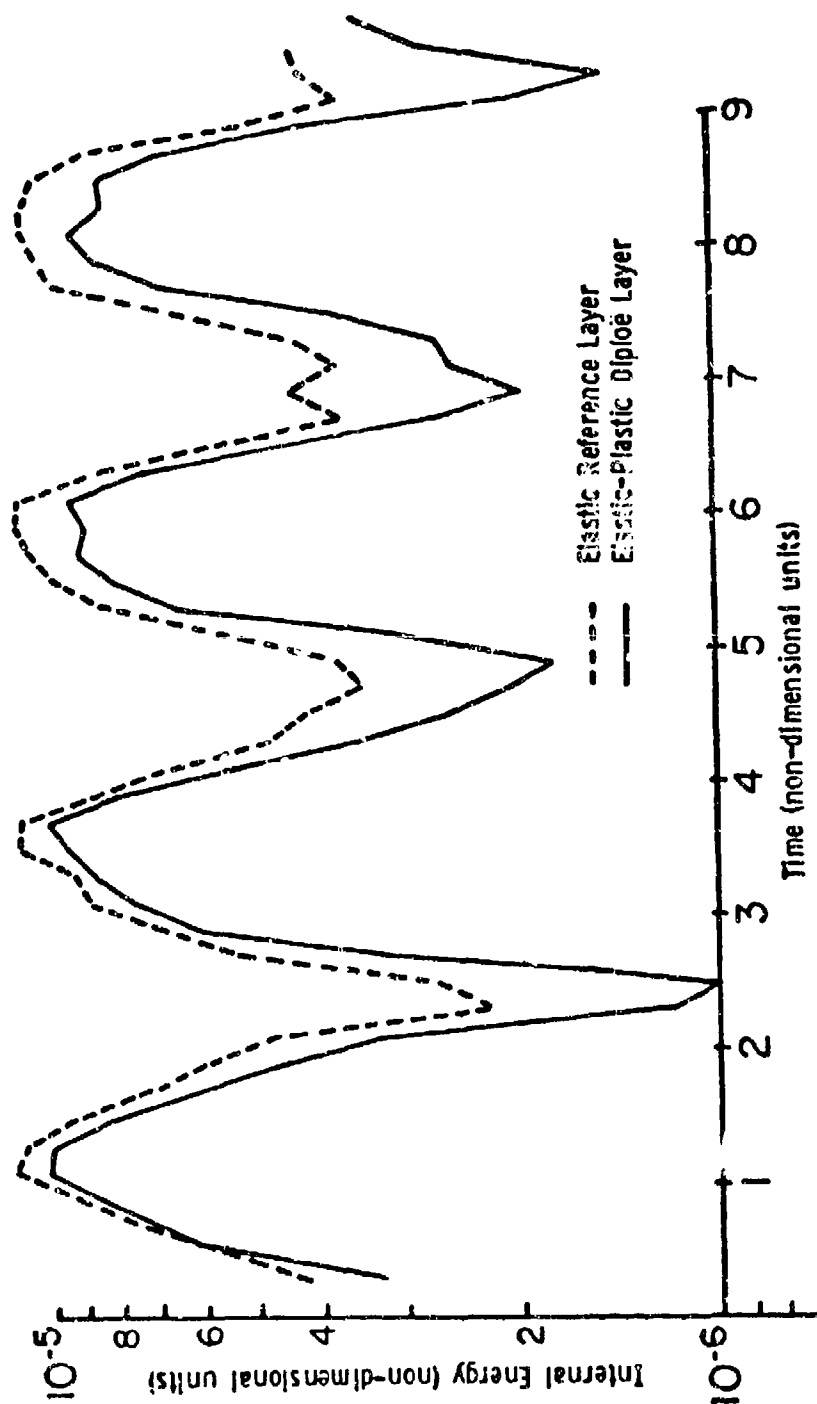
Figure 16. Internal energy in brain layer of one-dimensional analysis with large acoustic impedance mismatch for elastic-plastic diploe model.
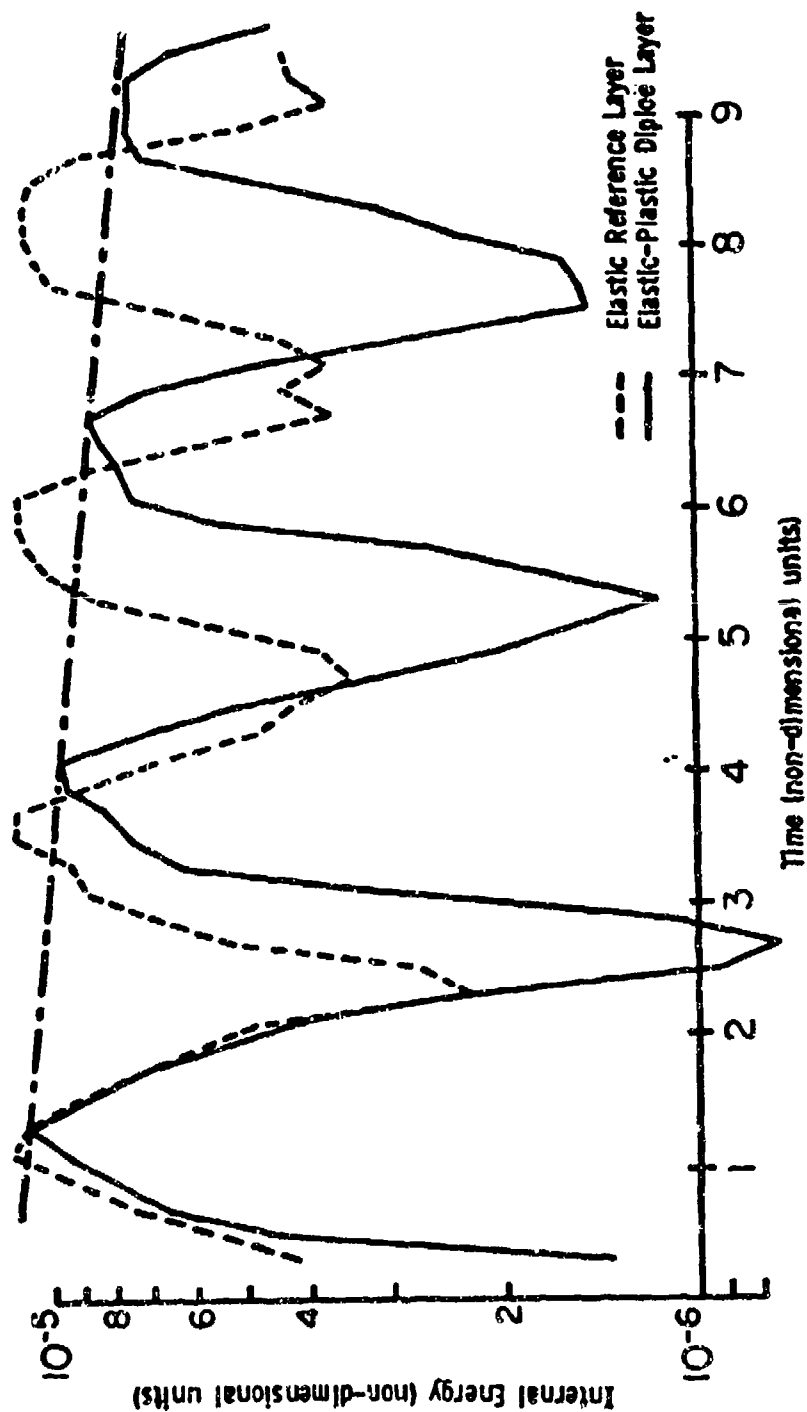
Figure 17. Internal energy in brain layer of one-dimensional analysis with enlarged diploë and large acoustic impedance mismatched for elastic-plastic model.

The crushable foam diplöe model yielded results which were less pre-dictable than those of the previous examples. When the acoustic impedance decreased, the energy in the brain increased (see Figure (18)). As the extra energy was reflected back into the crushable diplöe region, the pressure in the diplöe was increased by 25%. While the material is crush-ing to its solid condition, the sound speed is changing from the value for foam to the value for solid material. An increased pressure causes the foam to rapidly crush towards the solid sound speed condition. The over-all significance is that the mathematical non-linearities of the hydro-dynamic foam model suggest that a sound speed parameter optimization exists for foam energy-absorbing layers. For the elastic-plastic diplöe model, the total plastic work done in the diplöe can be computed. The value of plastic work as a function of time is plotted in Figure (19). The signific-ance of plastic work is that it represents stored energy which cannot be transmitted into the brain as injurious energy.

No previous one-dimensional models are formulated in an analogous manner to the present analysis. The lumped-parameter models cannot predict local stress levels and the rigid container model of Hayashi (1969) is accurate for soft impacts before the container rebounds. The "exact" ex-pansion solution of Liu (1970) predicts wave propagation effects, but the rigid container aspect results in zero pressure at the center. The present wave propagation emanating from impact on one side of the head and traveling back and forth through the brain seems to be an realistic model for the actual head impact situation.

In searching for the highest level of tensile stress near the blow and opposite to the blow, there is a chance of missing the true peak value with
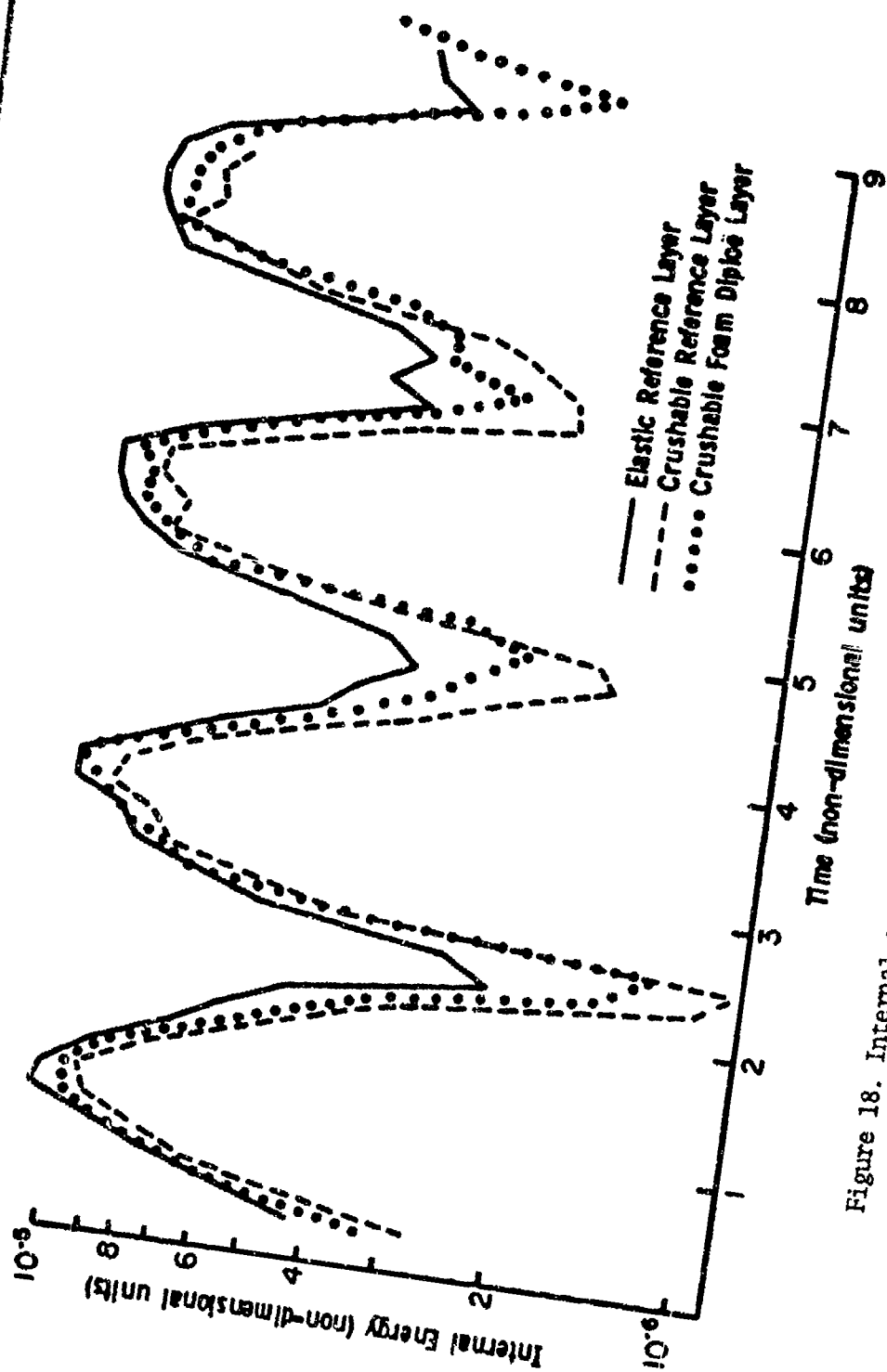
67

Figure 18. Internal energy in brain layer of one-dimensional analysis with large acoustic impedance mismatch for the crushable foam diploë model.
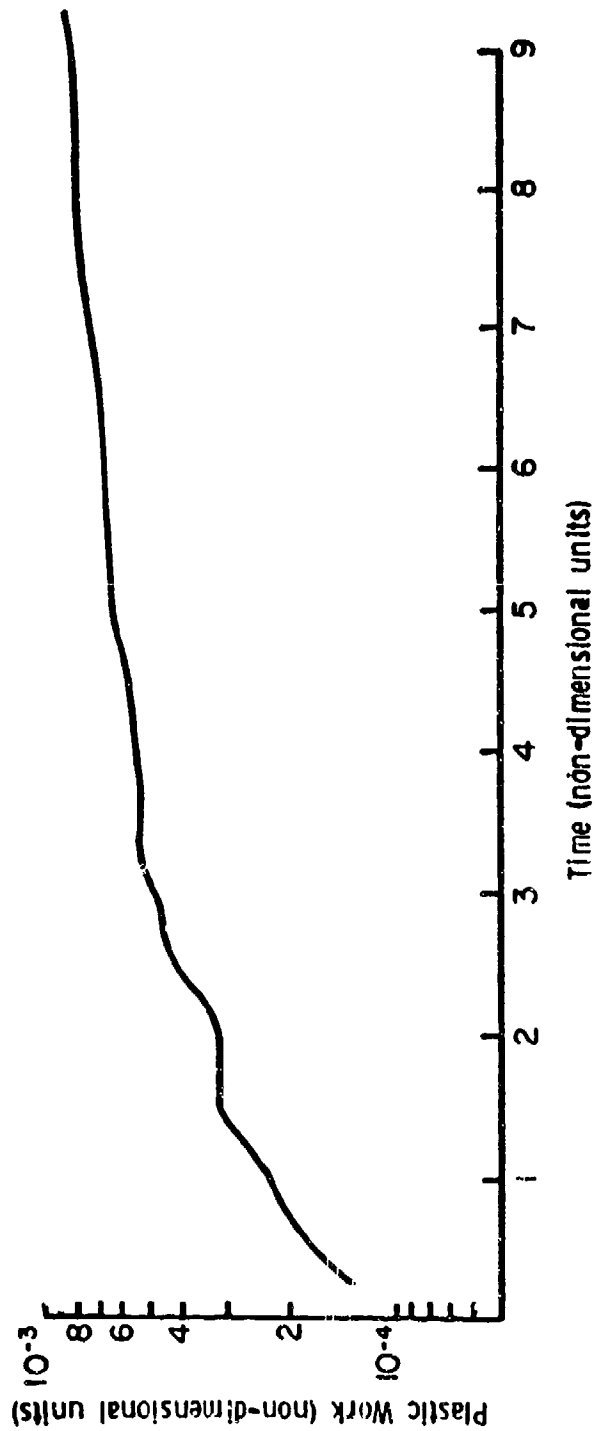
Figure 19. Plastic work in diploë layer for elastic-plastic model of one-dimensional analysis.

the reduced number of outputs. However, the indication of trends is more significant, at present, than the extra information gained from costly excess computer operation. The output was scanned to locate the tensile stress peaks near the site of the blow and near the opposite side. In addition to determining the value and time of occurrence for the first tensile stress peaks, similar information was obtained for the second peaks. Table 4 displays the first and second peak values and their respective times for several diplöe models. All values listed are in non-dimensional units (one unit is approximately 50μ sec). In a hydrodynamic model, normal stress is equivalent to pressure. Tensile pressure is considered positive in Table 4.

MAGNITUDE AND OCCURRENCE OF PEAK TENSILE STRESSES

SKULL LAYER MODELS	1st peak near blow $\times 10^{-2}$	time	1st peak opposite blow $\times 10^{-2}$	time	2nd peak near blow $\times 10^{-2}$	time	2nd peak opposite blow $\times 10^{-2}$	time
ELASTIC	.738	4.4	.662	3.4	.668	7.8	.432	8.4
ELASTIC-PLASTIC	.566	4.5	.601	3.5	.578	7.7	.373	8.2
CRUSHABLE	.526	3.0	.624	3.6	.626	7.7	.432	8.3
ELASTIC-PLASTIC*	.588	3.1	.594	4.1	.617	8.6	.385	9.5

*With enlarged diplöe and large impedance mismatch.

TABLE 4

PEAK TENSILE STRESSES NEAR THE SITE OF THE BLOW AND OPPOSITE THE SITE OF THE BLOW

(Stress and time are given in non-dimensional units.)

The presence of relatively high tensile stresses near the site of the blow, near the opposite side from the blow, and even in the central regions suggest potential sites of coup, contrecoup, and intermediate coup. The important fact to note is that these tensile stresses can appear in the absence of a closed container model. This fact agrees with the concept of Goldsmith (1966) that rarefaction waves reflecting from the interior skull surface cause high tensile stress levels.

The information shown in Table 4 was obtained from the second spatial zone and next to last zone for the brain layer of the one-dimensional model. The sharp rise of a stress wave could cause an absolute peak value to be unobserved by the data output system. However, the peak tensile stresses in the brain seem to be reduced by the energy absorbing diploe layer models. There is also a general trend for reduced pressure at other brain locations. The stress levels near the site of the blow appear to remain relatively high at the second peak, while the opposite side of the brain experiences a reduced stress level at the second peak.

An important concept in the potential mechanisms for head injury is the duration of the injurious force. Liu, et al (1971) define a Cumulative Damage Criterion which is based on the pressure-time area beyond a cut-off tensile stress level. Therefore, a possible design criterion for protective head devices is not only reduction of energy levels and peak tensile stress, but also control of the duration of the peak stresses. The present computer output is not adequate to accurately analyze the peak duration times. A scanning of the data yields the approximate durations listed in Table 5. It is to be noted that a peak cut-off level of 2.0×10^{-3} non-dimensional units of stress was used to determine the values for the duration times. The

practical result of using the above cut-off level was that the entire ten-
sile stress wave was observed. Table 5 indicates only duration and not
tensile stress level; therefore, the results are not directly analagous to
the Cumulative Damage Criteria. The site of potential contre-coup injury
is exposed to tensile stress for shorter periods than the potential coup
injury location. The slightly longer durations with the crushable and
elastic-plastic models indicate the general smoothing and spreading of the
wave which is the result of including energy absorbing mechanisms.

TABLE 5 - Peak Tensile Stress Duration

DIMENSIONLESS TIME DURATION

SKULL LAYER MODELS	1st peak near blow	1st peak opposite blow	2nd peak near blow	2nd peak opposite blow
elastic	2.3	.7	1.4	1.1
elastic-plastic	2.0	.8	1.6	.8
crushable	2.2	.9	1.7	.8
elastic-plastic*	2.5	1.0	2.0	1.3

*With enlarged diploe and large impedance mismatch.

The results of the rate dependent brain model, for all diplöe models, are shown in Figure 20. The shape of the curves is similar to the shape of the rate independent brain model curves. The peak internal energy values for all diplöe models are approximately equivalent for the two brain models. The lower portion of the internal energy curves for the energy absorbing diplöe models, with the viscous brain layer, was slightly higher than that of the inviscid brain model. There are no conclusive explanations as yet for this increased energy. A potentially larger acoustic impedance mismatch could lead to extra energy storage in the brain region. Because the viscous model is first order accurate (compared to second order accuracy for all other constitutive models), an increased number of time cycles is required to attain meaningful results. Despite the attempt to achieve a uniform degree of accuracy, the rate-dependent model yie.ds energy balance errors as large as 10%. This error could have produced the higher energy found in the viscous model. In general, the viscous brain model does not seem to differ greatly from the inviscid model, but further analysis is required to more accurately describe the rate-dependent brain effects.

Two Dimensional Analysis

Four spherical model analyses were solved as follows: (1) elastic single layered skull and hydrodynamic brain; (2) elastic single layered skull and elastic (shear) brain; (3) layered skull with elastic-plastic diplöe and hydrodynamic brain, and (4) layered skull with crushable diplöe and hydrodynamic brain. While some skull data is presented, the primary effort is concentrated on determining potentially dangerous mechanical stress conditions that exist in the brain. The first and fourth model
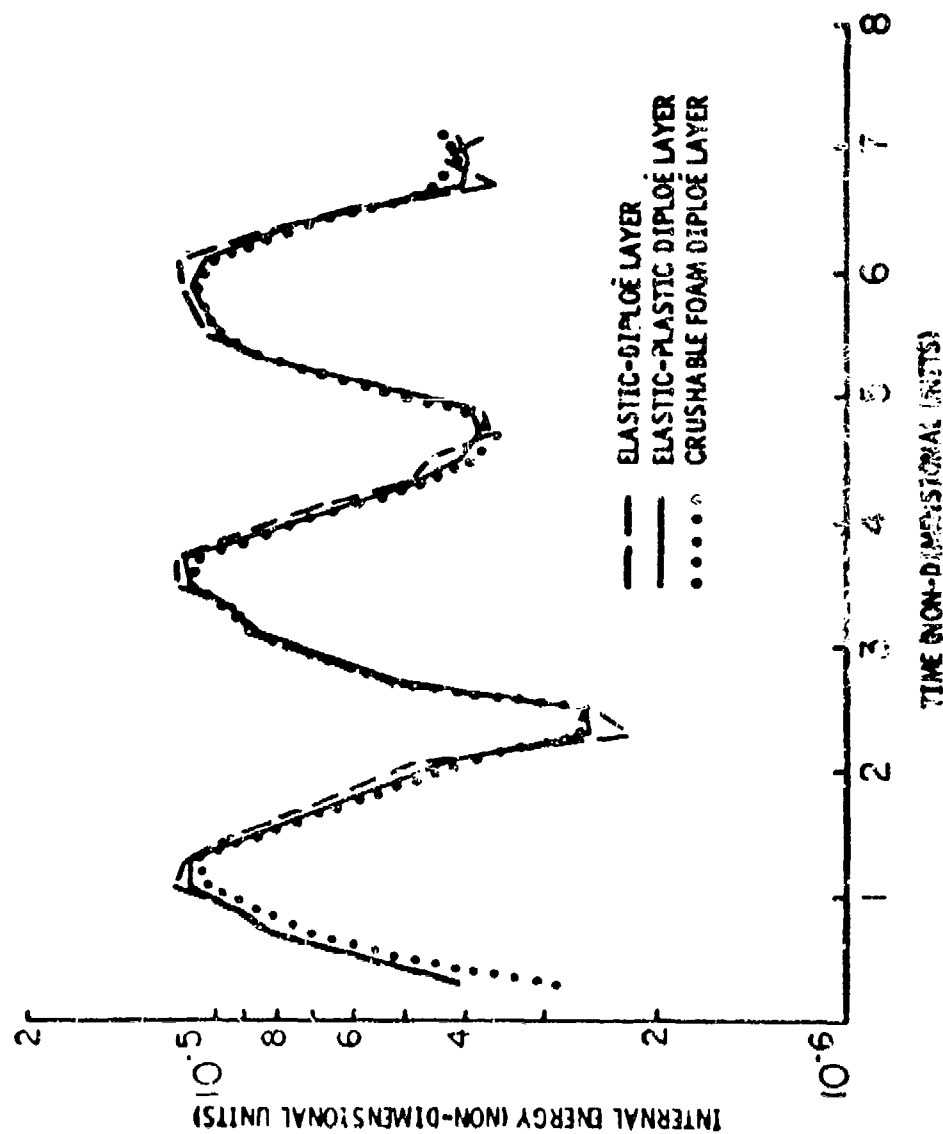
Figure 20. Internal energy in brain layer of one-dimensional analysis with viscoplastic brain model.

analyses were solved for 8.0 units of dimensionless time, while the second and third are only solved for 3.5 units.

The large volume of data generated by the "TOODY-IV" computer code can only be interpreted by considering selected graphic displays. Three forms of computer drawn plots are utilized. Figure 21 depicts a polar coordinate system for identifying the locations at which pressure values are plotted. The 0° line actually represents the average stress values in the zone adjacent to the symmetry line. The 180° line is defined in the same way. By considering a fixed angle, the pressure-time curve for a given radius may be drawn. It should be noted that in all plots tensile pressure is considered positive. To present an overall perspective of the pressure at several radii along a given angle, a hidden line plot is used which shows only the maximum tensile pressure that is visible when six radii are drawn with an effective three-dimensional depth into the paper. A final type of graph displays pressure over the entire brain region at a given time. Each hemisphere (the symmetric image is equivalent) contains 144 values of relative pressure from +9 to -9. Table 6 describes the conversion from dimensionless pressure to the relative scale used in the pressure profiles.

The single layered elastic skull and hydrodynamic brain model is the basic model that serves as a reference for other models in this paper and as a comparison with previous analyses. Even this simple model is very complex in terms of physically explaining the wave propagation results. All pressure and stress values are the composite result of several mechanical phenomena.

As the primary wave passes through the skull and enters the brain, a stress wave travels around the skull becoming a new point source for generating waves inward towards the brain. Because the impactor only strikes a small
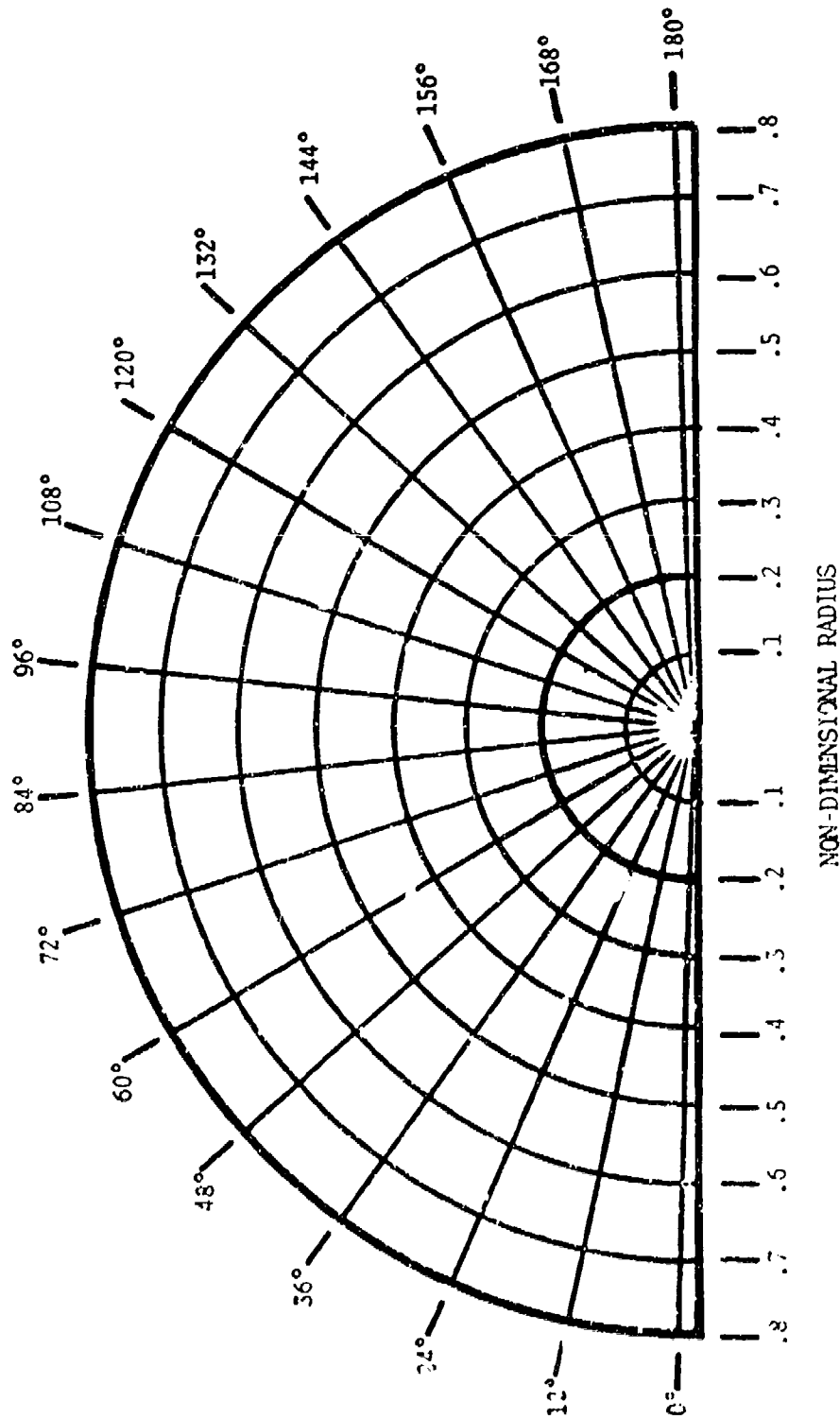
NON-DIMENSIONAL RADIUS

Figure 21. Polar coordinate system for two-dimensional pressure plots.

TABLE 6 - Relative Values for Stress Profiles

DIMENSIONLESS COMPRESSIVE STRESS LESS THAN	-1.10^{-7}	-5.10^{-7}	-1.10^{-6}	-5.10^{-6}	-1.10^{-5}	-5.10^{-5}	-1.10^{-4}	-5.10^{-4}	-1.10^{-3}	-5.10^{-3}
RELATIVE SCALE	0	-1	-2	-3	-4	-5	-6	-7	-8	-9

DIMENSIONLESS TENSILE STRESS GREATER THAN	$+1.10^{-7}$	$+5.10^{-7}$	$+1.10^{-6}$	$+5.10^{-6}$	$+1.10^{-5}$	$+5.10^{-5}$	$+1.10^{-4}$	$+5.10^{-4}$	$+1.10^{-3}$	$+5.10^{-3}$
RELATIVE SCALE	0	1	2	3	4	5	6	7	8	9

portion of the skull, the regions adjacent to the indentation bulge outward giving rise to tensile relief waves. Subsequent to the initial in-bending of the shell near the symmetry axis, the shell snaps back to produce rarefaction waves from outbending. When any of these waves travelling in one medium impinges on a boundary region of another medium, then all the stress-optical laws of reflection and refraction are obeyed. The most significant of these wave phenomena is the change from compression to rarefaction that occurs when a wave moving in a medium of high acoustic impedance reflects from the surface of a lower acoustic impedance material. Also the skull tends to accelerate its mass center before the brain starts to move; therefore, on the side opposite from the impactor there is an additional source of tensile force. Because the primary objective of this analysis is to evaluate damage potential in the brain, there is only a secondary effort to ascertain the source of the resultant wave propagation.

Impact to the elastic skull and hydrodynamic brain model produced regions of high tensile pressure in the brain near the blow, on the opposite side from the blow, and at several locations in between. Using the approach that brain tissue fails by excessive tensile pressure (see Benedict (1970) and Engin (1969)), these regions of rarefaction could represent the mechanism for coup, contre-coup, and intermediate coup, respectively. Two of the three-dimensional perspective graphs show the pressure results along the symmetry axis. Figures 22 and 23 display the pressure-time curves for six radii along the 0° and 180° lines in the brain. For times up to 3.5 dimensionless units, the largest tensile pressure appears at the outer radius along the 180° line. Lesser rarefaction peaks occur at several points throughout the brain. At angles further away from the symmetry line, the pressure is
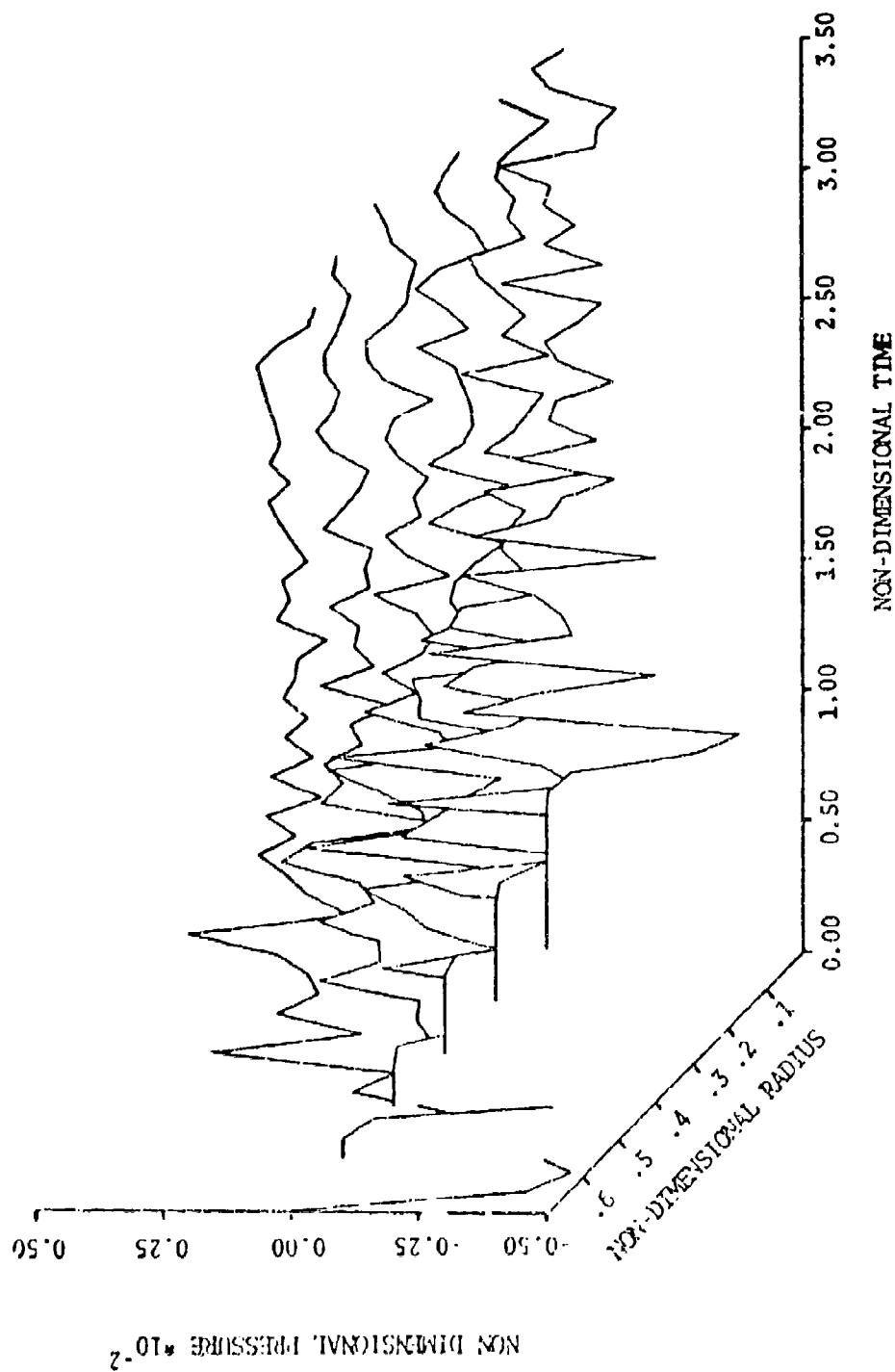
Figure 22. Perspective plot of pressure along 0° line for elastic skull two-dimensional model.
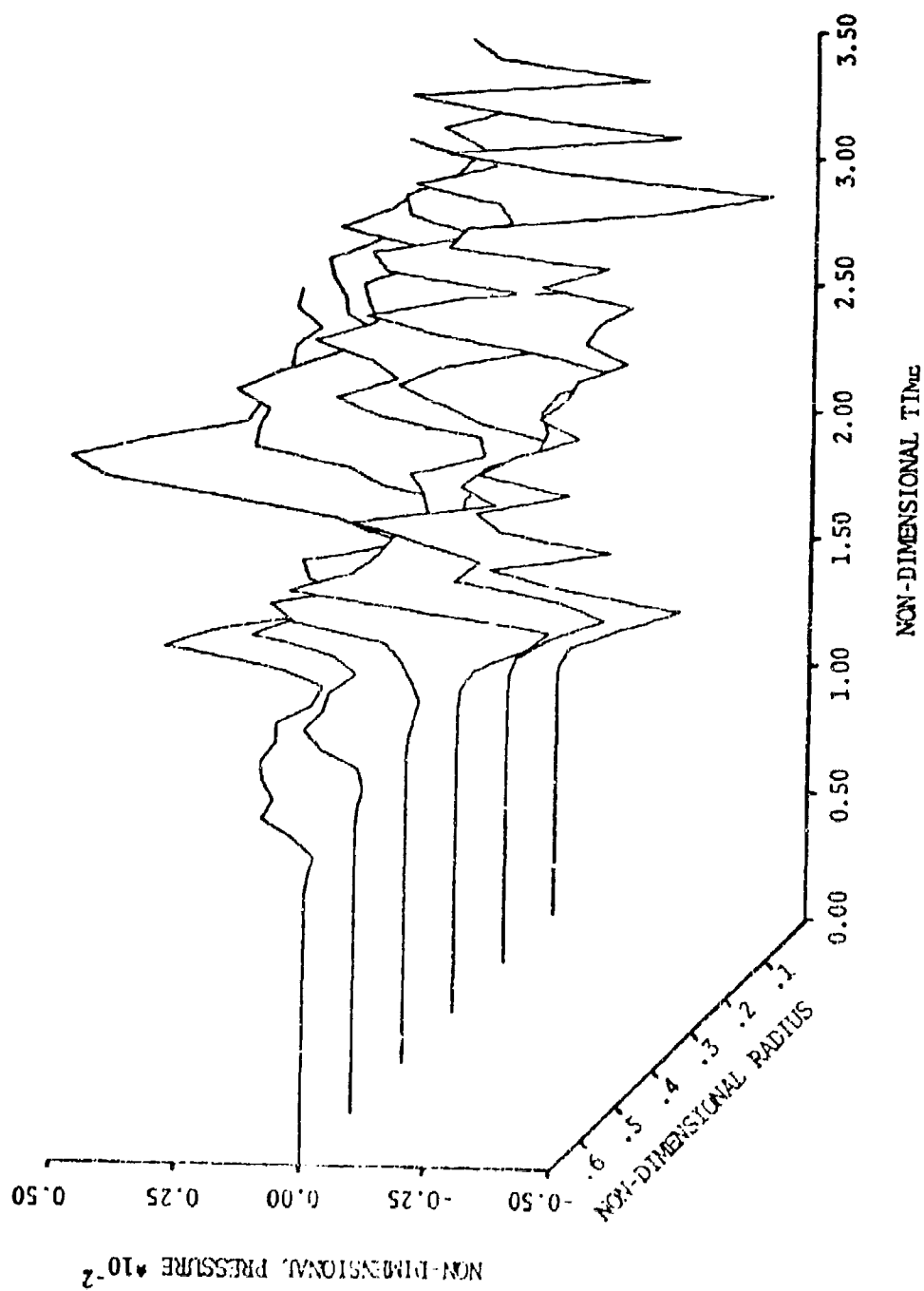
Figure 23. Perspective plot of pressure along 180° line for elastic skull two-dimensional model.

generally weaker. Figure 24 shows the reduced pressure levels that exist along the 96° line.

The exact values of pressure are readily observed in the standard pressure curve given in Figure 25. Because physiological head injury cannot be attributed to a definite mechanism, there are several possible pressure injury phenomena that can be observed from Figure 25. Two types of peak tensile pressures appear at the contre-coup site. Sharp spike peaks occur at times of approximately 2.0 and 2.8 units of time, and a broader, but lower level peak occurs at about 4.0 units of time. If peak level (regardless of duration) causes tissue and vessel damage, then the earlier peaks could cause injury. Also the rapid fluctuation between highly positive and negative pressure would tend to enhance a mechanism that depends on instantaneous failure at peak levels. Liu, et al (1971) proposed that the time averaged pressure (analogous to impulse) was the critical injury mechanism. Using the entire area of the tensile pressure pulse at 2.8 and 4.0 dimensionless times, the broader pressure peak (at the latter time) has a greater area. Figure 26 shows the entire pressure field in the brain at a time of 2.8 units. The wedge shaped region (only half is shown in the symmetric hemisphere) of high tensile pressure opposite from the blow and near the axis line looks very similar to the typical pathological finding in head injury victims (e.g. Lindenberg and Freytag (1957)). Wedge shaped regions were also observed with the broader pulse.

The intermediate location (dimensionless radius of .17) is subjected to several large, spike shaped tensile pulses. The peak values are not as high as at the outer radius, and the pressure profile shown in Figure 27 indicates that this tensile pressure concentration is less diffuse than at the outer

81
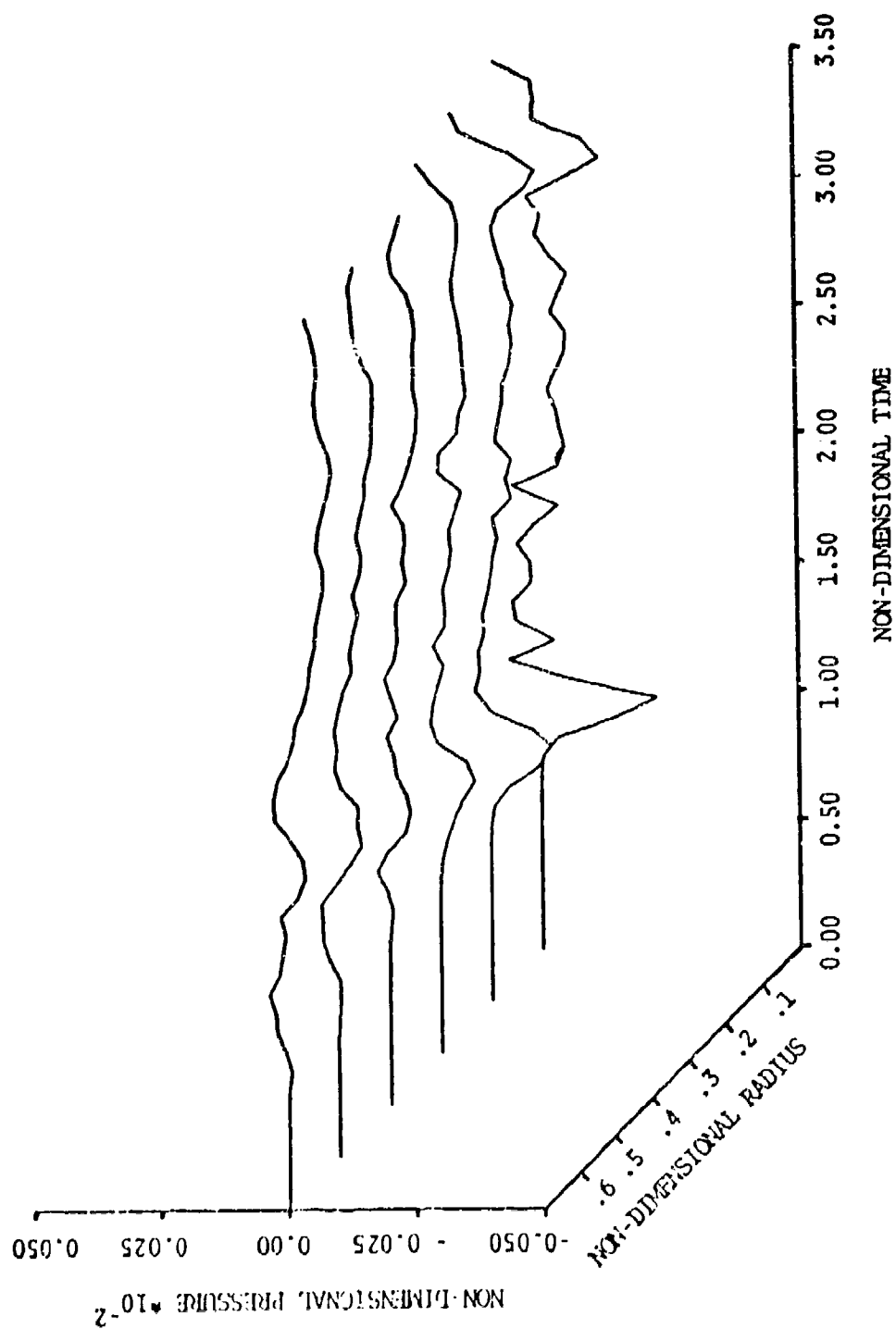
Figure 24. Perspective plot of pressure along 90° line for elastic skull two-dimensional model.

NON-DIMENSIONAL TIME

NON-DIMENSIONAL RADIUS

NON-DIMENSIONAL PRESSURE *10⁻²
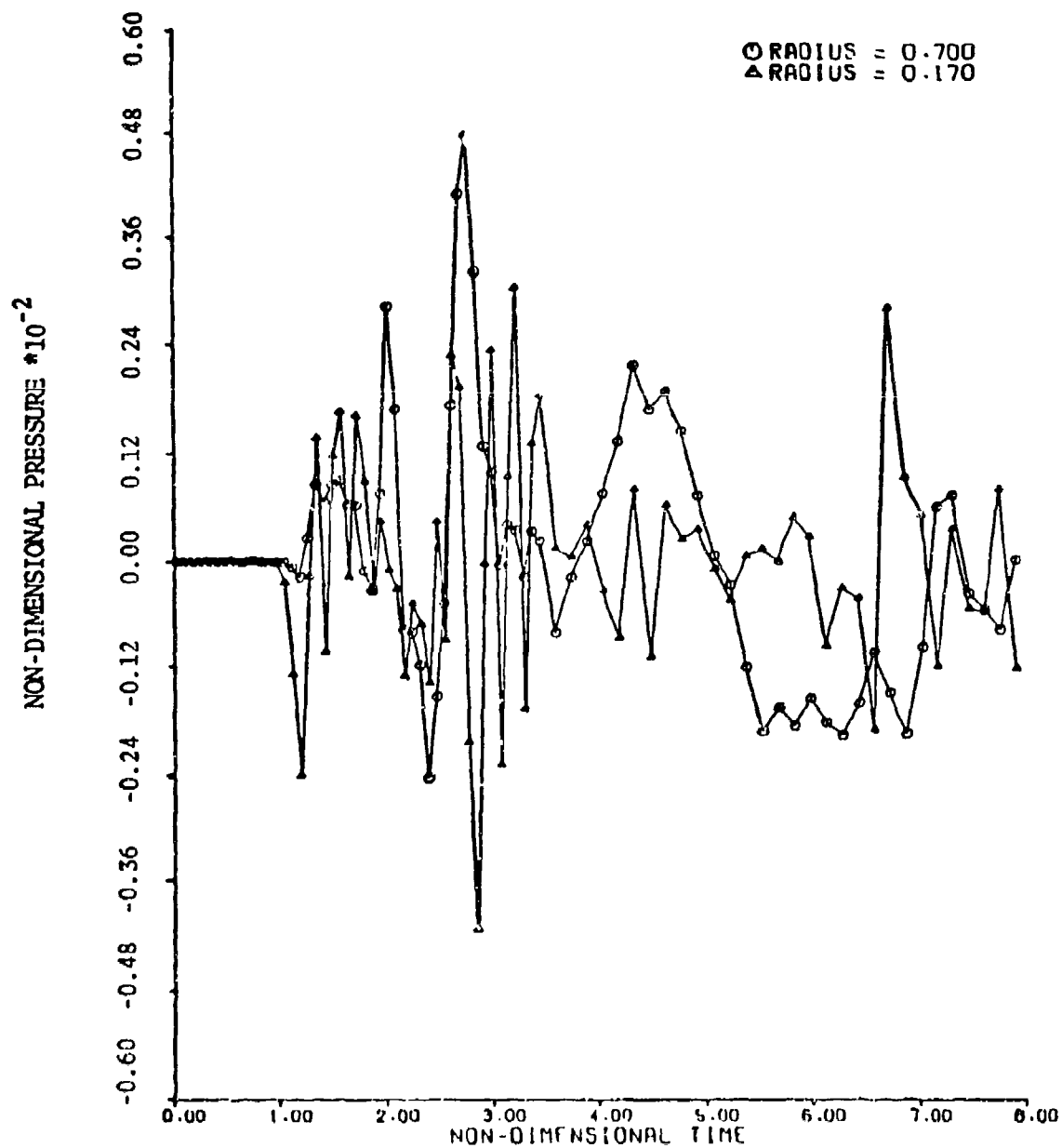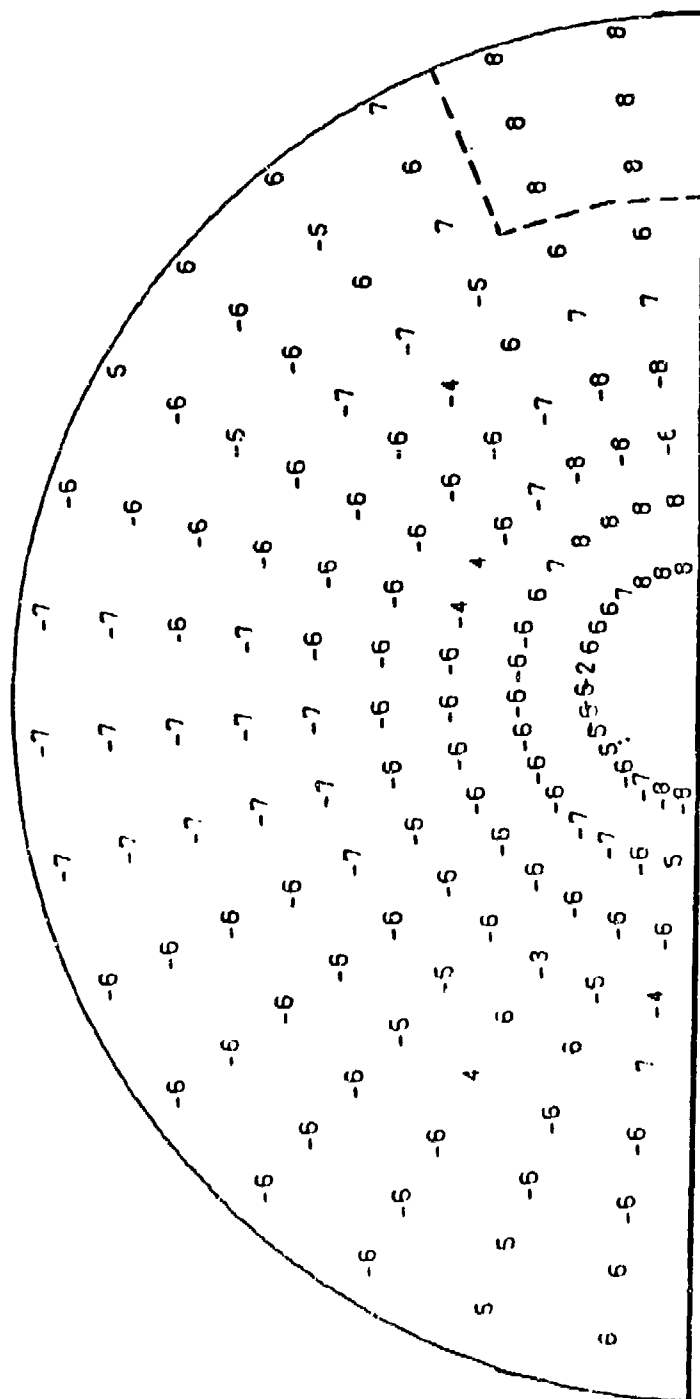
Figure 25. Pressure plot along 180° line for elastic skull two-dimensional model.

Figure 26 - Pressure Profile at Dimensionless Time of 2.8 for Elastic Skull Two-Dimensional Model
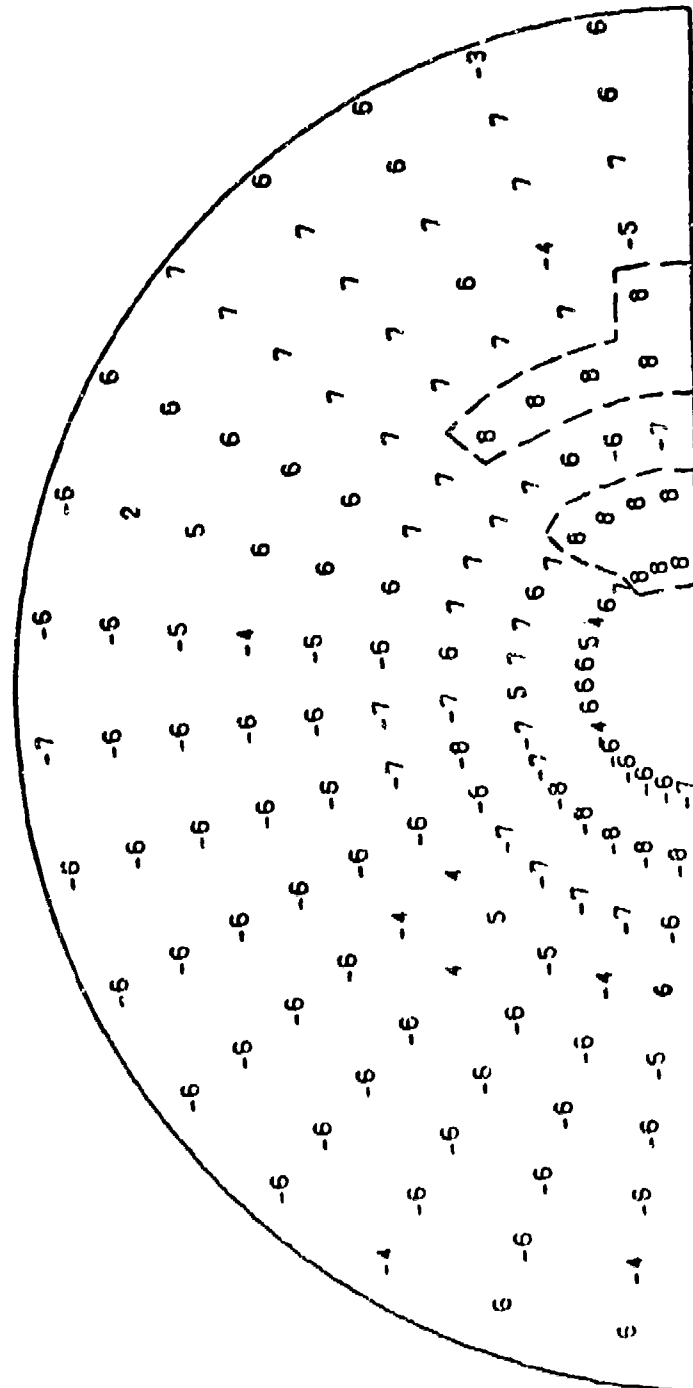
Figure 27 - Pressure Profile at Dimensionless Time of 3.2
for Elastic Skull Two-Dimensional Model

radius. As indicated in Figure 22, the rarefaction peaks near the blow are much weaker and much less diffuse than those opposite the blow.

The elastic skull results described above compare favorably with the analytic solutions of similar problems with impulsive loads as solved by Engin (1969), Liu, et al (1971) and Chan (1972). The time of occurrence and general levels of the peak tensile stresses for contre-coup and intermediate coup are in close agreement with the results of these authors. The rapid transition from compressive to tensile pressures is discussed by Liu, et al (1971). This latter article also discussed the large amplifications of input pressures that result in high peak pressures (1.8×10^8 dynes/cm^2 in the present model) when dissipating mechanisms are not included.

The values of pressure and shear stress in the skull provide some insight into possible regions of skull fracture. Evans (1957) describes skull fracture as being directly related to tensile stresses at and near the impact site. Figure 28 displays the skull pressure (average of the normal stresses) for an outer, middle, and inner radius of the skull along the 0° line. The outer radius shows the high compressive pressure that is the result of decreased curvature from inbending plus strong compression waves from the impactor. The inner radius would be in tension because of increased curvature, but the impact compression waves produce a combined mildly compressive initial pressure. At later times the snap back yields high rarefaction pressures in the outer shell. High tensile pressures in the outer skull appear earlier along the 24° line. Shear levels are also high near the blow and close to the symmetry axis (see Figure 29). The general result of potential sites of skull failure existing in an arc from 0° to approximately 35° are in agreement with the discussions of Engin (1969). Except for some small pressure fluctuations at
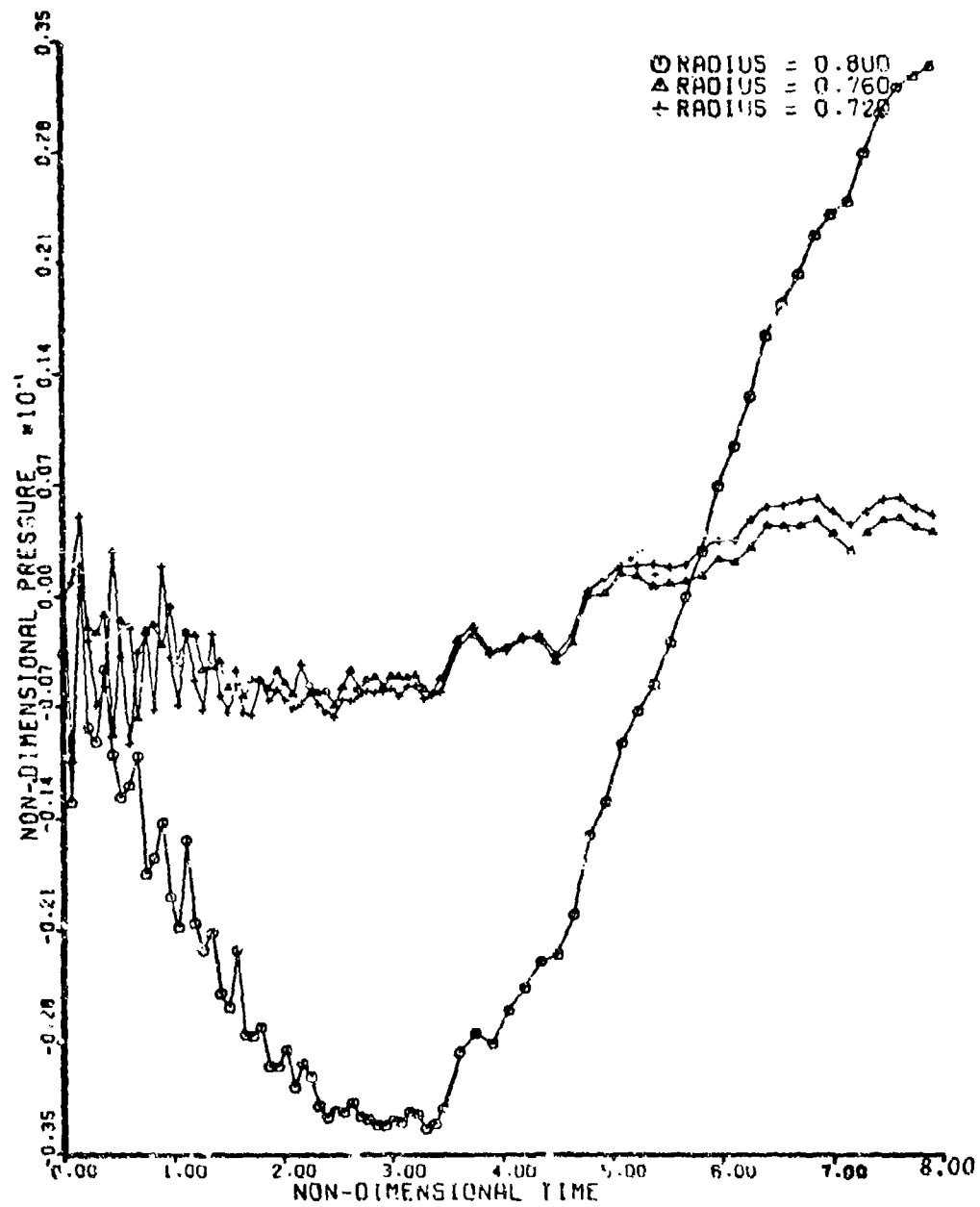
Figure 28 - Skull Pressure Plot along 0° line
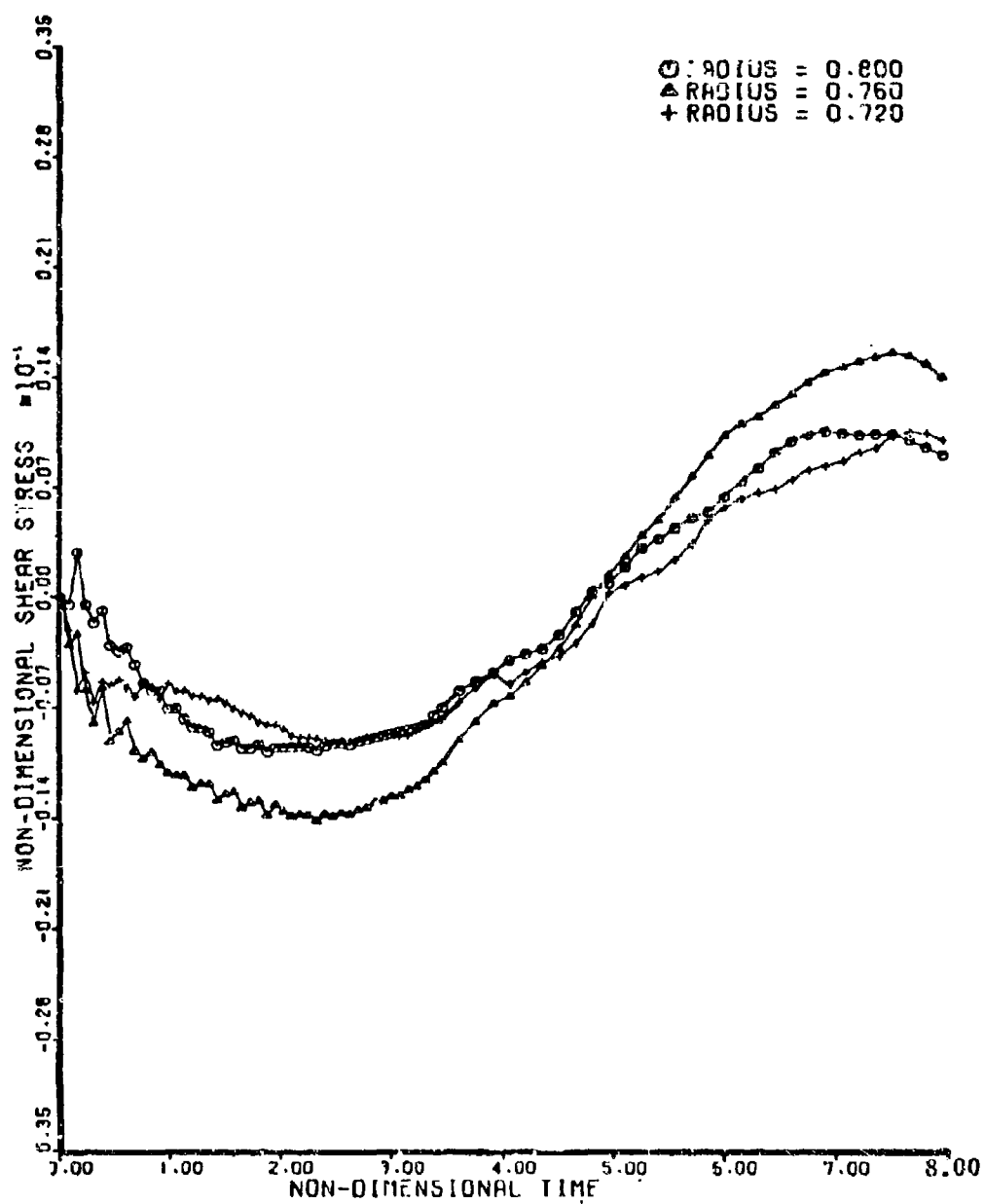Elastic Skull Two-Dimensional Model

Figure 29 - Skull Shear Plot along 24° line
Elastic Skull Two-Dimensional Model

the side opposite the impactor, the skull stresses in the intermediate angles are relatively weak. The regions of high tensile pressure in the skull could possibly be related to the Maximum Strain Index (McElhaney, et al (1971)) in the skull when the problem is extended to longer solutions.

The oscillation between inbending and outbending implies an apparent shell frequency of approximately 2000 Hz. This value is over twice the experimental value of Stalnaker, et al (1970) and Hodgson and Patrick (1968). The explanations for this discrepancy are that the theoretical results are based on dynamic transient effects and that the experimental head mass includes the extra mass of the facial bones.

The elastic skull and elastic brain model results provide an evaluation of the shear stress that may be induced from an axisymmetric translational blow. The assumed dynamic shear modulus of 10^9 dynes/cm^2 is less than one tenth the bulk modulus; therefore, the resultant shear stress values are less than one tenth of the pressure values. For the elastic brain model, the pressure values are computed as the average of the normal stresses. Figure 30 shows that the general form of the pressure-time curves is similar to the results for the hydrodynamic model. The peak pressures are slightly reduced because some of the energy is incorporated into the shear stress.

Shear values for the x-z plane (that are available from the "TOODY-IV" code) are shown in Figure 31. The 168° line is used because these values are higher than those at the 180° line (note that the scale used in one-tenth of the hydrodynamic results scale). There is no definite reason for this angular shift in the peak shear levels. Possibly, the typically slower speed of shear waves has induced a phase lag.
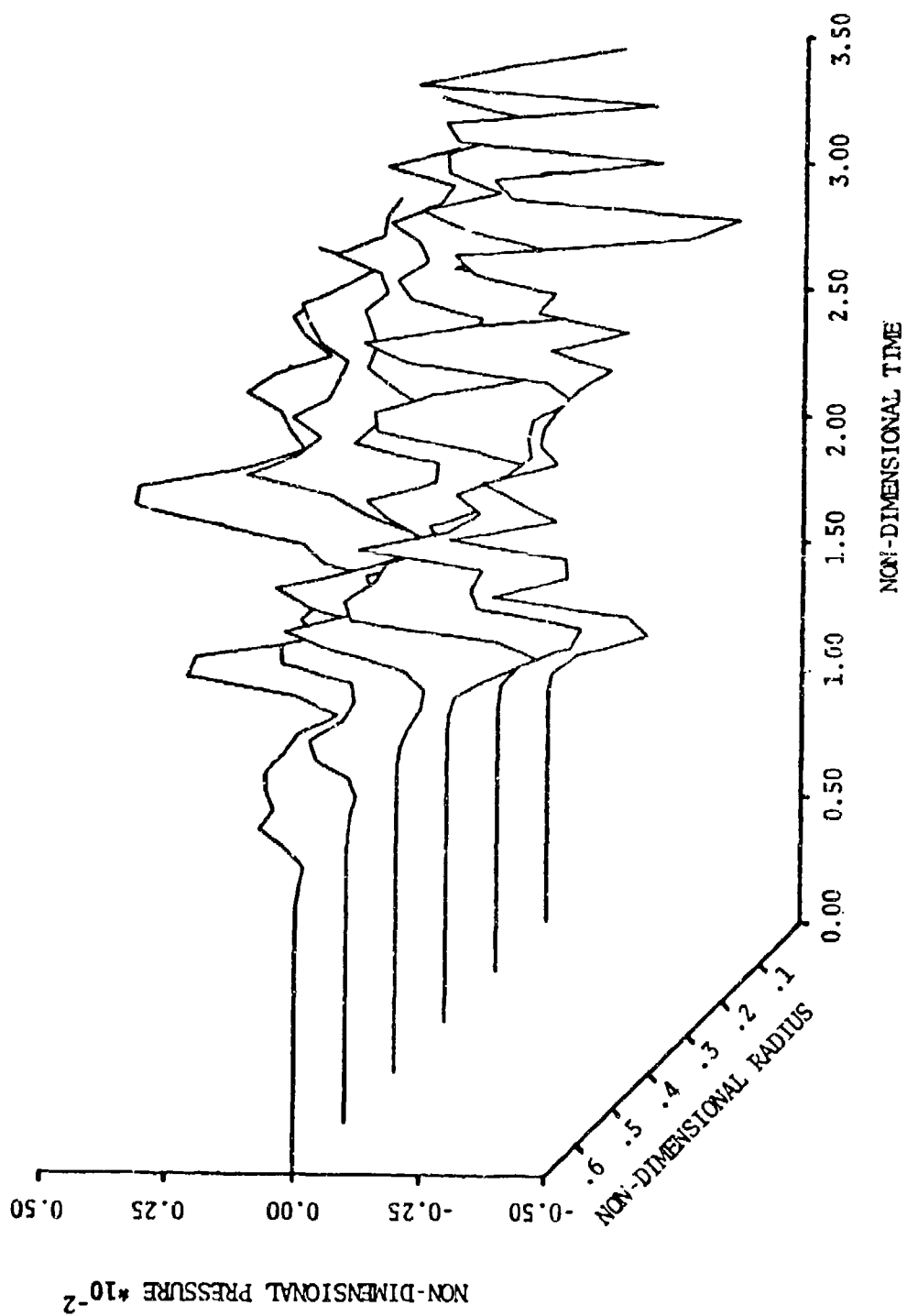
Figure 30. Perspective plot of pressure along 180° line for elastic brain two-dimensional model.
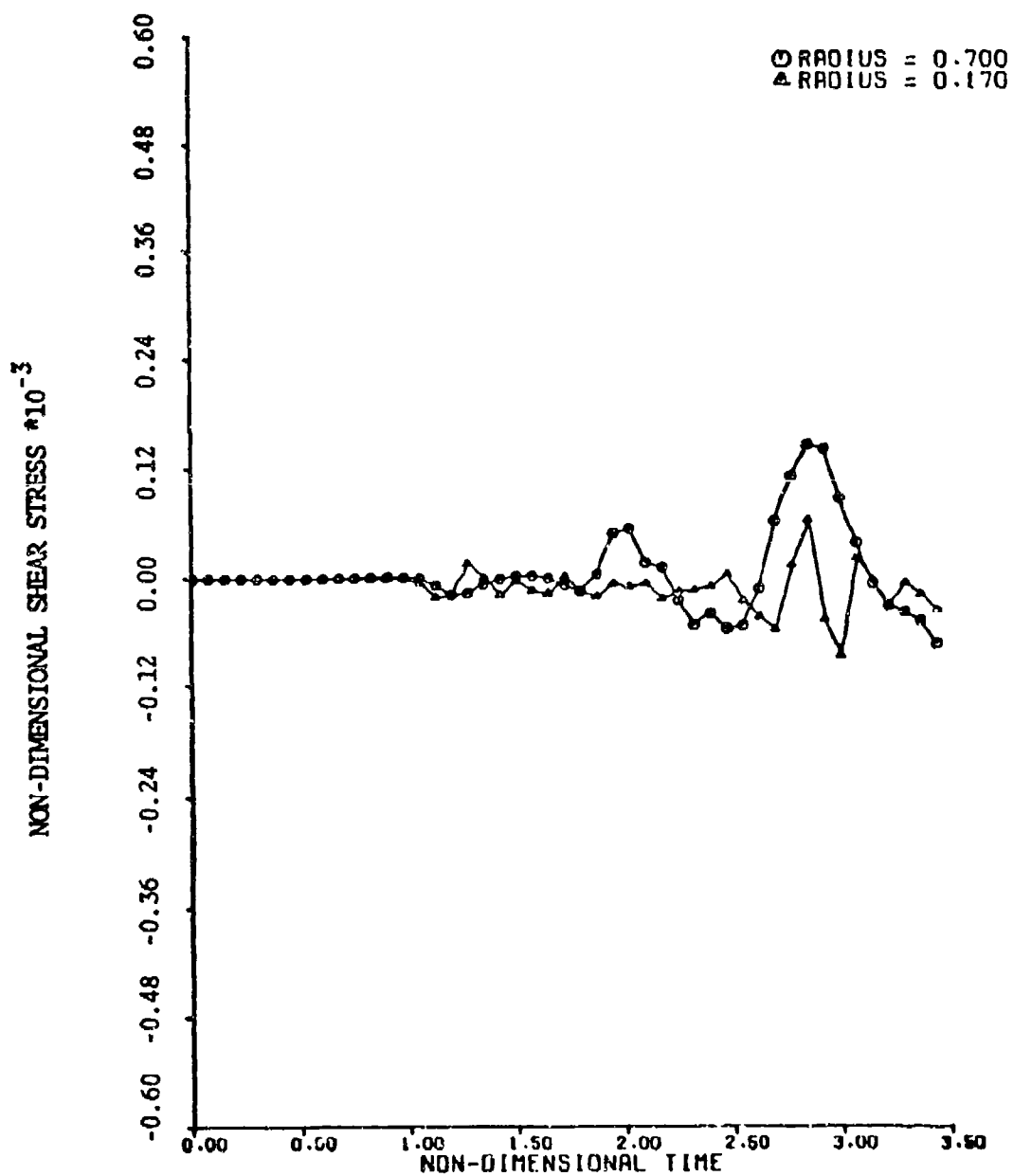
Figure 31. Perspective plot of shear along 168° line for elastic brain two-dimensional model.

The shear and pressure profiles at the dimensionless time of 2.77 are shown in Figures 32 and 33. The high simultaneous values of shear and tensile pressure suggest that the combined effect of these two mechanical forces might produce tissue or vessel damage. Typical shear-normal failure plots for most materials show that adding shear enhances breakage at lower normal stress levels. The use of a high dynamic shear modulus (as in the case of dilute polymer gels) also implies a brittle "glassy" state exists that would result in a fracture mechanism injury. In light of the experimental and pathological evidence of shear produced damage, the shear-tensile pressure injury concept seems to provide a reasonable and unifying explanation of tissue and vessel failure.

The existence of a shear and normal stress at a given point means that there is a principle plane (at that point) on which the normal stress is maximized. Near the outer radius along the 168° line at the 2.77 units of time, the stress conditions are $T^{xx} = .79 \times 10^{-3}$, $T^{zz} = .83 \times 10^{-3}$, and $T^{xz} = .114 \times 10^{-3}$ dimensionless units of stress. A plane exists on which the normal stress if $.93 \times 10^{-3}$. At other locations with lower shear levels, the increase in principle stress is not as large.

The multi-layered skull and hydrodynamic brain models determine the effects of a central skull region of lesser acoustic impedance and of energy absorption in that region. Because it was desired to accentuate the energy absorbing mechanisms (the same goal can be accomplished with a higher energy impact), the value of the yield stress and initial crushing pressure are one-tenth of the static experimental values of Melvin, et al (1970). Skull pressures in all of these analyses were higher than with an elastic skull. Figure 34 shows the skull pressure adjacent to the impactor along the symmetry
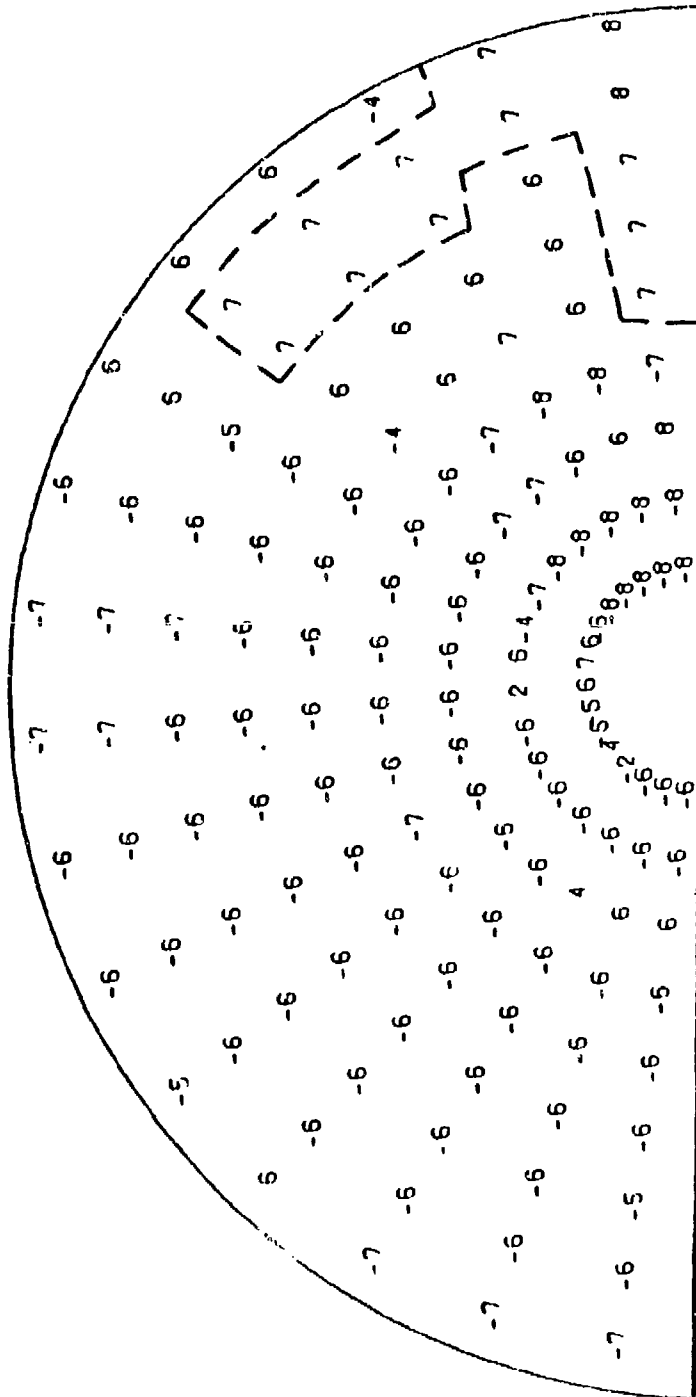
Figure 32 - Pressure Profile at Dimensionless Time of 2.77
Elastic Brain Two-Dimensionless Model

Figure 33 - Shear Profile at Dimensionless Time of 2.77
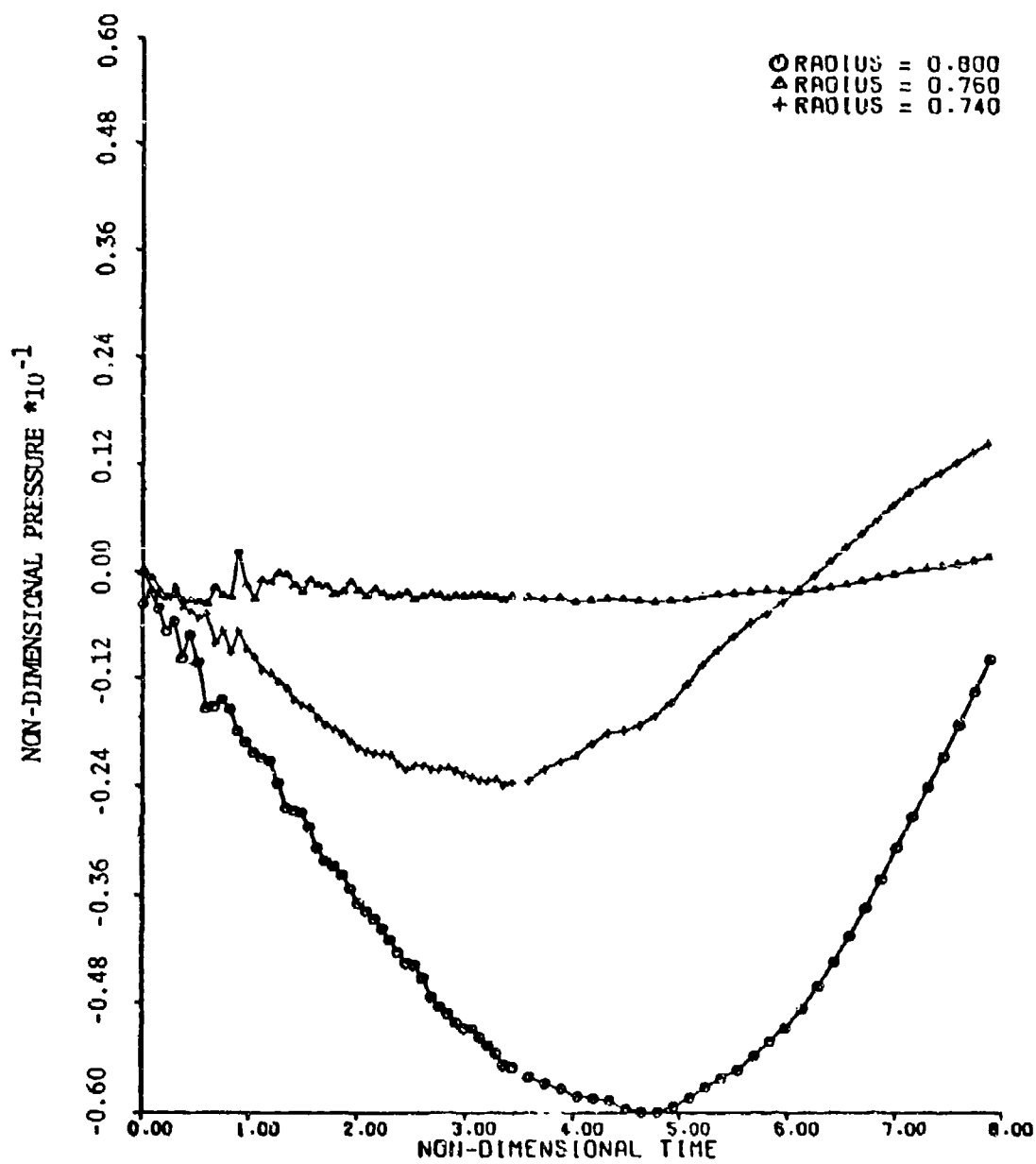for Elastic Brain Two-Dimensionless Model
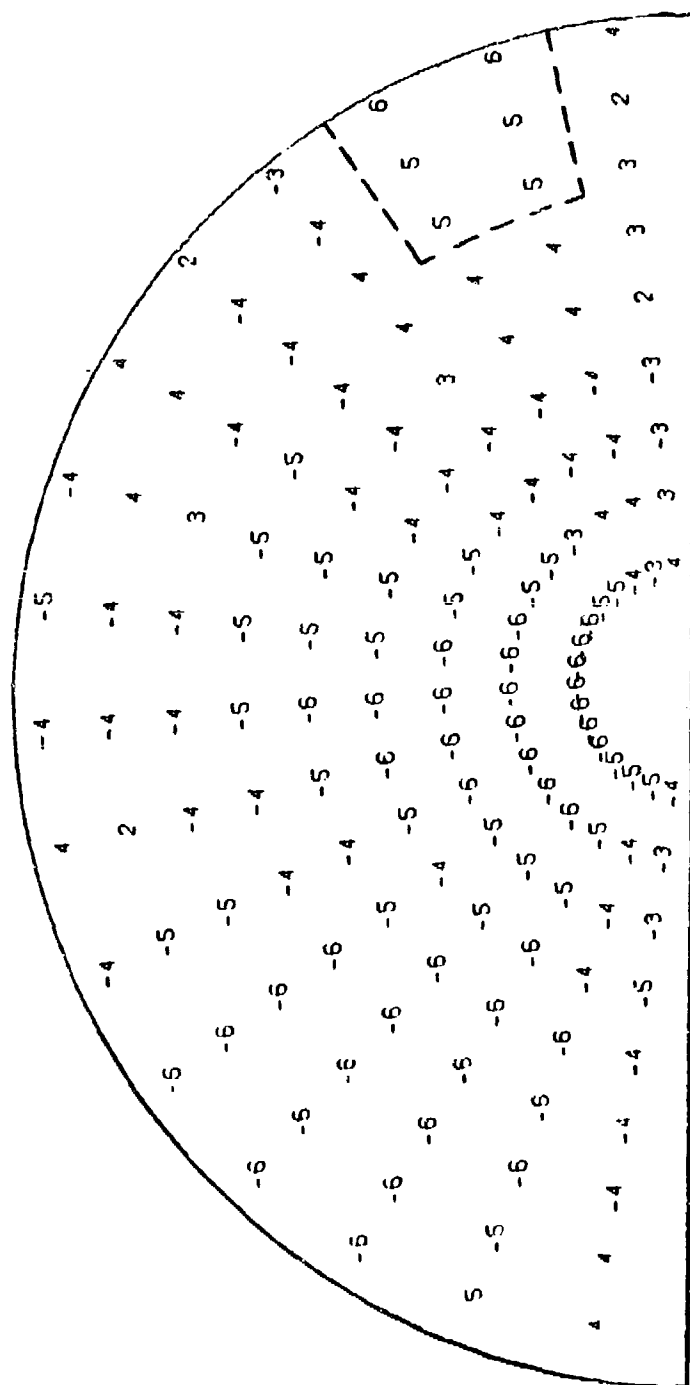
Figure 34. Skull pressure plot along 0° line for crushable skull two-dimensional model.

axis for a crushable diplöe model.

The elastic-plastic diplöe model limits the deviators as described by equation 39. Figure 35 displays the generally reduced tensile pressures in the brain that result from impact to this model. The peak contre-coup rarefaction pressure is reduced by one half compared to the elastic model. There is still substantial rapid positive to negative pressure fluctuation that indicates the pressure waves are not greatly smoothed. If a more efficient yield stress mechanism (such as work or strain hardening) was experimentally determined to exist in the diplöe, then even greater pressure reduction and more smoothing could be obtained.

The crushable foam diplöe model is a more efficient energy absorber than the elastic-plastic model, and it is specifically designed to reduce the peak levels of pressure pulses. Therefore, the protection afforded by this model yielded the most significant reduction of potentially dangerous mechanical forces.

To provide some continuity with previous experimental investigations, a crushable diplöe model was analyzed utilizing the initial crushing pressure and final crushing pressure as evaluated by Melvin, et al (1970) and McElhaney, et al (1970). The general levels and peak tensile pressures were slightly lower than for the elastic-plastic model with a lower yield point. No plots were constructed for this model. The reduced pressure was observed from the data printed during the computer analysis.

Figure 36 shows the pressure along the 180° line for the crushable model with a lower initial crushing value. The general smoothing of the curves represents a drastic modification compared to the elastic model results. The highest rarefaction occurs at about 2.0 units of time. With the elastic skull
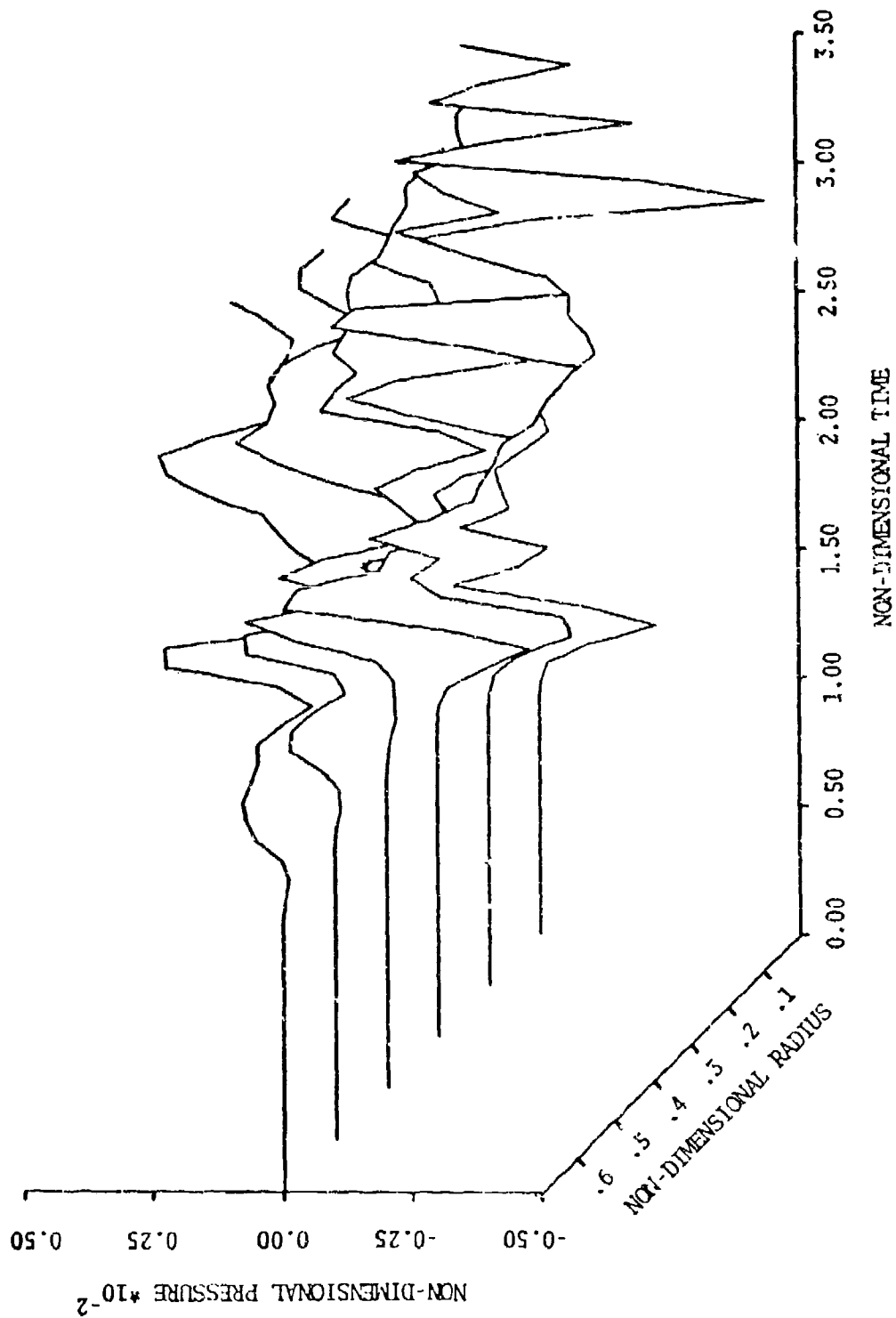
Figure 35. Perspective plot of pressure along 180° line for elastic-plastic skull two-dimensional model.
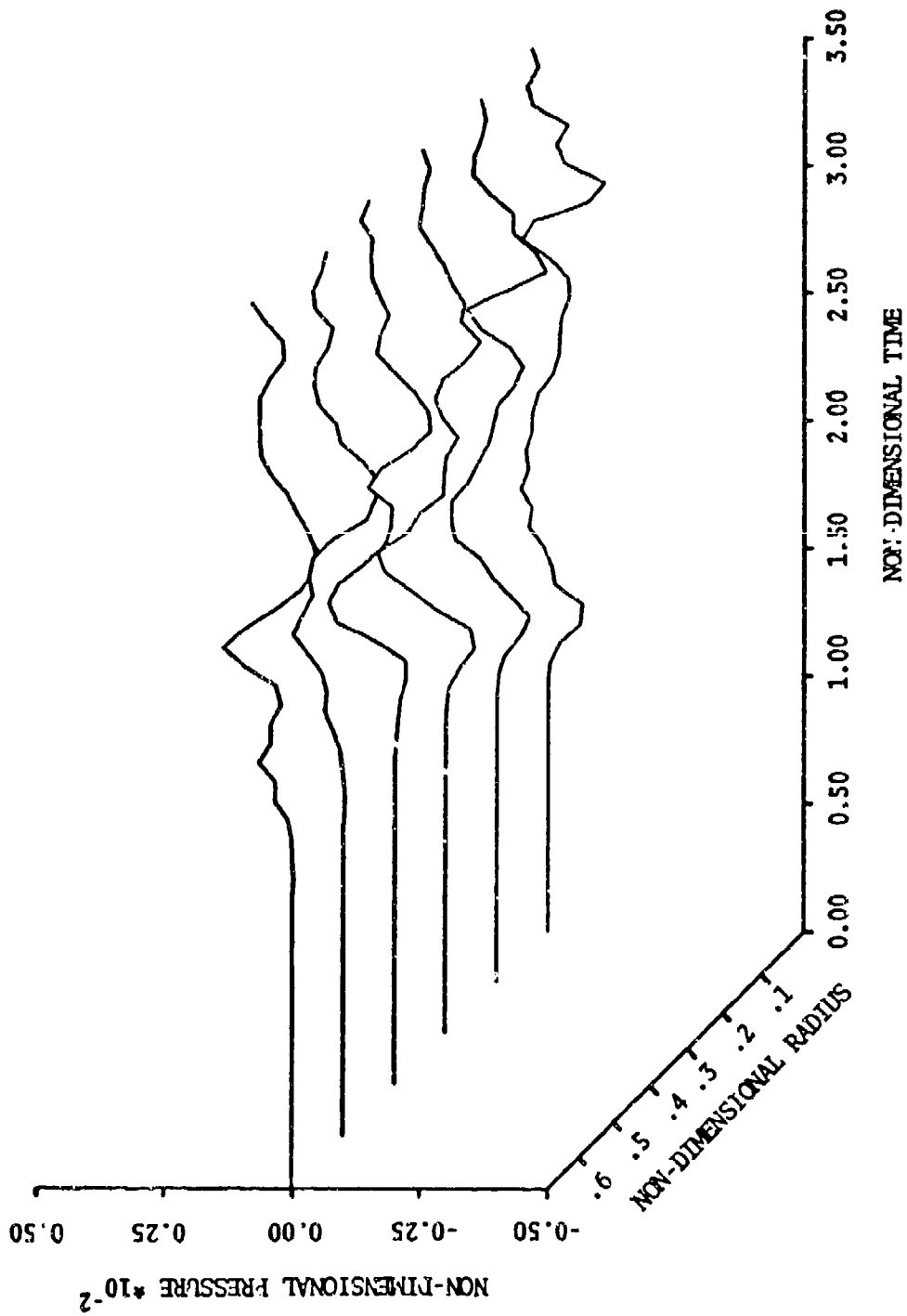
Figure 36. Perspective plot of pressure along 180° line for crushable skull two-dimensional model.

model there was a peak at the time of 2.0, but a larger value appeared at 2.8 units. The crushable analysis peak was less than one fourth of that for the elastic analysis. The pressure profile at the time of peak rarefaction (see Figure 37) shows a wedge shaped, very diffuse, and lower valued concentration of tensile pressure at the contre-coup site. The combination of acoustic impedance mismatch plus strong energy absorption in the diplöe region result in substantial protection against head impact injury.

The internal energy in the brain region was not available as magnetic tape output from the computer analysis. Therefore, the hand plotted internal energy versus time curve appears in Figure 38. The general periodic peaking was not as regular as for the one-dimensional analysis. While stress waves carry energy into and out of the brain region, there are specific times at which the spherical shape produces strong reinforcement peaks. The higher initial crushing value model transmitted less energy to the brain than the elastic-plastic model with a reduced yield stress. The lower crushing value foam model yielded the least energy in the brain. While internal energy represents positive as well as negative stress, it is interesting to note that the elastic model shows peaks at the dimensionless times of 2.0 and 2.8 and the lower crushing value foam model shows no peak at 2.8. The pressure plot observations of rarefaction peaks in the brain with the addition of more energy absorption in the diplöe are closely matched by the reduced internal energy results. This indicates the general usefulness of this method for comparing protection from different head models.
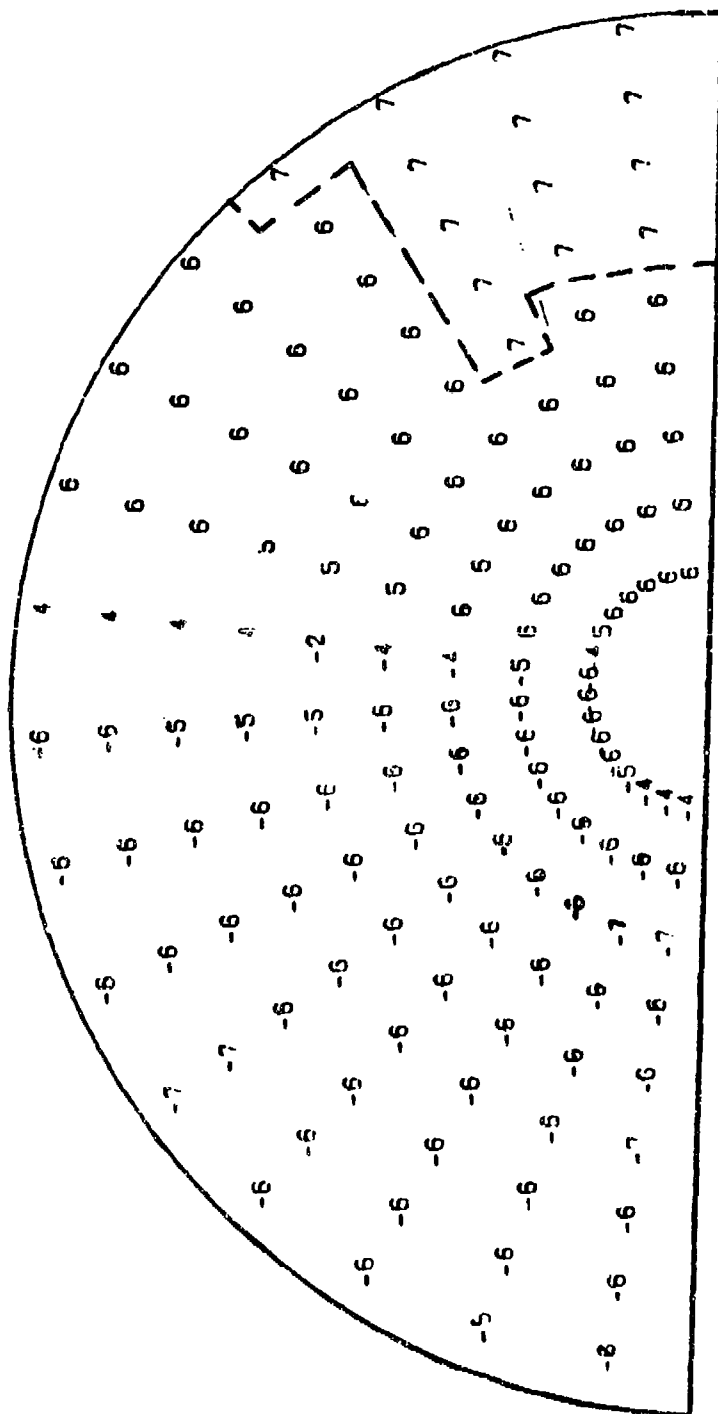
Figure 37 - Pressure Profile at Dimensionless Time of 2.0
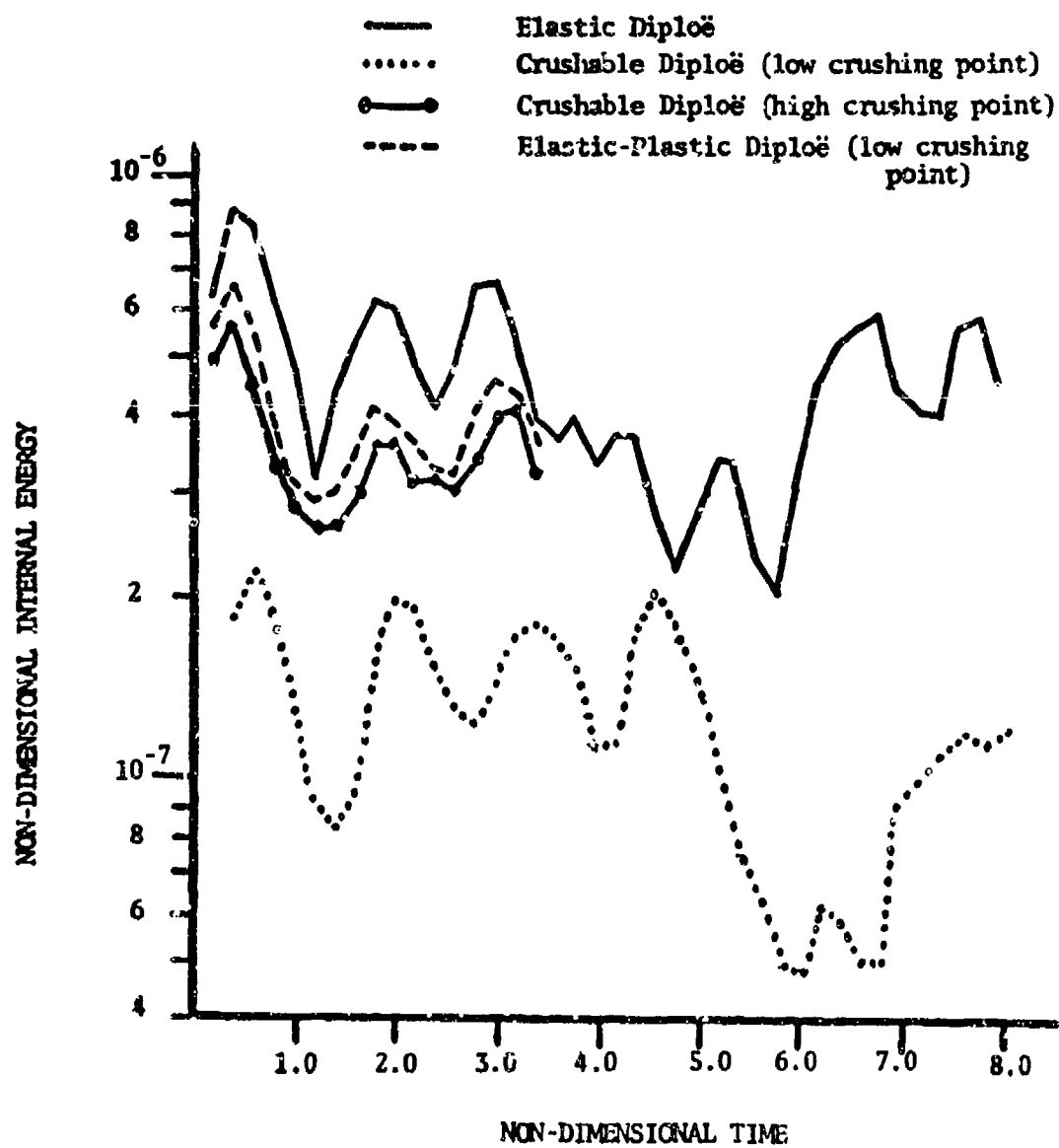for Crushable Skull Two-Dimensional Model

Figure 38. Internal energy in brain of two-dimensional analyses.

Experimental Analysis

Several selected photographic results from the dynamic photo-elastic experiments are shown in Figure 39 to Figure 45. The dark fringe wave front is traveling from right to left in all frames, and the time difference between frames is indicated under the photographs (if applicable). The dark circle at the boundary between inner disk and outer ring and around a few diplöe holes was the result of a pre-stress from the machining and casting processes. Despite this flaw in the model making techniques, the stress wave propagation is clearly observable. The original photographs are Polaroid prints with each frame being about .80 cm by 1.50 cm. In certain frames with poor lighting, the blown up figure is unfortunately not a high quality print.

Plane waves entering the small holes of the table models remained almost plane and completely continuous while traversing the holes and also emerged as a plane wave (as shown in Figures 39 and 40). The pulse size of the main pressure front can be approximated by multiplying the pulse duration (10μsec, as determined from preliminary studies) times the wave speed in PSM-5 (1830 cm/sec). The resulting pulse width of 1.83 cm is much larger than each individual hole depth so that the wave can start to re-group before the next line of holes is encountered (one diameter). Previous studies (Rose, Mortimer, and Chou (1973)) indicated that for pulse widths at least as large as the hole depth the wave front can regroup in two characteristic lengths. Characteristic length is defined as the hole dimension parallel to the wave front. It should be noted that the lining up of small holes parallel to the wave front helps to maintain a wave with slightly rippled form, but does little to aid in obtaining a continuous wave. The small characteristic length of each hole provides the primary enhancement for re-grouping as a continuous wave. Also
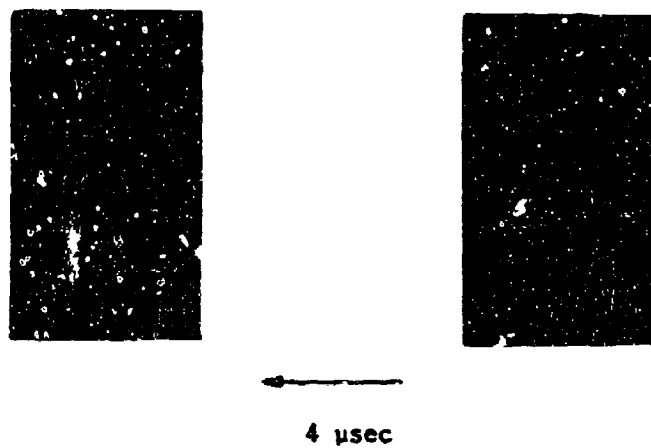
4 µsec

Figure 39. Photoelastic stress waves in table region with PL-2 filler.

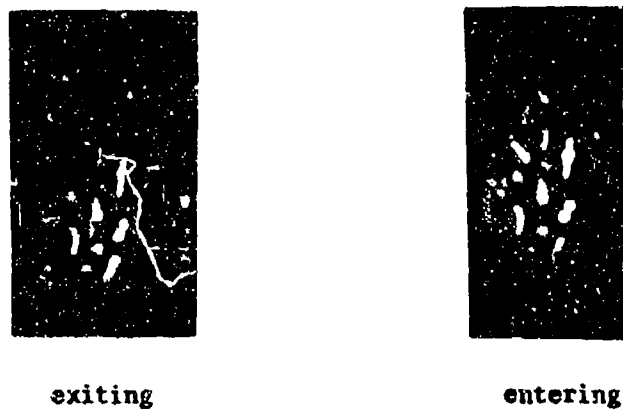exiting   entering

Figure 40. Photoelastic stress waves entering and exiting table region with Solithane 113 filler.

the entire table region is thinner in depth than the pulse width; therefore, this total section acts as an effective inclusion which can be traversed as a continuous and plane wave.

PL-2 and Solithane 113 models yielded approximate wave speeds in the small hole region of 1710 and 1690 cm/sec respectively. These values are nearly equal (despite the difference in filler properties) and are closer to the PSM-5 wave speed than to the filler wave velocity. The similarity in wave speed and wave form results of the two table models suggests that the geometrical considerations of small individual hole size, closely packed arrangement and thin overall depth are more significant than the filler material utilized.

The larger holes of the diplöe region had a more pronounced effect on the wave motion. With the PL-2 filler the wave front was highly irregular, but continuous. However, the Solithane 113 model produced a non-continuous wave that energed as distinct rays emanating from the solid portions of the model. The larger characteristic length of each hole did not enhance re-grouping before the next cavity was met. Also the entire diplöe region was larger than the input pulse width. The general effect was that only in the case of a small acoustic impedance mismatch could the wave remain continuous. These wave propagation results can be observed in Figures 41 and 42. The concentration of stress in the solid portions of the diplöe indicate a region of early failure as suggested by Melvin, et al (1970).

Because of the large depth of the entire diplöe section it was impossible to observe a wave entering and exiting the diplöe during the 12μsec period of a single test. By noting the time duration between a wave exiting the large holes (in the Solithane 113 model) and a wave passing through a similar
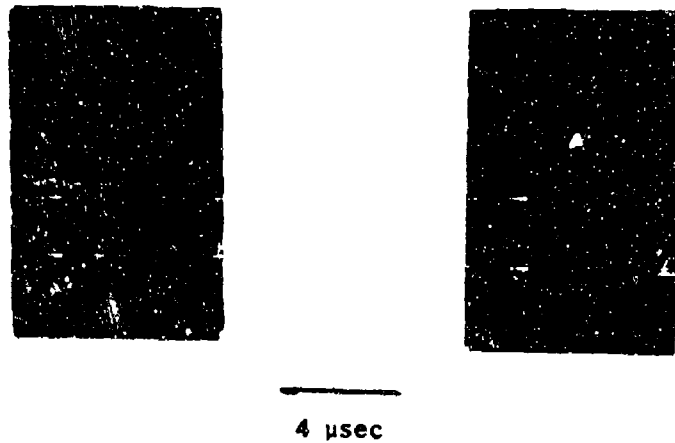
4 μsec

Figure 41.   Photoelastic stress waves in diploe region with PL-2
filler.

Figure 42.   Photoelastic stress waves in diploe region with Solithane
113 filler.

location on the reference plate (opposite side of the exploding wire), the overall average speed in both regions of the skull model is computed as 1525 cm/sec. This overall value suggests that the speed in the diplöe is slower than in the table region.

All of the exploding wire tests are in the elastic range because there are no permanent deformations in the table or diplöe regions. Therefore, the experimental comparisons with the theoretical analysis are applicable for the initial time period before crushing can begin. The slower wave speeds in the diplöe region are physically predictable and in agreement with the findings of the West Virginia Biomechanics Laboratory (1970). These results add confidence to the relative wave speed values employed in the theoretical analysis.

The exact nature of wave propagation is of course, strongly dependent on the relationship between hole size and pulse size. While the plastic skull model is proportional to the human head, the hole size to pulse size ratio for the model is higher than for direct impact to an actual head. The photoelastic results, using PL-2 which is closer to the fluid filled diplöe properties, can be extended to yield a qualitative approximation of the wave form during head impact. The microscopic cavities of the table regions probably have little effect on the wave motion other than to slightly reduce the wave speed. The larger spaces in the diplöe (but smaller than the plastic model holes) yield a continuous but not perfectly planar wave form with a lower wave velocity than the table region. Because the non-planar motion in the diploe will reform into a plane wave after traveling through the inner table, the small ripples in the wave form are considered secondary compared to the crushing effects. Additionally, it would be theoretically

impossible to incorporate all of the inhomogeneous diploe inclusions in the analysis.

The disk and concentric ring photoelastic head model provided direct observation of stress waves traveling through the brain and around the skull model analogs. A mathematical analysis of this plastic head model (with PL-2 disk) was performed using the "TOCDY-IV" computer code. A cylindrical theoretical geometry was used (similar to the shape shown in Figure 4-a) that does not allow for possible edge effects present in a thin plastic model. Except for this infinite thickness, the cross-sectional configuration is the same for both models. The early time results for each analysis (least affected by edge effects) have been compared, and the correlations are in close agreement.

The wave form for both analyses had similar characteristic shapes. As the wave front started to enter the central disk, the wave had traveled approximately 45° in the outer ring of each model. The curved wave form in the shell of both models indicated the slower wave velocity due to contact with lower acoustic impedance materials at the inner and outer shell radii. A slight advancement of the wave front along the symmetry axis as compared to other locations showed the geometric dispersion that exists in the disk region. As pressure starts to be generated inward from the shell (as the wave passes around the outer ring), the wave front in the disk attains a crescent shape (see Figure 43). When the wave reaches the opposite side from the exploding wire, there is a strong concentration of stress along the outer radius of the disk. Figure 44 shows the distinctive horseshoe shape that resulted with the Solithane 113 disk. The acoustic impedance mismatch is so large that the wave is almost completely around the outer

Figure 43.   Photoelastic stress waves in head model with PL-2
brain region.

Figure 44.   Photoelastic stress waves in head model with Solithane
113 brain region.

ring before the wave enters the disk; therefore, pressure generated inward from the ring has gone through a larger angle than with the PL-2 disk.

The dark stress fringes are representative of an isochromatic line which implies a constant difference between two principle stresses. The theoretical results are displayed as a plot of the principle stress differences versus position at 4μ sec intervals. In order to show the principle stress difference profiles, relative values indicated are based on a linear scale from 1 to 9. The actual leading and trailing edges of the wavefront include several values lower than 1 on the relative scale. These lower level principle stress differences are all listed as 0.

Figure 45 shows the photographic experimental and calculated theoretical wave forms for two similar times. The mathematical wave form is sketched by using the two highest values in the outer ring and the highest value in the disk. Lower isochromatic theoretical lines are found in the disk region because of the lower shear modulus. Both symmetric halves of the theoretical results in the ring and disk (not the short support strut) are presented. The primary wave fronts in both models have a similar form. The probable causes of discrepancies between the two models are imperfections in the molded and machined plastic model, inaccurate mathematical modeling of the pressure pulse, and incorrect material property values for the theoretical analysis. The general agreement between the models provides qualitative confidence in the theoretical solution technique.
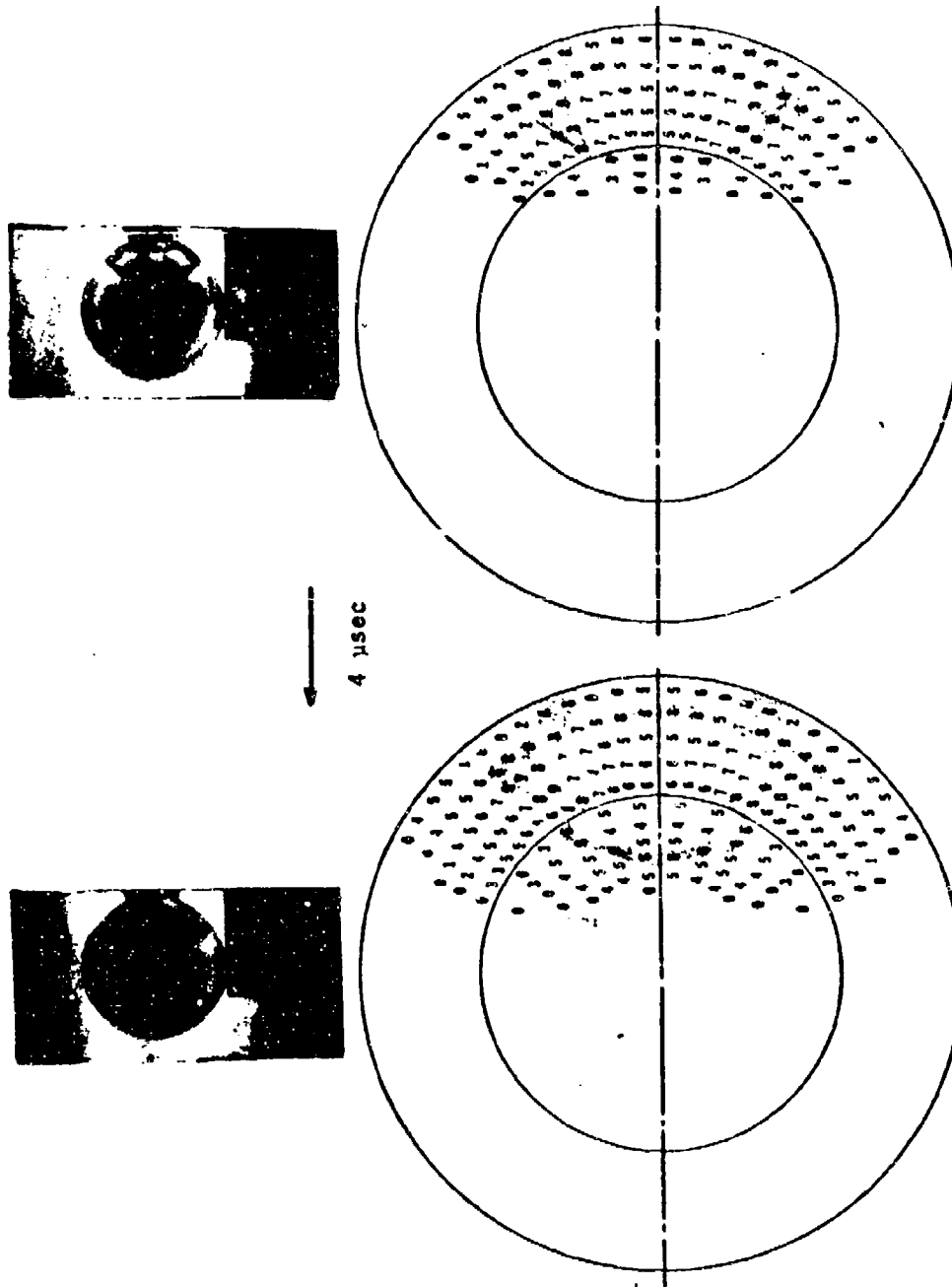
Figure 45. Correlation of experimental and theoretical ring and con-
centric disk head model.

VI - SUMMARY AND CONCLUSIONS

There is a lack of high frequency experimental data to describe the
mechanical properties of the head. The present analysis is based on the
best available test data and several approximations and modifications re-
quired to evaluate certain physical effects. While the analysis does not
include every layer of material in the head and the constitutive proper-
ties assumed are not perfect, it represents a reasonable approach for
theoretically studying several mechanisms that can strongly influence head
impact damage.

The "WONDY-IIIa" and "TOODY-IV" computer codes have been developed
and verified experimentally over a number of years. Internal error checks
supply a continuous check of accuracy and stability. The two-dimensional
elastic skull results bear strong resemblance to the analytic solutions of
Engin (1969) and Liu, et al (1971). Dynamic exploding wire studies of im-
pact to a photoelastic head model correlate qualitatively with the theoretic-
al two-dimensional analysis of a similar problem. In general, there is
confidence in the applicability and accuracy of the finite difference solu-
tion techniques.

The one-dimensional analysis provides an economic (in terms of computer
costs) method of predicting the influence of several material property and
size modifications in a geometrically simplified head impact model. The
greatest modelling error in this analysis is the lack of a closed container
that causes pressure amplification due to the spherical shape. Various
diploe models indicate the effects of impact to regions with a thicker diploe
and possibly modified dynamic acoustic properties. A potential parameter
for optimization of energy absorption is analysed for the crushable foam

diplöe model. Rarefaction waves are generated solely from acoustic mismatches at material interfaces.

The two-dimensional analysis predicts regions of high tensile pressure that correspond to coup, contre-coup, and intermediate coup injuries. Two types of pressure pulses generated wedge shaped tension areas at the contre-coup site. Very high level short duration spikes could cause failure by exceeding a critical tensile pressure level. A broader and weaker pressure pulse appeared that could cause tissue or vessel damage by remaining above a rarefaction injury level for a longer duration. Shear stress was evaluated in an elastic brain model. The combined shear-normal stress levels suggest that high tensile stress in the presence of a smaller shear stress is more likely to produce failure than the shear free stress conditions in a hydro-dynamic brain model. Impact to the multi-layered skull models yielded large reductions in rarefaction pressures in the brain. The acoustic impedance mismatch and the energy absorption (especially in the crushable foam model) utilized by including the diplöe layer of the skull, provided excellent protection against impact brain damage.

There are two general conclusions to be drawn from the analyses discussed in this work. First, the quantitative effects of including a layered energy absorbing skull and the possible existence of a high dynamic shear modulus for brain tissue have significant influence on the potentially damaging mechanical forces that result from head impact. Second, the generality of the solution techniques readily permits the extension of the analyses to investigate the importance of additional layers, new material definitions, more complex geometries, or different types of impact.

VII - RECOMMENDATIONS

Three areas for future research based on the findings of the present work are as follows: (1) modifications to the head impact model, (2) head protective device models, and (3) improvements in the analysis techniques.

The head impact modelling could be extended in several ways. Improved experimental high frequency evaluation of head component material properties and failure mechanisms is a primary area for head impact research. Two other head layers should be added to the present model. Impact transmitted through the scalp might yield a more gradual input energy pulse. The influence of including the meningeal region (or a mathematical slippage at the inner table-brain boundary) should be determined. Impactor modifications could include using a combined translation and surface traction load (as described by Chan (1971) or varying the size and velocity of the impactor. A final change in the analysis would be to study the effects of a more complex geometry such as an ellipsoidal shell. The present modelling techniques can be readily adjusted to include the above considerations.

The crushable foam diploe model produced reductions in potentially damaging forces in the brain. This energy absorption concept can be extended to include the addition of protective helmet layers between the impactor and outer head layer. Maximum reduction of energy transmission to the brain can be obtained by varying material properties and sizes and choosing the proper order of layering.

Excessive computer costs indicate that a more economic analysis would permit more parameter modifications and longer extension of the problem times. An accurate combination of several layers into one effective layer would simplify the helmeted head impact model. Another type of approximation theory (such as finite element or method of characteristics) might be

more efficient. Several new techniques for hybrid solution for systems of partial differential equations can be considered. A final approach is the use of mathematical manipulation of shell theories to reduce the solution to a simple analytic form. The present finite difference method will provide a useful tool for evaluating any new solution techniques.

BIBLIOGRAPHY

Advani, S. H., and Lee, T. *Structural Investigations of Crania-Cerebral Trauma*. West Virginia University final report: *Determination of the Physical Properties of Tissues of the Human Head*. Contract No. PH-43-67-1137, 1970.

Anzelius, A. *The Effect of an Impact on a Spherical Liquid Mass*. <u>Acta Path. Microbiol.</u>, Suppl. 48, 153-159, 1943.

Benedict, J. V. *An Analysis of an Impact Load, Fluid-Filled, thin Spherical Shell as a Mathematical Model for an Investigation of the Cavitation Theory of Brain Damage*. A doctoral thesis at Tulane University, 1969.

Benzley, S. E.; Bertholf, L. D.; Clark, G. E. TOODY II-A A Computer Program for Two-Dimensional Wave Propagation - C.D.C. 6600 Version Sandia Laboratory Report No. SC- DR- 69-516, Oct., 1969.

Chan, H. S. "The Asymmetric Response of a Fluid-Filled Spherical Shell - A Mathematical Simulation of Head Injury." A doctoral thesis, Tulane University, Nov., 1971.

Chou, P. C., and Pagano, N.J. *Elasticity*. Publ. by D. Van Noftrand Co., Princeton, N.J., 1967.

Engin, A. E. The Axisymmetric Response of a Fluid-Filled Spherical Shell S to a Local Radial Impulse - A Model for Head Injury. <u>J. Biomechanics</u> 2:325-341, 1969.

Engin, A. E., and Liu, Y. K. *Axisymmetric Response of a Fluid-Filled Spherical Shell in Free Vibration*. <u>J. Biomechanics</u> 3:11-22, 1970.

Estes, M. S., and McElhaney, J. H. *Response of Brain Tissue of Compressive Loading*. ASME 70-BHF-13, 1970.

Evens, F. G. <u>Stress and Strain in Bones</u>. Thomas Publishers, Springfield, Ill., 1957.

Evans, J. P. *Initial Clinical Appraisal, Grading, and Classification*. Head Injury Conference Proceedings. Ed. by Caveness and Walker, Lippincott, Phila., 1966.

BIBLIOGRAPHY (Continued)

Ewing, L. L.; Thomas, D. J.; Patrick, L. M.; Beeler, G. W.; Smith, M. J. Living Human Dynamics Response to - G_x Impact Acceleration II - Acceleration Measured on the Head and Neck. 13th Stapp Car Crash Conference, 1969.

Fallenstein, G. T., Hulce, V. P., and Melvin, J. W. Dynamic Mechanical Properties of Human Brain Tissue. J. of Biomech. 2:217-226, 1969.

Flynn, P. D. Dynamic Photoelastic Stress Patterns from a Simplified Model of a Head. Head Injury Conference Proceedings. Ed. by Caveness and Walker. Lippincott, Phila., 1966.

Friede, R. L. Experimental Concussion Acceleration. Arch. of Neurology 4:449-461, 1961.

Galford, J. W., and McElhaney, J. H. A Viscoelastic Study of Scalp, Brain and Dura. J. of Biomech. 3:211-221, 1970.

Goldsmith, W. The Physical Processes Producing Head Injuries. Head Injury Conference Proceedings. Ed. by Caveness and Walker. Lippincott, Phila., 1966.

Gosch, H. H.; Gooding E.; Schneider, R. C. The Lexan Calvarium for the Study of Cerebral Responses to Acute Trauma, Journal of Trauma, Volume 10, No. 5, pages 370-376, 1970.

Gross, A. G. A new Theory on the Dynamics of Brain Concussion and Brain Injury. J. of Neurosurgery 15:548-561, 1958.

Gross, A. G. Impact Thresholds of Brain Concussion. J. Aviation Med. 29:275, 1958.

Gurdjian, E. S., Hodgson, V. R., Hardy, W. G., Patrick, L. M., Lissner, H. R. Evaluation of the Protective Characteristics of Helmets in Sports. Journal of Trauma, Volume 4, Number 3 309-324 1964.

Gurdjian, E. S., and Lissner, H. R. Photoelastic Confirmation of the presence of Shear Strains at the Craniospinal Junction in Closed Head Injury. Neurosurgery 18-1:58, 1961.

Gurdjian, E. S., and Webster, J. E. Head Injuries. Publ. by Little, Brown and Co., Boston-Toronto, 1958.

Hayashi, T. Study of Intracranial Pressure caused by Head Impact. Journal of Faculty of Engineering, University of Tokyo, Volume XXX, Number I 59-72, 1969.

Herrmann, W. Constitutive Equation for the Dynamic Compaction of Dactite Porous Materials. J. Appl. Physics 40-6, 1968.

BIBLIOGRAPHY (Continued)

Herrmann, W., Holzhauser, P., and Thomoson, R. J. WONDY, A Computer Program for Calculating Problems of Motion in one direction. Sandia Laboratories Report SC-RR-66-601, 1967.

Herrmann, W., Lawrence, R. J., and Mason, D. S. Strain Hardening and Strain Rate in One-Dimensional Wave Propagation Calculations. Sandia Laboratory Report No. SC-RR-70-471, Nov., 1970.

Hodgson, V. R. and Patrick, L. M. "Dynamic Response of the Human Cadaver Head Compared to a Simple Mathematical Model," 12th Stapp Car Crash Conference, 1968.

Holbourn, A. H. S. Mechanics of Head Injuries. Lancet. 2:438-441, 1943.

Janssen, M. L., and Bowman, C. E. The Dynamic Response of Two-Dimensional Photoelastic Models of the Human Head. ASME paper 70-BHF-15, 1970.

Karnes, C. H. and Bertholf, L. D. Numerical Investigation of Two-Dimensional Axisymmetric Elastic-Plastic Wave Propagation near the Impact end of Identical 1100-0 Aluminum Bars. Sandia Laboratory Report No. SC-R-71-3336, 1971.

Kornhauser, M. Prediction and Evaluation of Sensitivity to Transient Acceleration. Journal of Applied Mechanics, Volume 21, pages 371-375, 1954.

Langfitt, T. W., Weinstein, J. D., and Kassell, H. F. "Vascular Factors in Head Injury: Contribution to Brain Swelling and Intracranial Hypertension. Head Injury Conference Proceedings. Ed. by Caveness and Walker. Lippincott, Phila., 1966.

Lawrence, R. J. WONDY IIIa: A Computer Program for one-dimensional Wave Propagation. Sandia Laboratories Report SC-DR-70-315, 1970.

Lawrence, R. J., Mason, D. S., Benzley, S. E. Dynamic Material Property Library. Sandia Laboratories Report SC-DR-68-885, 1968.

Lee, E. H. Elastic-Plastic Waves of One-Dimensional Strain. Fifth U. S. National Congress of Applied Mechanics Proceedings, 405-420, 1966.

Lindenberg, R. and Freytag, E. Morphology of Cortical Contusions. Archives of Pathology, Volume 63, 23-43, 1957.

Liu, Y. K. The Biomechanics of Spinal and Head Impact: Problems of Mathematical Simulation. Procedure of Symposium on Biodynamic Modelling and its Applications, Dayton, Ohio, 1970.

Liu, Y. K., Chan, H. S., and Nelson, J. Intracranial Pressure Wave Propagation in Closed Head Impact. Procedure Summer Computer Simulation Conference, Boston, Mass., pages 984-994.

BIBLIOGRAPHY (Continued)

Lombard, C.; Roth, H.; Gross, A.; Klein, A.; Ames, S. Impact Tests of Protective Headgear-Preliminary Report, Dept. of Aviation Med. University of Southern California, Los Angeles, Jan. 25, 1969.

Lundergan, C. D. and Drumheller, D. S. Dispersion of Shock Waves in Composite Materials. Journal of Applied Physics, Volume 42, Number 2, Feb., 1971.

Mahone, R., Corrao, P., Ommaya, A. K., Hendler, E., and Schulman, M. A Theory on the Mechanics of Whiplash-Produced Concussion in Primates. Unpublished paper presented at ASMA Meetings, San Francisco, 1969.

Martin, B. and McElhaney, J. H. The Acoustic Properties of Human Skull Bone, Journal of Piomedical Materials Volume 5, 325-333, 1971.

McElhaney, J. H., and Byars, E. F. Dynamic Response of Biological Materials, ASME 65-WA/HUF-9, 1965.

McElhaney, J. H., Fogle, J. L., Melvin, J. W., Haynes, R. R., Roberts, V. L., and Alem, H. H. Mechanical Properties of Cranial Bone. J. of Biomech. 3:495-511, 1970.

McElhaney, J. H., Roberts, V. L. and Stalmaker, R. L. The Biomechanical Aspects of Crash Helmet Design AGARD Meeting, Oporto, Portugal, June 1971.

Melvin, J. W., Fuller, P. M., and Barodawala, I. T. The Mechanical Properties of the Diploe Layer in the Human Skull. 1970 SESA Spring Meeting, Huntsville, Ala.

Mendelson, A. Plasticity: Theory and Application. MacMillan Corp. New York, 1968.

Ommaya, A. K. Experimental Head Injury in the Monkey. Head 'njury Conference Proceedings. Ed. by Caveness and Walker. Lippincott, Phila., 1966.

Ommaya, A. K. Mechanical Properties of Tissues of the Nervous System, J. of Biomech. 1:127-138, 1968.

Ommaya, A. K. The Physiopathology of Head Injuries. Committee on Hearing, Bioacoustics, and Biomechanics, Nov., 1969.

Ommaya, A. K., Hirsch, A. E., Martinez, J. L. The role of Whiplash in Cerebral Concussion. 10th Stapp Car Crash Conference Proceedings, 197-203, 1966.

BIBLIOGRAPHY (Continued)

Ommaya, A. K., Yarnell, P., Hirsch, A. E., Harris, E. H.   Scaling of
Experimental Data on Cerebral Concussion in Sub-Human Primates to
Concussion Threshold for Man.   11th Stapp Car Crash Conference pages
47-52, 1967.

Patrick, L.   Head Impact Protection.   Head Injury Conference Proceedings.
Ed. by Caveness and Walker.   Lippincott, Phila., 1966.

Pudenz, R. H., and Shelden, C. H.   The Lucite Calvarium - A Method for
Direct Observation of the Brain - II Cranial Trauma and Brain Movement.
Journal of Neurosurgery.   3:487, 1946.

Rand, R., and DiMaggio, F.   Vibrations of Fluid Filled Spherical and
Spheroidal Shells.   J. Acoustic Society Am.   42:1278-1286, 1967.

Rayne, J. M. and Maslen, K. R.   Factors in the Design of Protective
Helmets.   Aerospace Medicine, pages 631-637, June, 1969.

Roberts, V. L., Hodgson, V. R., and Thomas, L. M.   Fluid Pressure Gradients
caused by Impact to the Human Skull.   ASME paper 66-HUF-1, 1966.

Rose, J. L., and Chou. F. C.   Phtoelastic Study of Stress Waves Generated
by Exploding Wires.   1970 SESA Fall Meeting, Boston, Mass.

Rose, J. L. and Chou, P. C.   Study of Cylindrical Stress Waves Generated
by Exploding Wires.   Experimental Mechanics, Feb., 1972.

Shuck, L. Z., Haynes, R. R., and Fogle, J. L.   Determination of Visco-
Elastic Properties of Human Brain Tissue.   ASME paper 70-BHF-12, 1970.

Stalmaker, R. L., Fogle, J. L. and McElhaney, J. H.   Driving Point Impedance
Characteristics of the Head.   ASME paper 70 BHF-14, 1970.

Stapp, J. P.   Human Exposure to Linear Deceleration-Part 2.   Air Force
Technical Report 5915, Dec., 1957.

Stritch, S. J.   Diffuse Degeneration of the Cerebral White Matter in Severe
Dementia Following Head Injury.   Journal of Neurology, Neurosurgery,
Psychiatry.   Volume 19, 163-185, 1956.

Stritch, S. J.   Shearing of Nerve Fibres as a cause of Brain Damage due to
Head Injury.   Lancet, 443-448, August, 1961.

Unterharnscheidt, F., and Higgins, L.   Pathomorphology of Experimental Head
Injury due to Rotational Acceleration.   Acta Neuropath.   12:200-204, 1969.

BIBLIOGRAPHY (Continued)

Unterharnscheidt, F., and Sellier, K. Closed Brain Injuries: Mechanics and Pathomorphology. Head Injury Conference Proceedings. Ed. by Caveness and Walker. Lippincott, Phila., 1966.

Unterharnscheidt, F., and Sellier, K. Pathomorphology of Non-Penetrating Brain Injuries. Third International Congress of Neurosurgery Proceedings, 93-103, 1965.

von Gierke, H. E., On the Dynamics of some Head Injury Mechanisms. Head Injury Conference Proceedings. Ed. by Caveness and Walker, Lippincott, Phila., 1966.

Walker, A. E. Introduction. Head Injury Conference Proceedings. Ed. by Caveness and Walker, Lippincott, Phila., 1966.

West Virginia University Biomechanics Laboratory. Determination of the Physical Properties of Tissues of the Human Head. Contract No. PH-43-67-1137, final report, 1970.

Wood, J. L. Dynamic Response of Human Cranial Bone. J. Biomechanics 4:1-12, 1971.

APPENDIX A

Complete List of Finite Difference Equations
For the Two-Dimensional Analysis

In Chapter III - Theoretical Modelling, the general form of the governing two-dimensional equations was discussed. The following section represents a complete list of the necessary equations for solving the finite difference analysis of head impact. Each grid zone utilizes similar wave propagation relationships. The equations given below are for a typical elastic material grid zone.

The nodal location identifiers and all notations are described in Figure A-1 and List of Symbols. It is assumed that values for all variables are known at time n. The system of equations given below computes the new values for all variables at time n+1 for the 1st zone called region 3 (also defined by nodal point 0). After completing the solution for a particular zone, the next zone is temporarily identified as region 3, and the computations are repeated.
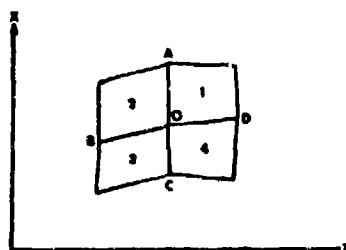

Figure A1. Grid Zone Description for Finite
Difference Algorithm

The conservation of linear momentum expressions yield the following acceleration values for grid zone 3 at time n (note: the stress values are the sum of the constitutive stress terms plus the artificial viscous stress terms):

$$(a^x)_0^n = -\frac{1}{\rho A} [\tau_1^{xx}(z_a-z_b)+\tau_2^{xx}(z_b-z_a)+\tau_3^{xx}(z_c-z_b)+\tau_4^{xx}(z_d-z_c)]$$

$$+\frac{1}{\rho A} [\tau_1^{xz}(x_a-x_d)+\tau_2^{xz}(x_b-x_a)+\tau_3^{xz}(x_c-x_b)+\tau_4^{xz}(x_d-x_c)] \qquad A1$$

$$+\frac{1}{4} [(\tau_1^{xx}-\tau_1^{yy})\frac{a_1}{m_1}+(\tau_2^{xx}-\tau_2^{yy})\frac{a_2}{m_2}+(\tau_3^{xx}-\tau_3^{yy})\frac{a_3}{m_3}+(\tau_4^{xx}-\tau_4^{yy})\frac{a_4}{m_4}]$$

$$(a^z)_0^n = -\frac{1}{\rho A} [\tau_1^{xy}(z_a-z_d)+\tau_2^{xy}(z_b-z_a)+\tau_3^{xy}(z_c-z_b)+\tau_4^{xx}(z_d-z_c)]$$

$$+\frac{1}{\rho A} [\tau_1^{zz}(x_a-x_d)+\tau_2^{zz}(x_b-x_a)+\tau_3^{zz}(x_c-x_b)+\tau_4^{zz}(x_d-x_c)] \qquad A2$$

$$+\frac{1}{4} [\tau_1^{xz}\frac{a_1}{m_1}+\tau_2^{xz}\frac{a_2}{m_2}+\tau_3^{xz}\frac{a_3}{m_3}+\tau_4\frac{a_4}{m_4}] .$$

The value for ρA is obtained from the value of the regions surrounding point 0 as

$$\rho A = \frac{1}{\rho} [\rho_1 A_1 + \rho_2 A_2 + \rho_3 A_3 + \rho_4 A_4] . \qquad A3$$

The velocity of point 0 is advanced in time by

$$(u^x)_0^{n+1/2} = (u^x)_0^{n-1/2} + 1/2(\Delta t^{n+1/2}+\Delta t^{n-1/2}) (a^x)_0^n$$

$$(u^z)_0^{n+1/2} = (u^z)_0^{n-1/2} + 1/2(\Delta t^{n+1/2}+\Delta t^{n-1/2}) (a^z)_0^n . \qquad A4$$

Similarly, the new location of point 0 is given by

$$x_0^{n+1} = x_0^n + \Delta t^{n+1/2} (u^x)_0^{n+1/2}$$

$$z_0^{n+1} = z_0^n + \Delta t^{n+1/2} (u^z)_0^{n+1/2} \qquad A5$$

The stretching deviators contain local strain rate and dilatation components. The final difference form for these deviators at time n+1/2 is given by (Note: $d_d^{yy'}$ is eliminated)

$$d_d^{xx} = \frac{[(u^x)_o - (u^x)_f][z_c^{n+1} + z_c^n - z_b^{n+1} - z_b^n] - [(u^x)_c - (u^x)_b][z_o^{n+1} + z_o^n - z_f^{n+1} - z_f^n]}{2[a^{n+1} + a^n]}$$

$$+ \frac{2}{3} \frac{\rho_3^{n+1} - \rho_3^n}{(\rho_3^{n+1} + \rho_3^n) \, \Delta\tau^{n+1/2}}$$

$$d_d^{zz} = \frac{[(u^z)_o - (u^z)_f][x_c^{n+1} + x_c^n - x_b^{n+1} - x_b^n] - [(u^z)_c - (u^z)_b][x_o^{n+1} + x_o^n - x_f^{n+1} - x_f^n]}{2[a^{n+1} + a^n]} \qquad A6$$

$$+ \frac{2}{3} \frac{\frac{n+1}{3} - \frac{n}{3}}{(\rho_3^{n+1} + \rho_3^n) \, \Delta\tau^{n+1/2}}$$

$$d_d^{xz} = \frac{[(u^x)_o - (u^x)_f][x_c^{n+1} + x_c^n - x_b^{n+1} - x_b^n] - [(u^x)_c - (u^x)_c][x_o^{n+1} + x_o^n - x_f^{n+1} - x_f^n]}{4[a^{n+1} + a^n]}$$

$$+ \frac{[(u^z)_o - (u^z)_f][z_c^{n+1} + z_c^n - z_b^{n+1} - z_b^n] - [(u^z)_c - (u^z)_c][z_o^{n+1} + z_o^n - z_f^{n+1} - z_f^n]}{4[a^{n+1} + a^n]} \; .$$

Equations A1,A2,A3 and A6 require density and area values that are obtained from the following expressions:

$$m_3 = v_3^o \, \rho_o,$$

$$\rho_3^{n+1} = \frac{m_3}{v_3^{n+1}} \qquad\qquad A7$$

$$v_3^{n+1} = \frac{1}{3} a_3^{n+1}(x_o + x_b + x_c + x_f) + \frac{1}{6} [z_f x_o - z_o x_f) \cdot (x_b - x_c) + (z_b x_c - z_c x_b)(x_o - x_f)],$$

and, $a_3^{n+1} = \frac{1}{2} [(z_c - z_b)(x_o - x_f) + (z_o - z_f)(x_b - x_c)]$.

The assumed energy independent nature of the constitutive equations yields the following hydrodynamic pressure relationship

$$.p_3^{n+1} = K\, n^{n+1}.$$

<div align="right">A8</div>

The stress deviator computations require the rigid body rotation (w^{xz}) at time $n+1/2$ given as

$$w^{xz} = \frac{[(u^x)_o - (u^x)_f][x_c^{n+1} + x_c^n + x_b^{n+1} + x_b^n] - [(u^x)_c - (u^x)_b][x_o^{n+1} + x_o^n - x_f^{n+1} - x_f^n]}{4[a^{n+1} + a^n]}$$

$$\frac{[(u^z)_o - (u^z)_f][z_c^{n+1} + z_c^n - z_b^{n+1} - z_b^n] - [(u^z)_c - (u^z)_b][z_o^{n+1} + z_o^n - z_f^{n+1} - z_f^n]}{4[a^{n+1} + a^n]}$$

<div align="right">A9</div>

Now using Hooke's Law the deviator stress components can be computed as

$$(d_\tau xz)^{n+1} = \left\{ \frac{1 - (u^{xz^{n+1/2}} \Delta t^{n+1/2})^2}{1 + (u^{xz^{n+1/2}} \Delta t^{n+1/2})^2} \right\} (d_\tau xz)^n + \frac{d_\tau xz}{1 + (u^{xz^{n+1/2}} \Delta t^{n+1/2})^2}$$

$$\frac{u^{xz^{n+1/2}} \Delta t^{n+1/2}}{1 + (u^{xz^{n+1/2}} \Delta t^{n+1/2})^2} \left\{ (d_\tau xx)^n - (d_\tau xx)^n + 1/2(\Delta d_\tau xx - \Delta d_\tau zz) \right\}$$

and,

$$(d_\tau xx)^{n+1} = (d_\tau xx) + \Delta t^{n+1/2}\, u^{xz^{n+1/2}}[(d_\tau xz)^{n+1} + (d_\tau xz)^n] + \Delta d_\tau xx$$

<div align="right">A10</div>

and,

$$(d_\tau zz)^{n+1} = (d_\tau zz) + \Delta t^{n+1/2}\, u^{xz^{n+1/2}}[(d_\tau xz)^{n+1} + (d_\tau xz)^n] + \Delta d_\tau zz$$

where,

$$\Delta d_\tau xx = 2\Delta t^{n+1/2}\, g^{n+1/2}\, (d_d xx)^{n+1/2}$$

$$\Delta d_\tau xz = 2\Delta t^{n+1/2}\, g^{n+1/2}\, (d_d xz)^{n+1/2}$$

$$\Delta d_\tau zz = 2\Delta t^{n+1/2}\, g^{n+1/2}\, (d_d zz)^{n+1/2}$$

For the present analysis only bulk components of the artificial viscosity tensor are used. Therefore, the necessary terms for artificial stress are derived as

$$q_3^{n+1} = \rho_3^{n+1} \sqrt{A_3^{n+1}} \; (\frac{1}{\rho} \frac{\partial \rho}{\partial t}) \; [B_1{}^2 \sqrt{A_3^{n+1}} \; |\frac{1}{\rho} \frac{\partial \rho}{\partial t}| + B_2 c_3^n] \; \text{for} \; \frac{1}{\rho} \frac{\partial \rho}{\partial t} > 0$$

$$q_3^{n+1} = 0 \; \text{for} \; \frac{1}{\rho} \frac{\partial \rho}{\partial t} \leq 0 \qquad \text{A11}$$

Finally, the stress components at time n+1 are computed by

$$(\tau^{xx})^{n+1} = (d_\tau^{xx})^{n+1} - p^{n+1} + q^{n+1}$$

$$(\tau^{zz})^{n+1} = (d_\tau^{zz})^{n+1} - p^{n+1} + q^{n+1} \qquad \text{A12}$$

$$(\tau^{xz})^{n+1} = (d_\tau^{xz})^{n+1}$$

The remaining stress term is solved as

$$(\tau^{yy})^{n+1} = 3p^{n+1} - [(\tau^{xx})^{n+1} + (\tau^{zz})^{n+1}] \qquad \text{A13}$$